

**MAGNETIC AND STRUCTURAL CHARACTERIZATION OF SOLID SOLUTION
 $\text{Ni}_x\text{Zn}_{(1-x)}\text{Fe}_2\text{O}_4$ ($x = 0.5$ AND $x = 1$) SYNTHESIZED BY HIGH ENERGY BALL
MILLING**

by

Ermides Chavez Baldovino

A thesis submitted in partial fulfillment of the requirements for the degree of

MASTER OF SCIENCE
in
PHYSICS

UNIVERSITY OF PUERTO RICO
MAYAGÜEZ CAMPUS
2013

Approved by:

Oswald N C Uwakweh, Ph. D.
President, Graduate Committee

Date

Dorial Castellanos, Ph. D.
Member, Graduate

Date

Henri A. Radovan, Ph. D.
Member, Graduate Committee

Date

Omar Colon, Ph. D.
Representative of Graduate Studies

Date

Dorial Castellanos, Ph. D.
Chairperson of the Department

Date

Copyright © 2013
By
Ermides Chavez Baldovino

Abstract

Mechanochemical reactions of NiO, ZnO, and α -Fe₂O₃ were carried out in a planetary mill to produce Nickel ferrite (NiFe₂O₄) and Nickel-Zinc ferrite (Ni_{0.5}Zn_{0.5}Fe₂O₄) nanocrystallites. All measurements were made at room temperature under identical processing conditions entailing initial addition of 0.6 mL of acetone as surfactant with hardened stainless steel grinding materials. The average crystallite sizes of the particles as determined from X-ray diffraction measurements decreased as a function of milling time, with values between 7.38 and 5.35 nm. Specific Saturation Magnetization determined from Vibrating Sample Magnetometer measurements varied with the milling time and reached a maximum value of 61.94 Am²/Kg (61.94 emu/g). From 1 mT, the coercivity displayed tendency to increase with increasing milling time for the end-member Nickel ferrite phase (NiFe₂O₄) for the three ball to powder ratios (BPR) used. Similar behavior was observed for the $x = 0.50$ composition (Ni_{0.5}Zn_{0.5} Fe₂O₄) ferrite. Room temperature Mössbauer spectra of all samples exhibited non-magnetic peaks, which evolved from the sextets associated with the precursor hematite phase, and ultimately a total collapse of the sextets due to the relaxation effects linked to the superparamagnetic effect. The rate of the mechanochemical synthesis process depended on the BPR used. The time to achieve NiFe₂O₄ phase was shorter for a BPR of 40:1, when compared to the BPR of 20:01 and 10:01, cases respectively. The superparamagnetic behavior was observed for all ball milled compositions, for crystal sizes less than 7.38 nm.

Resumen

Las reacciones mecanoquímicas de NiO, ZnO, y α -Fe₂O₃ se llevaron a cabo en un molino planetario para producir Níquel ferrita (NiFe₂O₄) y la ferrita de Níquel-Zinc (Ni_{0.5}Zn_{0.5}Fe₂O₄) nanocrystalinas. Todas las mediciones se hicieron a temperatura ambiente bajo condiciones de procesamiento idénticos, que implicaron una adición inicial de 0,6 ml de acetona como agente tensoactivo en conjunto con los materiales de molienda de acero inoxidable. Los tamaños medios de las partículas, tal como se determinaron a partir de mediciones de difracción de rayos X, disminuyeron como función del tiempo de molienda, con valores entre 7,38 y 5,35 nm. Magnetización de saturación específica determinada a partir de mediciones de magnetometría de muestra vibrante variaron con el tiempo de molienda y alcanzaron un valor máximo de 61,94 Am²/Kg (61,94 emu/ g). A partir de 1 mT, la coercitividad muestra tendencia de aumentar con el incremento del tiempo de molienda para la fase de la ferrita de Níquel o miembro final (NiFe₂O₄) para las tres razones de bolas a polvo (BPR) utilizados. Un comportamiento similar se observó para la composición $x = 0,50$ de la ferrita de Níquel-Zinc (Ni_{0.5}Zn_{0.5} Fe₂O₄). Los espectros de Mössbauer a temperatura ambiente de todas las muestras, mostraron picos no magnéticos, que evolucionaron a partir de los sextetos asociados a la fase del precursor (hematita), y en última instancia un colapso total de los sextetos, debido a los efectos de relajación, relacionados con el efecto superparamagnético. El tiempo de obtención de la síntesis mecanoquímica dependió de la BPR utilizado. El tiempo para alcanzar la fase NiFe₂O₄ fue más corto para un BPR de 40:1, en comparación con BPR de 20:01 y 10:01, respectivamente. El tiempo para lograr el comportamiento superparamagnético mostró una dependencia de la BPR utilizado, a mayor BPR menor es el tiempo para alcanzar la fase. Se observó el comportamiento superparamagnético para todas las composiciones de bolas de molidas, para los tamaños de partícula menores a 7.38 nm.

Dedictory

To my parents, Cilia Esther Baldovino Hernandez and Ermides Chavez Barba, two precious loved ones and most wonderful beings placed by God in my life, whom have taught me with love, commitment and dedication that I can achieve my biggest dreams. With all my heart, I dedicate them this triumph

Acknowledgments

I would like to acknowledge Almighty God, my partner and friend at all times, and in every situation and circumstance.

My parents, Cilia Esther Baldovino Hernandez y Ermides Chavez Barba be the foundation for the construction of this work and major projects that await me.

I acknowledge The University of Puerto Rico at Mayaguez for giving me the opportunity to perform this research.

I also would like to acknowledge Dr. Oswald N. C Uwakweh for their assistance in conducting this research.

In addition, I would like to acknowledge The NANOMaterials Processing Laboratory for allowing the use of some equipment during the execution of this research.

Further, I would like to acknowledge Mr. Boris Renteria for his assistance in the realization of the VSM measurements.

I acknowledge Ms. Angela Ferra Elias and Ms. Amanda Blagg, for their logistical support in the realization of this Thesis. Same goes Ms. Neshma Lopez for her assistance with the syntheses processing carried out at different times.

Finally, I extend my acknowledgements to all the people whose support and collaboration made possible the realization of this work, as I say my sincere thanks to them.

Contents

Abstract.....	iii
Resumen	iv
Dedicatory.....	v
Acknowledgments.....	vi
1. Introduction	1
2. THEORETICAL BACKGROUND	4
2.1. Basic concepts.....	4
2.1.1. Magnetization.....	4
2.1.2. Magnetic susceptibility and permeability.....	4
2.1.3. Single-Domain Particles	9
2.1.4. Coercivity of Fine Particles.....	10
2.1.5. Superparamagnetism.....	11
2.1.6. Hysteresis Loops.....	12
2.1.7. Hysteresis Loops- Superparamagnetism.....	14
2.3.2. Structure of Ferrites.....	16
3. EXPERIMENTAL PROCEDURES.....	19
3.1. Sample Synthesis	19
3.2. High Energy Ball Milling Process	20
3.3. Characterization Techniques	22
3.3.1. Powder X-Ray Diffraction (PXRD).....	22
3.3.2. Vibrating Sample Magnetometer (VSM).....	25
3.3.3. Mössbauer Spectroscopy (MS)	26
3.3.3.1. Basic Principles of Mössbauer Spectroscopy	29
3.3.3.2. Mössbauer parameters.....	29
4. $\text{Ni}_x\text{Zn}_{(1-x)}\text{Fe}_2\text{O}_4$ x = 1 with BPR = 10:1	35
4.1 Results and Discussion	35
4.1.1 X-ray diffraction for BPR = 10:1.....	35

4.1.2	Measurements of magnetization for BPR = 10:1	40
4.1.3	Measurements of Mössbauer for BPR = 10:1	43
4.2.	Conclusions	46
5.	$\text{Ni}_x\text{Zn}_{(1-x)}\text{Fe}_2\text{O}_4$ $x = 1$ with BPR = 20:1	47
5.1	X-Ray Diffraction for BPR = 20:1	47
5.2	Measurements of Magnetization for BPR = 20:1.....	52
5.3	Measurements of Mössbauer for BPR = 20:1	55
6.2	$\text{Ni}_x\text{Zn}_{(1-x)}\text{Fe}_2\text{O}_4$ $x = 1$ (NiFe_2O_4) with BPR = 40:1.....	58
6.2.2.	X-ray diffraction for BPR = 40:1.....	58
6.2.2.	Measurements of Magnetization for BPR = 40:1.....	62
6.2.2.	Measurements of Mossbauer for BPR = 40:1	66
7.	$\text{Ni}_x\text{Zn}_{(1-x)}\text{Fe}_2\text{O}_4$ $x = 0.5$ with BPR = 10:1	68
7.1	X-ray diffraction for BPR = 10:1	68
7.2	Measurements of Magnetization for BPR = 10:1.....	73
7.3	Measurements of Mossbauer for BPR = 10:1	77
8	$\text{Ni}_x\text{Zn}_{(1-x)}\text{Fe}_2\text{O}_4$ $x = 0.5$ with BPR = 20:1	81
8.1	X-ray diffraction for BPR = 20:1	81
8.2	Measurements of Magnetization for BPR = 20:1.....	87
8.3	Measurements of Mossbauer for BPR = 20:1	90
9	$\text{Ni}_x\text{Zn}_{(1-x)}\text{Fe}_2\text{O}_4$ $x = 0.5$ with BPR = 40:1	96
9.1	X-ray diffraction for BPR = 40:1	96
9.2	Magnetization measurement for BPR = 40:1.....	102
9.3	Measurements of Mössbauer for BPR 40:1	106
10.	Conclusions	108

LIST OF FIGURES

Figure 2.1. The inverse susceptibility ($1/\chi$) varies with Temperature (T) for (a) Diamagnetic, (b) Paramagnetic, (c) Ferromagnetic, (d) Antiferromagnetic, (e) Ferrimagnetic. T_N , and T_C are Néel temperature and Curie temperature respectively and θ_p is called paramagnetic Curie point.	9
Figure 2.2. Typical hysteresis loop of a ferromagnetic material.....	13
Figure 2.3. Crystal structure of a cubic ferrite	18
Figure 3.1 a) Motion of planetary ball mill, b) Schematic diagram of motion of grinding balls.....	20
Figure 3.2 Schematic diagram of Bragg reflection from a set of crystal planes.	23
Figure 3.3. Schematic representation a vibrating sample magnetometer (VSM)	26
Figure 4.8. Mössbauer spectra of NiFe_2O_4 for BPR 20:1	57
Figure 6.1. X-ray diffraction spectra of the formation of NiFe_2O_4 during mechanochemical synthesis for BPR = 40:1.....	58
Figure 6.2. Evolution of particle size and Strain of formed NiFe_2O_4 (BPR = 40:1) as a function of ball milling time.	61
Figure 6.3 VSM measurements showing evolution of magnetic properties of reacting mixtures for BPR = 40:1 as a function of milling time.	63
Figure 6.4 Evolution of coercivity and saturation magnetization as a function of ball milling of NiFe_2O_4 for BPR 40:1	64
Figure 6.5 Mössbauer spectra of NiFe_2O_4 for BPR 40:1	66
Figure 6.6. XRD spectra and $\text{Ni}_{0.5}\text{Zn}_{0.5}\text{Fe}_2\text{O}_4$ for BPR = 10:1	69
Figure 6.7. Evolution of particle size and strain of formed $\text{Ni}_{0.5}\text{Zn}_{0.5}\text{Fe}_2\text{O}_4$ (BPR = 10:1) as a function of ball milling time.	71
Figure 6.8. VSM measurements corresponding of $\text{Ni}_{0.5}\text{Zn}_{0.5}\text{Fe}_2\text{O}_4$ for BPR = 10:1	73
Figure 6.9. Evolution of coercivity and saturation magnetization as a function of ball milling of $\text{Ni}_{0.5}\text{Zn}_{0.5}\text{Fe}_2\text{O}_4$ for BPR 10:1.	76
Figures 6.10. Mössbauer spectra of $\text{Ni}_{0.5}\text{Zn}_{0.5}\text{Fe}_2\text{O}_4$ for BPR = 10:1	80
Figure 6.11. XRD spectra and $\text{Ni}_{0.5}\text{Zn}_{0.5}\text{Fe}_2\text{O}_4$ for BPR = 20:1	81

Figure 6.12. Particle size reduction $\text{Ni}_{0.5}\text{Zn}_{0.5}\text{Fe}_2\text{O}_4$ for BPR = 20: 1 as a function of time ball milling	83
Figure 6.13. VSM measurements corresponding of $\text{Ni}_{0.5}\text{Zn}_{0.5}\text{Fe}_2\text{O}_4$ for BPR 40:1	87
Figure 6.14. Evolution of coercivity and saturation magnetization as a function of ball milling of $\text{Ni}_{0.5}\text{Zn}_{0.5}\text{Fe}_2\text{O}_4$ for BPR 20:1	90
Figure 9.1. XRD spectra and $\text{Ni}_{0.5}\text{Zn}_{0.5}\text{Fe}_2\text{O}_4$ for BPR = 40:1	97
Figure 9.2. Average particle size reduction of $\text{Ni}_{0.5}\text{Zn}_{0.5}\text{Fe}_2\text{O}_4$ for BPR 40:1 as a function of milling time	101
Figure 9.3. Vibrating sample magnetometer (VSM) corresponding to the different ball milled of $\text{Ni}_{0.5}\text{Zn}_{0.5}\text{Fe}_2\text{O}_4$ for BPR 40:1 as a function of time.	102
Figure 9.4. Evolution of coercivity and saturation magnetization as a function of ball milling of $\text{Ni}_{0.5}\text{Zn}_{0.5}\text{Fe}_2\text{O}_4$ for BPR 40:1	105
Figures 9.5. Mössbauer spectra of $\text{Ni}_{0.5}\text{Zn}_{0.5}\text{Fe}_2\text{O}_4$ for BPR = 40:1	107

1. Introduction

Spinel ferrites have the general molecular formula $(A^{2+})[B_2^{3+}]O_4^{2-}$ where A^{2+} and B^{3+} are the divalent and trivalent cations occupying tetrahedral (A) and octahedral (B) interstitial positions of the fcc lattice formed by O^{2-} ions. The magnetic properties of these oxides depend on the type of cations and their distribution among these two interstitial positions. The cation distribution and the resulting magnetic properties are found to be different and quite interesting in some nanocrystalline spinel ferrites when compared to those of their bulk counterparts [1-6]. The striking example is $ZnFe_2O_4$, which, in the bulk form, is a normal spinel with the Zn^{2+} ions at the A sites, while the Fe^{3+} ions are at the B sites, and exhibits antiferromagnetic ordering below 10 K. But nanocrystalline $ZnFe_2O_4$ with a grain size of about 5–20 nm is reported to be magnetically ordered with a large magnetic moment even at high temperatures [6]. The observed high temperature magnetic ordering is attributed to the change in the cation distribution from the normal to the mixed spinel type where Fe^{3+} and Zn^{2+} ions occupy both the sites. On the other hand, $NiFe_2O_4$ is a well-known inverse spinel with Ni^{2+} ions on B sites and Fe^{3+} ions distributed equally among A and B sites. Their use and interest date back to more than four decades when their magnetic properties were studied and reported by Néel [7-9] who suggested that small antiferromagnetic particles can exhibit superparamagnetism and weak ferromagnetism due to uncompensated spins in the two sublattices. They are special magnetic materials whose importance is manifested on their use in a host of scientific and technological applications such as in magnetic and switching devices to mention but a few [10]. Their performances in applications can be tied to their stoichiometric compositions with respect to cationic distribution,

microstructures, and consequently to their syntheses methods, including attendant processing techniques employed in product realization [11, 12]. Apart from their bulk properties interests, they are commanding or attracting keen interests based on the fact that they exhibit unusual properties in their nanoscale forms.

The synthesis of nanocrystalline spinel $\text{Ni}_{0.5}\text{Zn}_{0.5}\text{Fe}_2\text{O}_4$ (Ni-Zn) and NiFe_2O_4 (Ni-Fe) ferrites have been investigated intensively in recent years due to their potential applications in non-resonant devices, radio frequency circuits, high-quality filters, rod antennas, transformer cores, read/write heads for high-speed digital tapes and operating devices [13-16]. Magnetic properties of Ni-Zn and Ni-Fe ferrites rely heavily on the chemical composition and are also sensitive to their microstructure [17]. The general formula of these materials is: $(\text{Zn}_x\text{Fe}_{1-x})_{\text{tetra}}[\text{Ni}_{1-x}\text{Fe}_{1+x}]_{\text{octa}}\text{O}_4$. Ni-Zn and Ni-Fe ferrites are of particular interest because the magnetic properties of the nanoparticles differ markedly from those of their bulk counterpart. It is of further interest to replace a non-magnetic Zn^{2+} ion by a magnetic Ni^{2+} in Zn-ferrite to understand the difference in the properties of the system of ferrites in the limit of nano-regime. The properties of these ferrites are highly sensitive to the cation distribution which in turn depends on the method of preparation and sintering conditions. Spinel-type ferrites can be prepared by a variety of methods [18-23].

Mechanochemical processes by HEBM entail chemical transformations that occur in finite region of the induced particles in the range of 10^{-5} to 10^{-6} m [24]. The changes associated with or induced by ball milling include the alteration or generation of specific surface areas of the solid precursor particles by dynamic deformation, fracturing, etc. All of these occur together with rapid solid particle reduction, while intimate mixings are enhanced with the use of surfactants such alcohol, acetone, etc. [26-27]. The high-energy milling as a solid-state method for synthesis

of nanodimensional materials has the advantage that it can be easily operated and produce large amounts of nanostructured powders in a fairly short time. Furthermore, the highly nonequilibrium nature of the milling process allows one to prepare solids with improved and/or novel physical and chemical properties [28].

We use the high energy ball milling process for synthesizing $\text{Ni}_{0.5}\text{Zn}_{0.5}\text{Fe}_2\text{O}_4$ (Ni-Zn) and NiFe_2O_4 (Ni-Fe) samples, and to study the influence of milling time on the structural and magnetic properties of the samples. Furthermore, monitoring the synthesis process for different milling times (intervals of 5 hours), the variation of the ball-to-powder ratio (BPR), and to study the influence these parameter on the magnetization specific saturation, the structural, and magnetic ordering in NiFe_2O_4 and $\text{Ni}_{0.5}\text{Zn}_{0.5}\text{Fe}_2\text{O}_4$ ferrites.

2. THEORETICAL BACKGROUND

2.1. Basic concepts

2.1.1. Magnetization.

Each atomic current is a tiny closed circuit of atomic dimensions, and it may be therefore be appropriately described as a magnetic dipole. In fact, the dipole moment is the quantity of interest here, since the distant magnetic induction field due to a single atom is completely determined by specifying its magnetic dipole moment, \mathbf{m} . Let the magnetic moment of the i th atom be \mathbf{m}_i . We now define a macroscopic vector quantity, the magnetization \mathbf{M} . We sum up vectorially all of the dipole moments in a small volume element Δv , and then divide the result by Δv ; resulting quantity [5],

$$\mathbf{M} = \lim_{\Delta v \rightarrow 0} \frac{1}{\Delta v} \sum_{i=1}^n \Delta \mathbf{m}_i \quad 2.1$$

2.1.2. Magnetic susceptibility and permeability.

Hysteresis. In order to solve problems in magnetic theory, it is essential to have a relationship between \mathbf{B} and \mathbf{H} or, equivalently, a relationship between \mathbf{M} and one of the magnetic field vectors. These relationships depend on the nature of the magnetic material and are usually obtained from experiment. In a large class of materials there exists an approximately linear relationship between \mathbf{M} and \mathbf{H} . If the material is isotropic as well as linear,

$$\mathbf{M} = \chi_v \mathbf{H} \quad 2.2$$

where the dimensionless scalar quantity χ_v is called the magnetic susceptibility. If χ_v is positive, the material is called paramagnetic, and the magnetic induction is strengthened by the presence of the material. If χ_v is negative, the material is diamagnetic, and the magnetic induction is weakened by the presence of the material [5]. Although χ_v is a function of the temperature, and sometimes varies quite drastically with temperature, it is generally safe to say that χ_v for paramagnetic and diamagnetic materials is quite small; i.e.,

$$|\chi_v| \ll 1 \text{ (for paramagnetic, diamagnetic materials).}$$

χ_v also refers to unit volume and is sometimes called the volume susceptibility and given the. Other susceptibilities can be defined, as follows [5, 6]:

$$\chi_m \equiv \chi_v / \rho = \text{mass susceptibility (emu/Oe g), where } \rho \text{ density,}$$

$$\chi_A \equiv \chi_v A = \text{atomic susceptibility (emu/Oe g atom), where } A = \text{atomic weight,}$$

$$\chi_M \equiv \chi_v M = \text{molar susceptibility (emu/Oe mol), where } M = \text{molecular weight}$$

The susceptibility is a parameter in characterization of magnetic properties of material.

The magnitude of the susceptibility and its temperature and the field dependencies provide a measure of magnetic behavior of different types of magnetic materials. Therefore, the magnetic behavior of a material is classified into diamagnetic, paramagnetic, ferromagnetic, antiferromagnetism and ferrimagnetism [7].

Diamagnetism. The electron orbits are randomly oriented, and the orbital dipole moments cancel out. But in the presence of a magnetic field, each atom picks up a little "extra" dipole moment, and these increments are all antiparallel to the field. This is the mechanism responsible for

diamagnetism [8]. If we consider a system consisting of N atoms, each containing i electrons with radii we may write for the susceptibility

$$\chi = \frac{\mathbf{M}}{\mathbf{H}} = -\frac{N\mu_0 e^2}{4m_e} \sum r_i^2 \quad 2.3$$

Where N is the number of atoms per unit volume, μ_0 is the permeability of free space, e is the charge of electron, r is the orbital radius and m_e is the mass of electron [8]

Paramagnetism: Occurs for materials whose atoms or molecules have a magnetic moment. This magnetic moment originates from electrons lying outside closed electron shells. The magnetic moments are completely disordered due to the thermal motion. Applying an external magnetic field, the average angle between the moments and the field direction depends on the ratio of the potential energy of the moments in the field and the thermal energy (analogous to the considerations for dielectrics). Thus, the susceptibility is temperature-dependent, and it is given by Curie's law [9].

$$\chi = \frac{C}{T} \quad 2.4$$

where C is the Curie constant per gram and T is the absolute temperature.

Ferromagnetism: It is a strong magnetic effect present in a small number of crystalline substances. Some examples of ferromagnetic substances are iron, cobalt, nickel, gadolinium, and dysprosium. These substances contain permanent atomic magnetic moments that tend to align

parallel to each other even in a weak external magnetic field. Once the moments are aligned, the substance remains magnetized after the external field is removed. This permanent alignment is due to a strong coupling between neighboring moments, a coupling that can be understood only in quantum mechanical terms. All ferromagnetic materials are made up of microscopic regions called domains, regions within which all magnetic moments are aligned. These domains have volumes of about 10^{-12} to 10^{-8} m^3 and contain 10^{17} to 10^{21} atoms. The boundaries between the various domains having different orientations are called domain walls. [10]

When the temperature of a ferromagnetic substance reaches or exceeds a critical temperature called the Curie temperature, the substance loses its residual magnetization and becomes paramagnetic. Below the Curie temperature, the magnetic moments are aligned and the substance is ferromagnetic. Above the Curie temperature, the thermal agitation is great enough to cause a random orientation of the moments, and the substance becomes paramagnetic and its susceptibility then follows the Curie–Weiss law [7, 10].

$$\chi = \frac{C}{T - \theta} \quad 2.5$$

Where C is the Curie constant per gram, T is the absolute temperature and θ is called Weiss const.

Antiferromagnetic: It is substances have a small positive susceptibility at all temperatures, but their susceptibilities vary in a peculiar way with temperature. As the temperature decreases, χ increases but goes through a maximum at a critical temperature called the Néel temperature T_N . The substance is paramagnetic above T_N and antiferromagnetic below it. T_N often lies far below room temperature, so that it may be necessary to carry susceptibility measurements down to

quite low temperatures to discover if a given substance, paramagnetic at room temperature, is actually antiferromagnetic at some lower temperature. Most, but not all, antiferromagnetics are ionic compounds: oxides, sulfides, chlorides, and the like. A very large number are known, which makes them much more common than ferromagnetics. [6]:

Ferrimagnetic: It is substances exhibit a substantial spontaneous magnetization at room temperature, just like ferromagnetics, and this fact alone makes them industrially important. Like ferromagnetics, they consist of magnetically saturated domains, and they exhibit the phenomena of magnetic saturation and hysteresis. [6].

In fact ferrimagnetic substances are also related to antiferromagnetic, in that the exchange coupling between adjacent magnetic ions leads to antiparallel alignment of the localized moments. The overall magnetization occurs because the magnetization of one sublattice is greater than that of the oppositely oriented sublattice.

The fact that ferrimagnetics are ionic solids means that they are electrically insulating, whereas most ferromagnetics are metals. This results in a wide range of important applications for ferrimagnetics, in situations requiring magnetic insulators.

The magnetic ferrites fall mainly into two groups with different crystal structures: Cubic and Hexagonal [6].

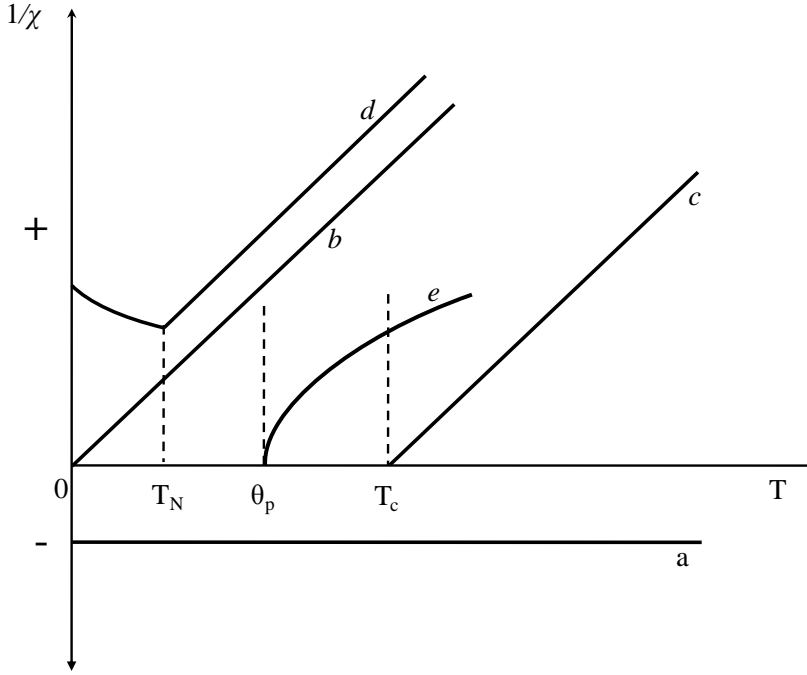


Figure 2.1. The inverse susceptibility ($1/\chi$) varies with Temperature (T) for (a) Diamagnetic, (b) Paramagnetic, (c) Ferromagnetic, (d) Antiferromagnetic, (e) Ferrimagnetic. T_N and T_C are Néel temperature and Curie temperature respectively and θ_p is called paramagnetic Curie point.

2.1.3 Single-Domain Particles

There are good reasons to believe that a sufficiently small magnetic particle will not contain domain walls and so will consist of a single domain. One simple argument is that, if the particle is smaller than the thickness of a domain wall, it cannot consist of two domains separated by a domain wall. Another way to approach the problem is to note that the total magnetostatic energy of a single domain particle of diameter D will vary as the particle volume, which is proportional to D^3 , while the domain wall area and energy will vary as the cross-sectional area of the particle, which is proportional to D^2 . If these are the only energies to consider, there must be a critical diameter D_c below which the single-domain state is favored. The calculation of the critical size for single-domain behavior in specific cases turns out to be tricky and uncertain. The

magnetostatic energy will depend on the saturation magnetization of the material and on the geometry of the particle. The domain wall energy will depend on the values of the anisotropy constant(s) and the exchange stiffness, and perhaps also the magnetostriction and elastic constants, as well as on the geometry. And the exact magnetization configuration in the tiny particle may not be as simple as a pure ferromagnetic state or two purely ferromagnetic regions separated by a domain wall whose structure and energy were calculated for an infinite solid [6].

2.1.4 Coercivity of Fine Particles

The *coercivity*, also called the coercive field or coercive force, of a magnetic material is the intensity of the applied magnetic field required to reduce the magnetization of that material to zero after the magnetization of the sample has been driven to saturation. Thus coercivity measures the resistance of a magnetic material to becoming demagnetized [8].

In magnetic studies on fine particles the single property of most interest is the coercivity, for two reasons: (1) it must be high, at least exceeding a few hundred oersteds, to be of any value for permanent-magnet applications, and (2) it is a quantity which comes quite naturally out of theoretical calculations of the hysteresis loop. The coercivity of fine particles has a striking dependence on their size. As the particle size is reduced, it is typically found that the coercivity increases, goes through a maximum, and then tends toward zero.

Below a critical diameter D_s the particles become single domains, and in this size range the coercivity reaches a maximum. (The quantity D_s is the critical diameter). Particles of size D_s and smaller change their magnetization by spin rotation, but more than one mechanism of rotation

can be involved. As the particle size decreases below D_s the coercivity decreases, because of thermal effects, according to:

$$H_{ci} = g - \frac{h}{D^{3/2}} \quad 2.6$$

This equation is derived from the behavior of nanoparticles. Where g and h are constants and D is the particle size.

Below a critical diameter D_p the coercivity is zero, again because of thermal effects, which are now strong enough to spontaneously demagnetize a previously saturated assembly of particles.

Such particles are called *superparamagnetic* [6].

2.1.5 Superparamagnetism

Consider an assembly of uniaxial, single-domain particles, each with an anisotropy energy density $E = K \sin^2(\theta)$, where K is the anisotropy constant and θ the angle between M_s and the easy axis. If the volume of each particle is V , then the energy barrier ΔE that must be overcome before a particle can reverse its magnetization is KV . Now in any material, fluctuations of thermal energy are continually occurring on a microscopic scale. In 1949 Néel pointed out that if single-domain particles became small enough, KV would become so small that energy fluctuations could overcome the anisotropy forces and spontaneously reverse the magnetization of a particle from one easy direction to the other, even in the absence of an applied field. Each particle has a magnetic moment $\mu = M_s V$ and, if a field is applied, the field will tend to align the moments of the particles, whereas thermal energy will tend to disalign them. This is just like the behavior of a normal paramagnetic, with one notable exception. The magnetic moment per atom or ion in a normal paramagnetic is only a few Bohr magnetons. But a spherical particle of iron 50 Å in

diameter contains 5560 atoms and has the relatively enormous moment of $(5560)(2.2) = 12,000 \mu_B$. As a result, Bean coined the very apt term *superparamagnetism* to describe the magnetic behavior of such particles [6].

2.1.6 Hysteresis Loops

Both ferro- and ferrimagnetic materials differ widely in the ease with which they can be magnetized. If a small applied field suffices to produce saturation, the material is said to be magnetically soft. Saturation of some other material, which will in general have a different value of saturation magnetization (M_s), may require very large fields. Such a material is magnetically hard [6].

First, let us consider an unmagnetized sample of ferromagnetic material. If the magnetic intensity, initially zero, is increased monotonically, then the **B-H** relationship will trace out a curve something like that shown in Figure 2.2. This is called the *magnetization curve* of the material. It is evident that μ 's taken from the magnetization curve, using the expression $\mu = \mathbf{B}/\mathbf{H}$, are always of the same sign. (positive), but they show a rather large spectrum of values. The maximum permeability occurs at the “knee” of the curve; in some materials this maximum permeability is as large as $10^5 \mu_0$; in others it is much lower. The reason for the knee in the curve is that the magnetization **M** reaches a maximum value in the material, and

$$\mathbf{B} = \mu_0 (\mathbf{H} + \mathbf{M}) \quad 2.7$$

continues to increase at large **H** only because of the $\mu_0 \mathbf{H}$ term [1]. The maximum value of **M** is called the saturation magnetization. Next consider a ferromagnetic specimen magnetized by the above procedure. If the magnetic intensity **H** is decreased, the **B-H** relationship does not follow back down the curve of Figure 2, but instead moves along the new curve of Figure 2.2 to point r.

The magnetization, once established, does not disappear with the removal of \mathbf{H} ; in fact, it takes a reversed magnetic intensity to reduce the magnetization to zero. If \mathbf{H} continues to build up in the reversed direction, then \mathbf{M} (and hence \mathbf{B}) will establish itself in the reversed direction, and Figure 2.2 begins to show a certain symmetry. Finally, when \mathbf{H} once again increases, the operating point follows the lower curve of Figure 2. Thus the \mathbf{B} - \mathbf{H} curve for increasing \mathbf{H} is entirely different from that for decreasing \mathbf{H} . This phenomenon is called hysteresis, from the Greek word meaning "to lag"; the magnetization literally lags the exciting field [5].

The curve of Figure 2.2 is called the hysteresis loop of the material. The value of \mathbf{B} at point r is known as the retentivity or *remanence*; the magnitude of \mathbf{H} at point c is called the coercive force or *coercivity* of the material. From Figure 2.2 it is evident that the value of μ , defined by Eq. (6), is negative in the second and fourth quadrants of the diagram. The shape of the hysteresis loop depends not only upon the nature of the ferromagnetic material but also on the maximum value of \mathbf{H} to which the material is subjected. However, once \mathbf{H}_{\max} is sufficient to produce saturation in the material, the hysteresis loop does not change shape with increasing \mathbf{H}_{\max} . [5]

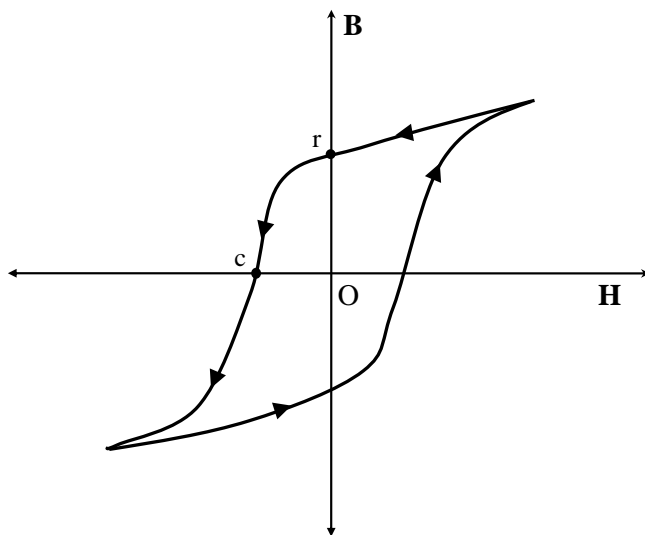


Figure 2.2. Typical hysteresis loop of a ferromagnetic material

2.1.7 Hysteresis Loops- Superparamagnetism

If the anisotropy is zero, then the magnetic moment of each particle can point in any direction, and the classical theory of paramagnetism reproduces the behavior of the particles well. The magnetization is described by the Langevin function:

$$M = Nm \left[\coth \left(\frac{mH}{k_B T} \right) - \frac{k_B T}{mH} \right] = NmL(\alpha) \quad 2.8$$

where $\alpha = mH/k_B T$, and $L(\alpha) = \coth(\alpha) - 1/\alpha$ is the Langevin function.

In the superparamagnetic case, however, because the magnetic moment per particle, m , is large, α is correspondingly large, and so the full magnetization curve, up to saturation, can be observed easily even at moderate fields. (Remember that, for ordinary paramagnetic materials, very high fields and low temperatures were required to study the whole magnetization curve.)

If the anisotropy of each particle is finite, and the particles are aligned with their easy axes parallel to each other and the field, then the moment directions are quantized, with two allowed orientations. In this case the magnetization is described by the special case of the Brillouin function with $J = 1/2$, i.e.

$$M = Nm \tanh(\alpha) \quad 2.9$$

Again, the entire magnetization curve can be obtained even at moderate fields. In the general case, the particles are not perfectly aligned, and neither of these ideal equations exactly describes the observed magnetization curve. Also, in most samples the particles are not all the same size and the moment per particle is not constant, giving further deviation from ideality. In all cases,

however, there is no hysteresis (that is, the coercivity and the remanent magnetization are both zero), and so superparamagnetic materials are not suitable for recording media. Superparamagnetism can be destroyed by reducing the temperature, increasing the particle size, or increasing the anisotropy, such that $KV > k_B T$.

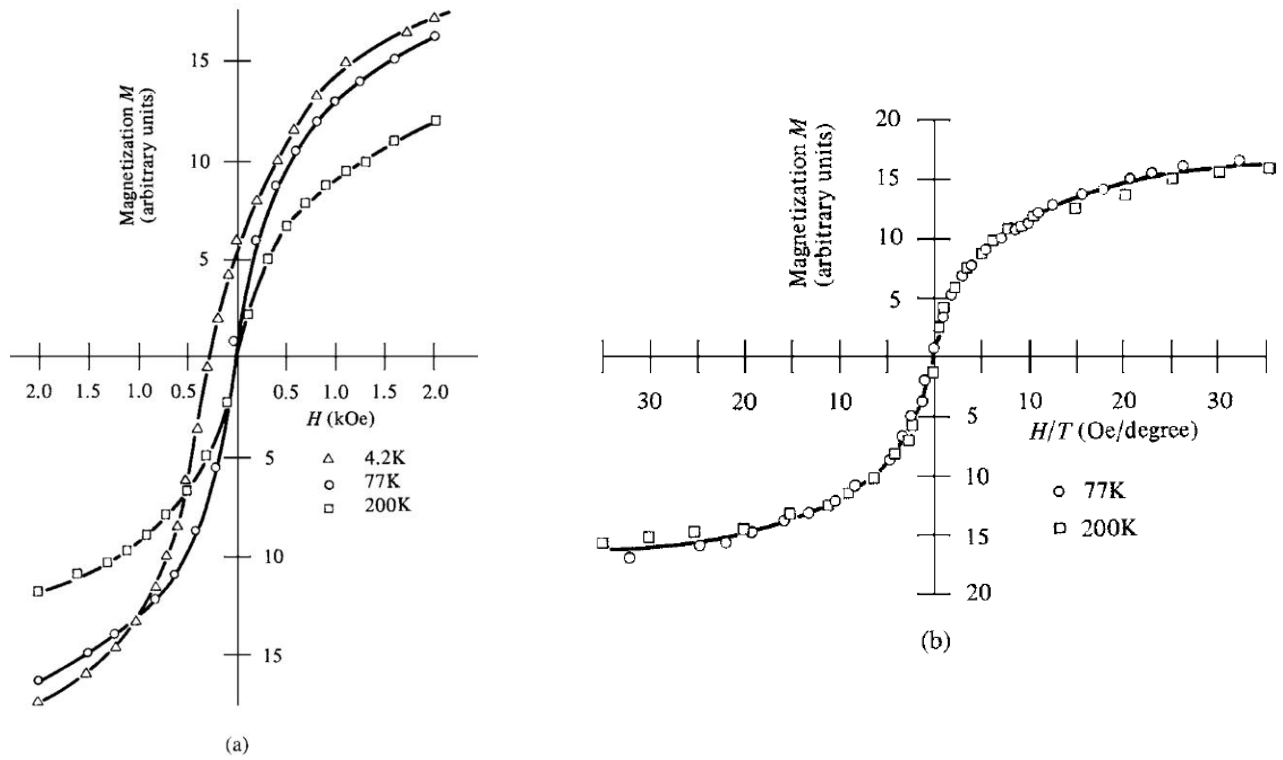


Figure 2.3 Magnetization curves of iron particles 44 Å in diameter. a) M vs H b) M vs H/T .

Figure 2.3, shows the magnetization curves of 44 Å diameter iron particles from one of the earliest studies of superparamagnetism [8]. At 200 K and 77 K the particles show typical superparamagnetic behavior, with no hysteresis. Note also that the induced magnetization is higher at 77 K than at 200 K for the same applied field, as we would expect from the Langevin theory. At 4.2 K, however, the particles do not have enough thermal energy to overcome their energy gain from orienting along the applied field direction, and so hysteresis is observed (only half of the hysteresis loop is shown in the figure) [8].

2.3.2 Structure of Ferrites

The magnetic ferrites fall mainly into two groups with different crystal structures:

Cubic: These have the general formula MFe_2O_3 , where M is a divalent metal ion, like Mn, Ni, Fe, Co, or Mg. Cobalt ferrite CoFe_2O_4 is magnetically hard, but all the other cubic ferrites are magnetically soft. As magnetic materials, these ferrites are both old and new, inasmuch as magnetite Fe_3O_4 ($=\text{FeO} \cdot \text{Fe}_2\text{O}_3$), which might be called iron ferrite, is the oldest magnetic material known to man, the “lodestone” of the ancients.

Hexagonal: The most important in this group are barium and strontium ferrites, $\text{BaO} \cdot 6 \text{Fe}_2\text{O}_3$ and $\text{SrO} \cdot 6 \text{Fe}_2\text{O}_3$, which are magnetically hard [6].

Spinel ferrites such as Fe_3O_4 have a complex cubic unit cell, subunits of which are shown in Figure 3. Oxygen atoms occupy four of the vertices of each of the eight small cubes which make up the unit cell. There are two distinct types of sites which the transition metal ions can occupy, tetrahedral (A) sites and octahedral (B) sites. Of the 64 possible tetrahedral sites in the spinel unit cell, only eight are occupied. Of the 32 possible octahedral sites, only 16 are occupied. Therefore, in each formula unit, Fe_3O_4 , one A site and two B sites are occupied. The A-occupied

sub-cells are tetrahedrally arranged within the unit cell and the B-occupied cells are arranged in a complementary tetrahedron (Figure 2.3).

Not all of the available sites are actually occupied by metal ions. Only one-eighth of the A sites and one-half of the B sites are occupied. In the mineral spinel, the Mg^{2+} ions are in A sites and the Al^{3+} ions are in B sites. Some ferrites MFe_2O_3 have exactly this structure, with M^{2+} in A sites and Fe^{3+} in B sites. This is called *the normal spinel structure*. Both zinc and cadmium ferrite have this structure and they are both nonmagnetic, i.e., paramagnetic. Many other ferrites, however, have *the inverse spinel structure*, in which the divalent ions are on B sites, and the trivalent ions are equally divided between A and B sites. The divalent and trivalent ions normally occupy the B sites in a random fashion, i.e., they are disordered. Iron, cobalt, and nickel ferrites have the *inverse structure*, and they are all ferrimagnetic.

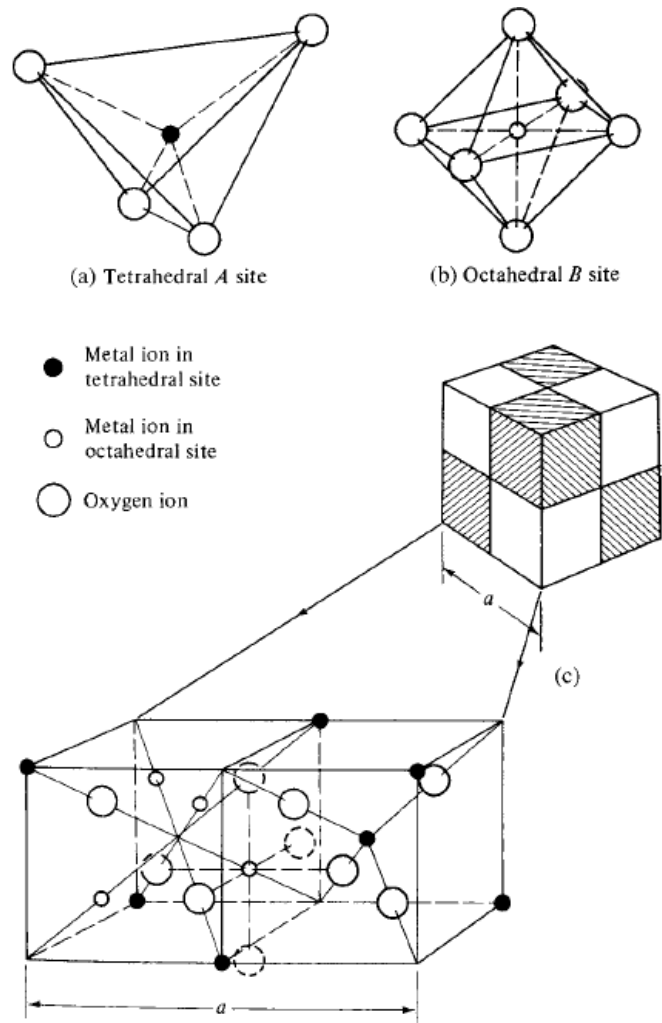
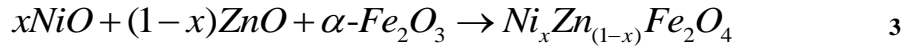


Figure 2.4. Crystal structure of a cubic ferrite

3. EXPERIMENTAL PROCEDURES

3.1. Sample Synthesis

In this work were synthesized samples of $Ni_xZn_{(1-x)}Fe_2O_4$ ($x = 0.5$ and $x = 1$), by ball milling method of high energy. The solid precursors used for this study were Alfar Aesar supplied NiO (99.9 %, metal basis), ZnO (99.9 %, metal basis) and $\alpha-Fe_2O_3$ (99 + %, metal basis), weighed out in stoichiometric amounts to yield the single phase $Ni_xZn_{(1-x)}Fe_2O_4$ via the reaction scheme:



The three powder materials were loaded in vials of Tungsten Carbide (WC) for Pulverisette-4 mills with 10 mm diameter tempered steel balls totalling 17 and 0.6 ml of acetone to the initial materials mixture was used. The setting was 1400 rpm for the main disc, with a R-ratio – 3.0. The milling times were 5, 10, 15, 20, 25, 30 and 35 hours in Pulverisette-4 millings intermittently stopped to retrieve powder samples for analysis. Also, was varied the ball to powder ratios (BPR) with 10:1, 20:1 and 40:1 respectively.

3.2. High Energy Ball Milling Process

Two different terms are commonly used in the literature to denote the processing of powder particles in high-energy ball mills. Mechanical Alloying (MA) describes the process when mixtures of powders (of different metals or alloys/compounds) are milled together. Material transfer is involved in this process to obtain a homogeneous alloy. On the other hand, milling of uniform (often stoichiometric) composition powders, such as pure metals, intermetallics, or prealloyed powders, where material transfer is not required for homogenization, has been termed Mechanical Milling (MM). The destruction of long-range order in intermetallics to produce either a disordered intermetallic or an amorphous phase has been referred to as Mechanical Disordering (MD). [11]

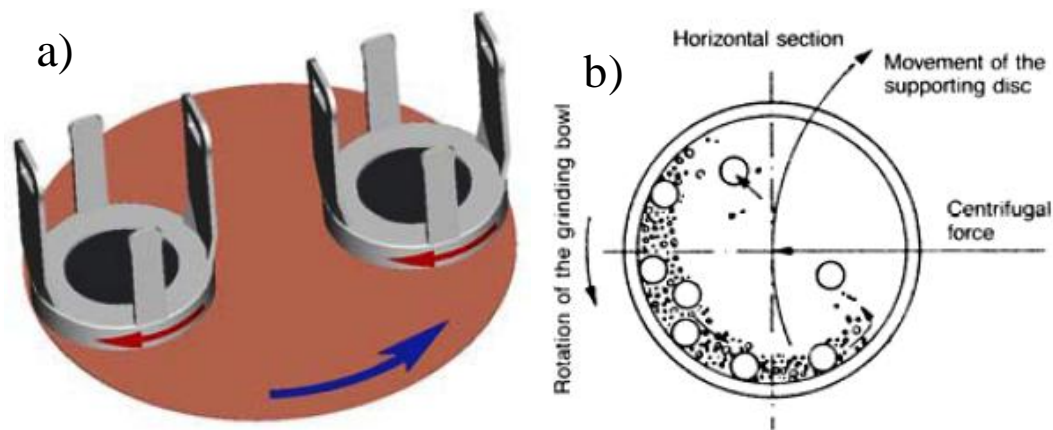


Figure 3.1 a) Motion of planetary ball mill, b) Schematic diagram of motion of grinding balls

Another popular mill for conducting MA experiments is the planetary ball mill (referred to as Pulverisette) in which a few hundred grams of the powder can be milled at a time. The planetary ball mill owes its name to the planet-like movement of its vials. These are arranged on a rotating support disk and a special drive mechanism causes them to rotate around their own axes. The

centrifugal force produced by the vials rotating around their own axes and that produced by the rotating support disk both act on the vial contents, consisting of material to be ground and the grinding balls. Since the vials and the supporting disk rotate in opposite directions, the centrifugal forces alternately act in like and opposite directions. This causes the grinding balls to run down the inside wall of the vial - the friction effect, followed by the material being ground and grinding balls lifting off and traveling freely through the inner chamber of the vial and colliding against the opposing inside wall - the impact effect (Fig. 3.1). Even though the disk and the vial rotation speeds could not be independently controlled in the earlier versions, it is possible to do so in the modern versions. Grinding vials and balls are available in eight different materials - agate, silicon nitride, sintered corundum, zirconia, chrome steel, Cr-Ni steel, tungsten carbide, and plastic polyamide. [4, 5, 11]

3.3. Characterization Techniques

The techniques used for the characterization of the samples in this thesis were:

- Powder X-ray Diffraction (PXRD)
- Vibrating Sample Magnetometry (VSM)
- Mössbauer Spectroscopy (MS)

3.3.1. Powder X-Ray Diffraction (PXRD)

Crystalline solids consist of regular arrays of atoms, ions or molecules with interatomic spacings of the order of 100 pm. For diffraction to take place, the wavelength of the incident light has to be of the same order of magnitude as the spacings of the grating. Because of the periodic nature of the internal structure, it is possible for crystals to act as a three-dimensional diffraction grating to light of a suitable wavelength. This discovery was immediately noted by W.H. and W.L. Bragg (father and son), and they started experiments on using X-ray crystal diffraction as a means of structure determination. In 1913 they first determined the crystal structure of NaCl, and they went on to determine many structures including those of KCl, ZnS, CaF₂, CaCO₃, and diamond. W.L. (Lawrence) Bragg noted that X-ray diffraction behaves like ‘reflection’ from the planes of atoms within the crystal and that only at specific orientations of the crystal with respect to the source and detector are X-rays ‘reflected’ from the planes. It is not like the reflection of light from a mirror, as this requires that the angle of incidence equals the angle of reflection, and this is possible for all angles. With X-ray diffraction, the reflection only occurs when the conditions for constructive interference are fulfilled [11].

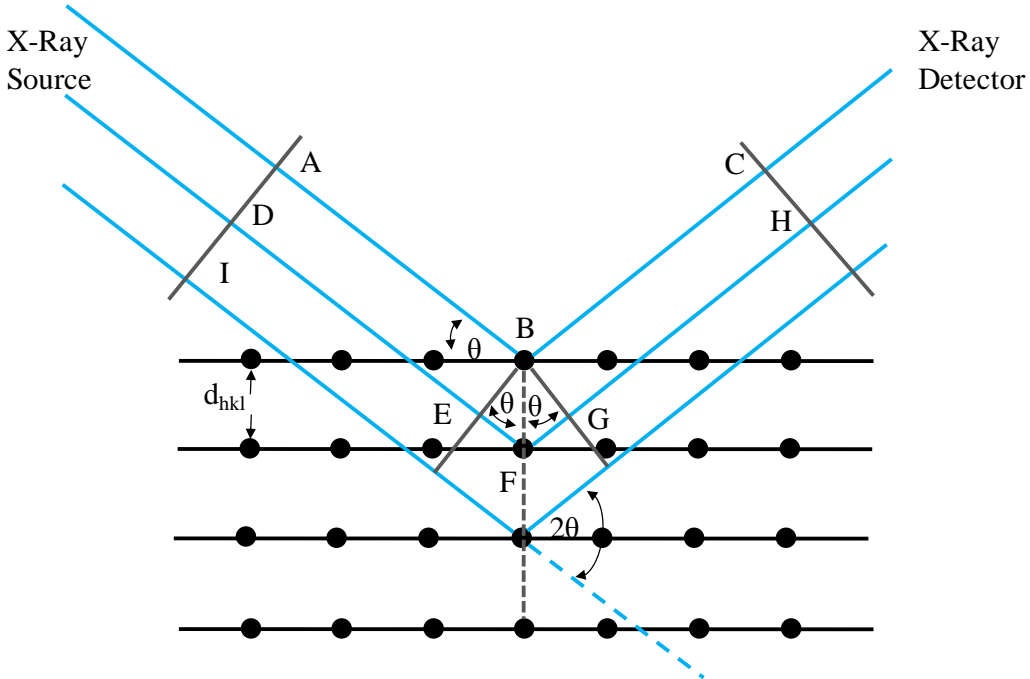


Figure 3.2 Schematic diagram of Bragg reflection from a set of crystal planes.

Figure (3.2) illustrates the Bragg condition for the reflection of X-rays by a crystal. The array of black points in the diagram represents a section through a crystal and the lines joining the dots mark a set of parallel planes with Miller indices hkl and interplanar spacing d_{hkl} . A parallel beam of monochromatic X-rays ADI is incident to the planes at an angle θ_{hkl} . The ray A is scattered by the atom at B and the ray D is scattered by the atom at F . For the reflected beams to emerge as a single beam of reasonable intensity, they must reinforce, or arrive in phase with one another. This is known as constructive interference, and for constructive interference to take place, the path lengths of the interfering beams must differ by an integral number of wavelengths. If BE and BG are drawn at right angles to the beam, the difference in path length between the two beams is given by:

$$\text{difference in path length} = EF + FG \quad 3.2$$

but

$$EF = FG = d_{hkl} \sin \theta_{hkl} \quad 3.3$$

so

$$\text{difference in path length} = 2d_{hkl} \sin \theta_{hkl} \quad 3.4$$

This must be equal to an integral number, n , of wavelengths. If the wavelength of the Xrays is λ , then

$$n\lambda = 2d_{hkl} \sin \theta_{hkl} \quad 3.5$$

This is known as the **Bragg equation**, and it relates the spacing between the crystal planes, d_{hkl} , to the particular Bragg angle, θ_{hkl} at which reflections from these planes are observed (mostly the subscript hkl is dropped from the Bragg angle θ without any ambiguity as the angle is unique for each set of planes).

When $n = 1$, the reflections are called first order, and when $n = 2$ the reflections are second order and so on. However, the Bragg equation for a second order reflection from a set of planes hkl is

$$2\lambda = 2d_{hkl} \sin \theta \quad 3.6$$

which can be rewritten as

$$\lambda = 2(d_{hkl}/2) \sin \theta \quad 3.7$$

Equation **3.7** represents a first order reflection from a set of planes with interplanar spacing $(d_{hkl}/2)$. The set of planes with interplanar spacing $(d_{hkl}/2)$ has Miller indices $2h \ 2k \ 2l$. Therefore, the second order reflection from hkl is indistinguishable from the first order reflection from $2h \ 2k \ 2l$, and the Bragg equation may be written more simply as

$$\lambda = 2d_{hkl} \sin \theta$$

3.8

3.3.2 Vibrating Sample Magnetometer (VSM)

The vibrating-sample magnetometer (VSM) is based on Faraday's law which states that an *emf* will be generated in a coil when there is a change in magnetic flux linking the coil [2].

$$\varepsilon = - (d\Phi_B/dt) \quad 3.9$$

With $\Phi_B = \int \vec{B} \cdot d\vec{a}$

We may write for a coil with n turns of cross-sectional area a

$$\varepsilon = - na(dB/dt) \quad 3.10$$

If the coil is positioned in a constant magnetic field, one has

$$\mathbf{B} = \mu_0 \mathbf{H} \quad 3.11$$

When we bring a sample having a magnetization M into the coil, we have

$$\mathbf{B} = \mu_0 (\mathbf{H} + \mathbf{M}) \quad 3.12$$

The corresponding magnetic field change is:

$$d\mathbf{B} = \mu_0 d\mathbf{M} \quad 3.13$$

Combining Eqs. (*) and (*)' leads to

$$\varepsilon = - \mu_0 na(d\mathbf{M}/dt) \quad 3.14$$

This means that the oscillating magnetic field of the moving sample induces an alternating *emf* in the detection coils, whose magnitude is proportional to the magnetic moment of the sample.

The (small) alternating emf is amplified, usually with a lock-in amplifier which is sensitive only to signals at the vibration frequency. The lock-in amplifier must be provided with a reference signal at the frequency of vibration, which can come from an optical, magnetic, or capacitive sensor coupled to the driving system [6, 8].

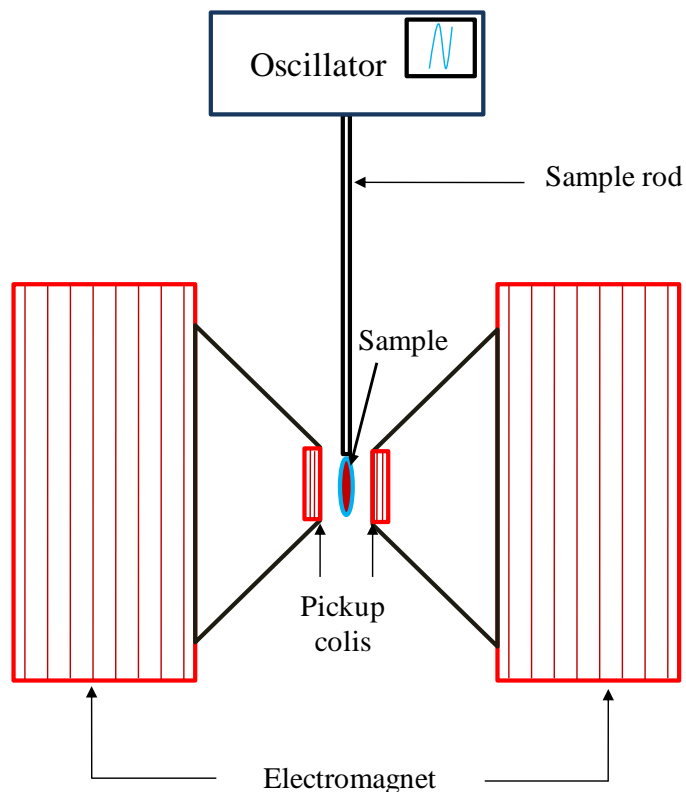


Figure 3.3. Schematic representation a vibrating sample magnetometer (VSM)

3.3.3. Mössbauer Spectroscopy (MS)

Mössbauer spectra are usually recorded in transmission geometry, whereby the sample, representing the absorber, contains the stable Mössbauer isotope, i.e., it is not radioactive. A scheme of a typical spectrometer setup is depicted in Fig. 3(3.4). The radioactive Mössbauer

source is attached to the electro-mechanical velocity transducer, or Mössbauer drive, which is moved in a controlled manner for the modulation of the emitted γ -radiation by the Doppler effect. The Mössbauer drive is powered by the electronic drive control unit according to a reference voltage (VR), provided by the digital function generator. Most Mössbauer spectrometers are operated in constant-acceleration mode, in which the drive velocity is linearly swept up and down, either in a saw-tooth or in a triangular mode. In either case, the source moves periodically back and forth. The emitted γ -photons arriving at the γ -detector are converted into electric pulses which are then amplified, shaped and selected by a chain of electronic components, comprising a preamplifier, a main amplifier and a single-channel analyzer (SCA). The SCA is a pulse discrimination device which can be tuned to the Mössbauer radiation such that pulses of resonance energy are passed on to the multi-channel analyzer (MCA) for acquisition, and pulses from unwanted nonresonant background radiation are rejected. The MCA is the central device of the Mössbauer spectrometer for data acquisition and storage. It essentially consists of an array of digital counters with input logics for discrete electric pulses.

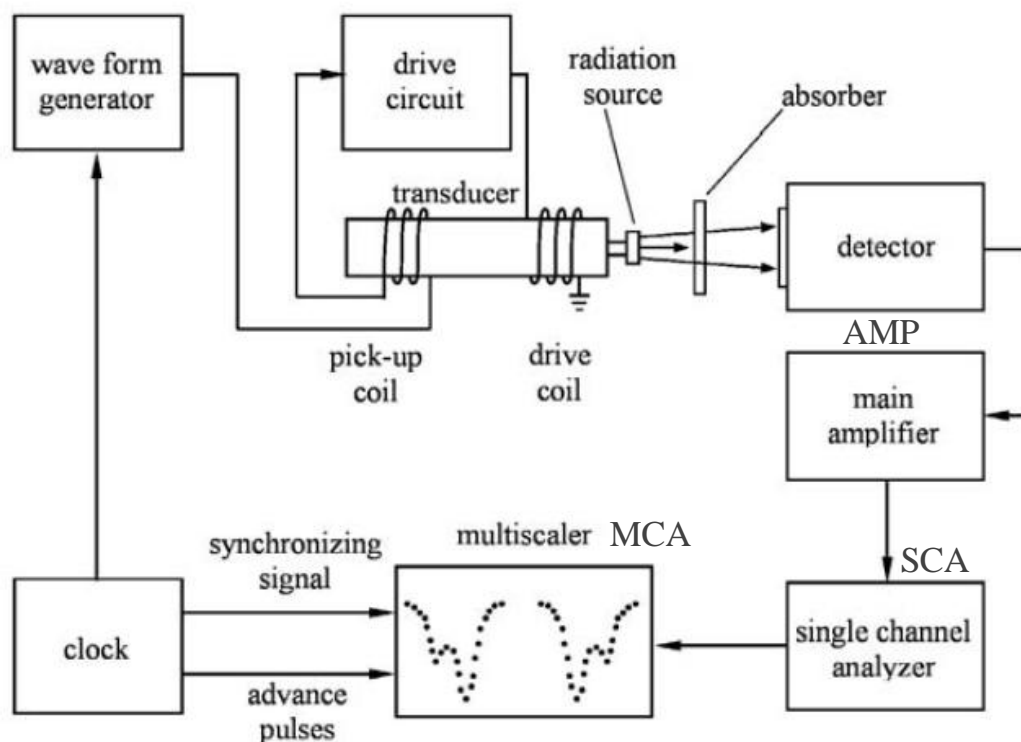


Figure 3.4 1. Schematic representation a Mossbauer spectrometer.

Mössbauer spectroscopy is a valuable analytical tool in a wide range of sciences including geology and mineralogy. It can be used for studying elements that have a Mössbauer-active isotope like iron, tin, gold, etc., just to name a few. It gives information about the oxidation and magnetic state of such elements and about the short-range crystal chemistry of crystalline and amorphous materials containing Mössbauer-active nuclides. As a specific feature of the method, we emphasize that the various Mössbauer-active nuclides that may be present in the same sample can only be studied consecutively because each Mössbauer spectrum is measured with one particular type of radiation source (e.g., ^{57}Co), which can only be used for the measurement of one particular type of Mössbauer-active nuclide (i.e., ^{57}Fe in the given example). Iron is the most abundant in geological (and planetological) environments among the elements that can be studied by Mössbauer spectroscopy. The determination of the valence state and the

characterization of the coordination polyhedra of iron allows geologists and mineralogists to solve current problems of natural inorganic systems. Such systems may be very different in size, from the local crystal chemistry of individual mineral species to the evolution trends of continents.

3.3.3.1. Basic Principles of Mössbauer Spectroscopy

Mössbauer spectroscopy is based on the recoil-free resonance of γ -photons observed with certain atomic nuclei. This method makes it possible to measure nuclear energy levels to an extremely high accuracy (up to 13–15 decimals). Such a precision allows one to measure the slight variation of nuclear energy levels caused by interactions between the electrons and the nucleus. Such interactions reflect changes in the electronic, magnetic, geometric, or defect structure as well as in the lattice vibrations, serving as a basis for a variety of analytical applications.

3.3.3.2. Mössbauer parameters

The main Mössbauer parameters are summarized in Figure 3.4.2. The Mössbauer parameters are presented below in the simplest possible way.

The *isomer shift* δ is a parameter arising from the nuclear energy shift caused by the electric interaction between the nucleus and the (s) electrons that have nonzero density at the site of the nucleus. Thus, the chemical isomer shift is influenced by the oxidation state and by the occupation numbers of electronic orbitals. A simplified formula implying this is as follows:

$$\delta = \Delta E \frac{c}{E_0} = \alpha \Delta |\Psi(0)|^2 \quad 3.15$$

where ΔE is the difference between the median transition energies of the absorber (E_A) and the source (E_S) shown in Fig. 1, which is due to the fact that the Mössbauer nucleus is not naked, but

sitting in the middle of well-determined atomic species both in the source and in the absorber; c/E_0 is the Doppler conversion factor from energy to speed; c is the speed of light in a vacuum; and $\Delta|\Psi(0)|$ is the difference between the electron densities at two identical nuclei, one of which is embedded in the source material, while the other in the absorber material. The factor α comprises several factors including the relative difference between the nuclear radii of the excited state and the ground state for the same nucleus. For small nuclei (e.g., ^{57}Fe and ^{119}Sn), α can be considered as being independent of the electron density, depending exclusively on the kind of the nucleus in question. Since the electron density may change from compound to compound (or, sometimes, from site to site), the chemical isomer shifts of different absorbers will be different even if they are measured with the same source (which is the usual thing to do).

Parameter Formula	⁵⁷ Fe energy level diagram with allowed transition Source (S) Absorber (A)	Schematic representation of absorption vs. relative speed of source and absorber
Chemical isomer shift $\delta_C \propto \Delta E_{IS} = \beta \Delta \Psi(0) ^2$		
Second order Doppler shift $\delta_{SOD} \propto \Delta E_{SOD} = -\frac{\langle u^2 \rangle}{2c^2} E_0$		
Quadrupole splitting $\Delta \propto \Delta E_Q = \frac{1}{2} eQV_{33} \sqrt{1 + \frac{\eta^2}{3}}$		
Magnetic splitting $\Delta_m \propto \Delta E_m = -g_I \mu_N B$		
Peak width $W \geq W_0 \propto 2\Gamma = 2 \frac{\hbar \ln 2}{T_{1/2}}$		

Figure 3.4 2. Representation of the main Mössbauer parameters for the $I = 3/2 \rightarrow 1/2$ transition. $E_0 \approx E_\gamma$ is the median transition energy of the naked nucleus, Γ is the natural line width characteristic of both the emission and absorption profile, and W is the peak width. The δ , Δ , and W values have speed unit (mm/s), while E and Γ have energy unit. [10]

The quadrupole splitting Δ arises from the splitting of the nuclear energy levels caused by the inhomogeneous electric field of valence electrons and ligands. This interaction is determined by the nuclear quadrupole moment (Q) and the components E_{ij} of the electric field gradient (EFG) tensor caused by valence electrons and ligands at the nucleus. If the excited state is characterized by nuclear spin quantum number $I = 3/2$ and the ground state by $I = 1/2$ (which is the case with ⁵⁷Fe and ¹¹⁹Sn), the quadrupole splitting is given by the formula:

$$\Delta = \Delta E_Q \frac{c}{E_0} = \frac{1}{2} e Q V_{33} \sqrt{1 + \frac{\eta^2}{3}} \frac{c}{E_0} \quad 3.16$$

where e is the elementary charge; ΔE_Q is the energy shift shown in Fig. 1; and η is the asymmetry parameter calculated from the second derivatives of the electric potential V

$$\eta = \frac{V_{11} - V_{22}}{V_{33}} \quad 3.17$$

Note that the components of the EFG are obtained from the respective potential derivatives as follows:

$$E_{ij} = -V_{ij} = -\frac{\partial V}{\partial x_i \partial x_j} \quad 3.18$$

and therefore the V_{ij} s are often referred to (incorrectly) as the components of the EFG tensor. The coordinate axes x_1 , x_2 , and x_3 of the cartesian system are labeled in such a way that:

$$|V_{33}| \geq |V_{22}| \geq |V_{11}| \quad 3.19$$

For a point charge ez situated at $r = (x_1, x_2, x_3)$, the V_{ij} components at the nucleus ($r = 0$) are as follows:

$$V_{ij} = ez \frac{3x_i x_j - r^2 \delta_{ij}}{r^3} \quad 3.20$$

where δ_{ij} is the Kronecker symbol:

$$\delta_{ij} = \begin{cases} 1 & \text{for } i=j \\ 0 & \text{for } i \neq j \end{cases} \quad 3.21$$

The quadrupole splitting is proportional to the peak separation of the corresponding **quadrupole doublet** (Figure. 3.4.2), and so it can be determined easily from the Mössbauer spectrum. If ligand contribution is predominant in the quadrupole interaction, the individual ligands are

usually considered as point charges whose effects are calculated from eq. 6. Summing up that equation, one can prove that the quadrupole splitting is zero for the cases of the highest symmetry in coordination and charge distribution (spherical, “ideal” hexahedral, octahedral, and tetrahedral). However, the often-cited statement that the lower the symmetry, the larger the quadrupole splitting is an oversimplification, which can lead to incorrect conclusions. (For instance, the ligand contribution of the EFG for an octahedral *trans* FeA₂B₄ complex is twice that for the corresponding *cis* configuration although the former one is obviously more symmetrical.) The quadrupole splitting can also depend on the temperature (see the next section) owing to the temperature-dependent population of valence levels.

The **magnetic splitting** Δ_m observed in Mössbauer spectra arises from the Zeeman splitting of the energy levels of the nucleus provided that a nonzero **magnetic flux density**, B , exists there.

The formula of Zeeman splitting is given as follows:

$$\Delta_m = \Delta E_m \frac{c}{E_0} = -g \mu_N B \Delta m_I \frac{c}{E_0} \quad 3.22$$

where ΔE_m is the energy shift illustrated by Figure. 3.4.2 for the $I = 3/2 \rightarrow 1/2$ transition of ⁵⁷Fe (in the special case of $\Delta m_I = 1$); g_I is a nuclear factor that depends on the nuclear spin I of the nucleus; m_I is the magnetic quantum number; and μ_N is the nuclear magneton. It follows from the above formula that Δ_m has different values for the excited state (e) and for the ground state (g).

The magnetic flux density at the nucleus is proportional to the peak separation of the corresponding **magnetic sextet** (Figure. 3.4.2), and so it can be determined very easily from the Mössbauer spectrum.

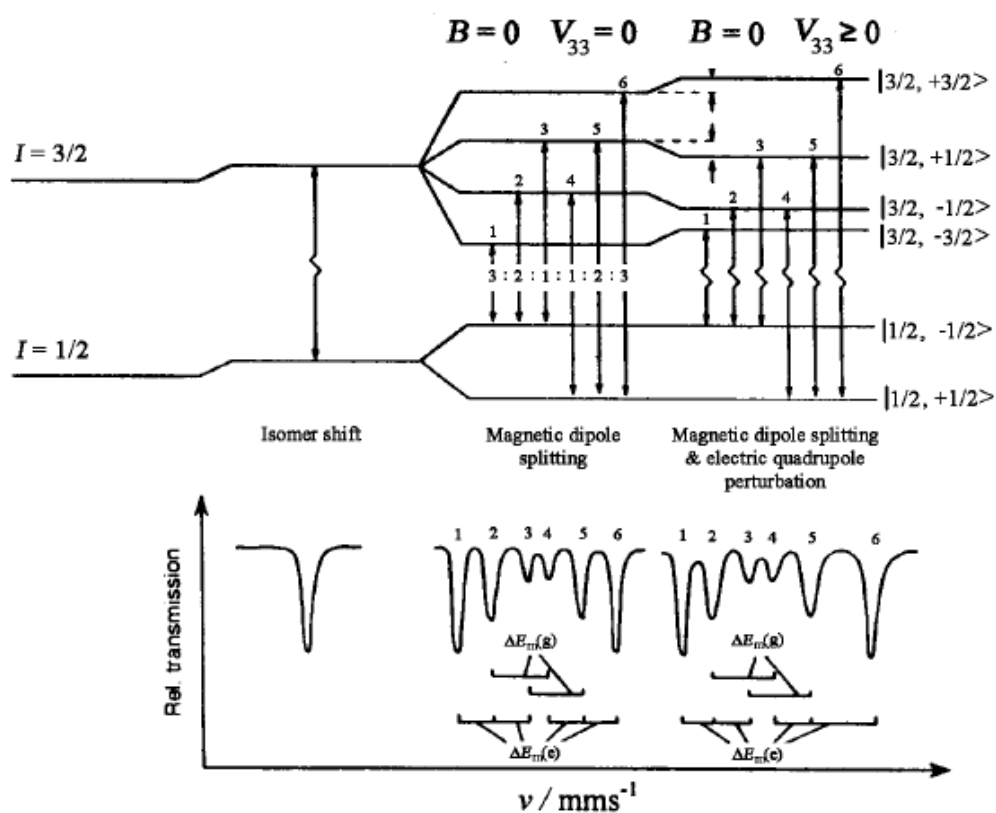


Figure 3.4 3. Magnetic splitting with and without quadrupole interaction for ^{57}Fe [10]

4. $\text{Ni}_x\text{Zn}_{(1-x)}\text{Fe}_2\text{O}_4$ $x = 1$ with BPR = 10:1

4.1 Results and Discussion

4.1.1 X-ray diffraction for BPR = 10:1

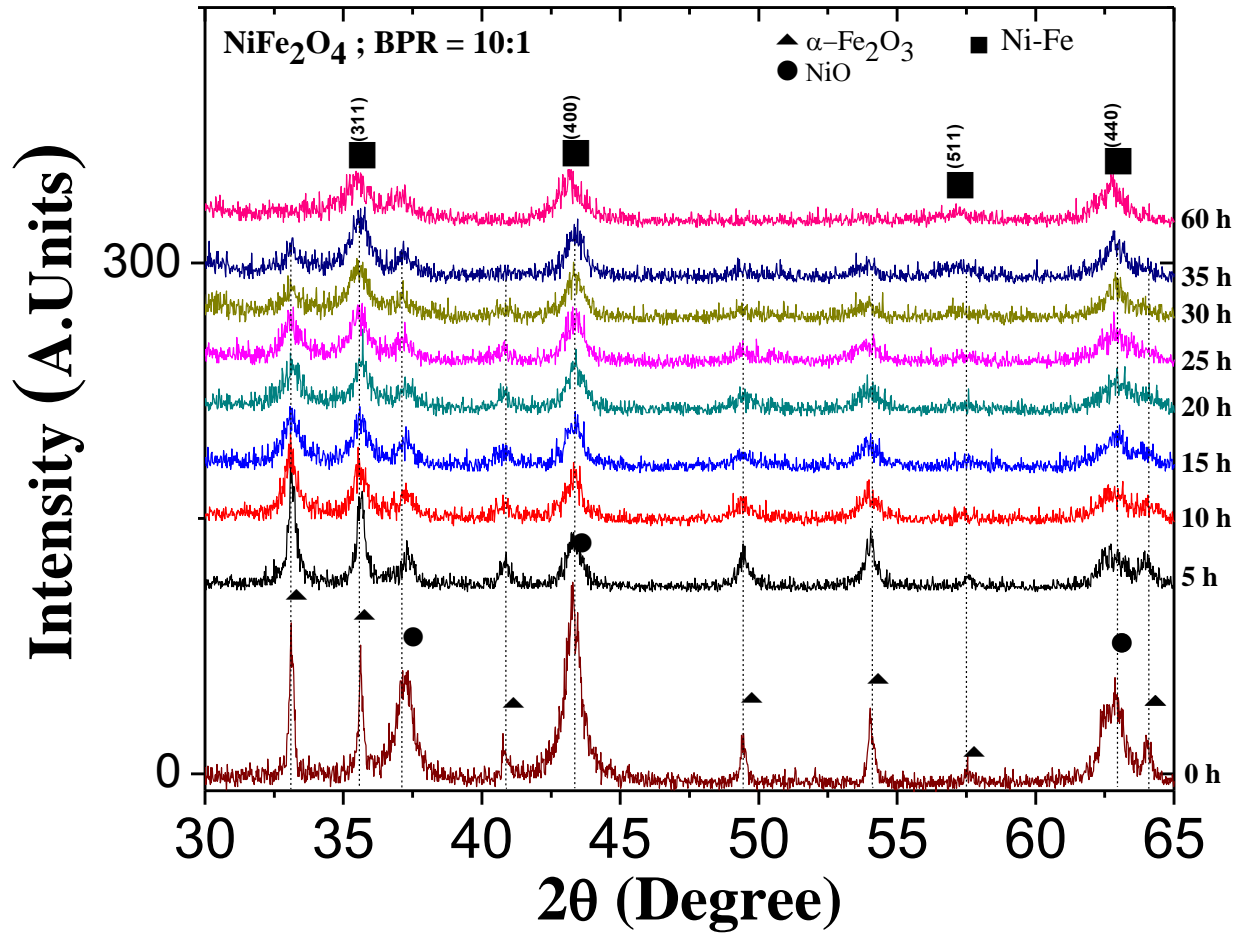


Figure 4.1 1. Shows the behavior of different diffractograms of sample NiFe_2O_4 with BPR = 10:1.

The diffractograms shown in Figure 4.1.1, are a manual mixture of NiO (ICCD PDF # 98-000-0133), and $\alpha\text{-Fe}_2\text{O}_3$ (ICCD PDF # 98-000-0240), together with the evolution with the ball mill (BPR = 10:1). Shows the XRD patterns of the different behavior of the sample with BPR = 10:1

NiFe₂O₄. We observed a decrease in intensity and a widening of the peaks after 5 hours of milling corresponding to the phases of α -Fe₂O₃ and NiO. These two precursors are held until 35 hours milling, which means that no new phase produced during milling process. This is because; the grinding time is required for the formation of NiFe₂O₄ not enough with the BPR used in this synthesis. This fact supports the hypothesis and reported that a relationship exists between the BPR used and the time it takes for the compound formed as reported Chuag et al [9, 10, 11]. However, if the milling continued for 60 hours, displayed the corresponding phase to the spinel type ferrite NiFe₂O₄, as indicated by the prominent peaks in $2\theta = 35.47^\circ$, 43.25° , 57.22° and 62.68° corresponding to (311), (400), (511) and (440) respectively.

From careful study and analysis of spectral XRD peaks and relative intensities of NiO and α -Fe₂O₃ in Figure 4.1.1, the data shown in Table 4.1.1 were obtained. There is a peak broadening as determined from the full width at half maximum (FWHM) showing a gradual increase during 5 hours from 0.46 to 0.92 been milled for 35 hours milled state for the α -Fe₂O₃. Similarly, for NiO, where milling for 5 hours showed a FWHM of 1.26 and 1.74 to 35 hours of milling.

The peaks of the phases mentioned above (NiO and α -Fe₂O₃) disappear at 60 hours of milling, reaching single phase NiFe, due the high impact energy transferred to the powder mixtures led to the destabilization of the precursor materials. The energy of impact in general causes the fracturing of the powdered materials with minimal cold welding given that the powdered precursors all belong to the ceramic material class. The ionic/covalent bonding associated with these oxides implied that extensive plastic deformation could not result since these bonds do not promote generation of dislocation as in the case of metallic bonding. Therefore, the types of structural defects that characterize the HEBM process in this study should include formation of new surfaces (via fractures), anti-site defects, breaking of bonds- especially in surfaces, grain

size refinement due to local stress and heat intensities. The particle-particle interaction leading to surface atomic diffusion there by new phase or metastable phase formation can be expected to occur during HEBM. Given that the relative thermodynamic stability of the precursor solids, NiO and α -Fe₂O₃ vary, therefore, the order of chemical reaction leading to the formation of the NiFe₂O₄ would be determined by the decomposition of the precursor solid with the least stability. From the manual mixture XRD measurement, one was not in to the peaks attribution, while, the effect of the ball milling process masked the precise monitoring of the phases with the peaks broadening, and disappearance all suggestive of the structural solution that accompanied the phases decomposition and chemical reactions with HEBM.

The Power Cell program was used in the peaks analyses in order to determine the average particle size and residual strain changes accompanying the ball milling of the material. The average particle size diameter D of the NiO and α -Fe₂O₃ ferrites phases was calculated from the reflection lines (311) using the Scherrer equation [27, 29, 30]: $D = (0.9 \lambda) / (\beta \cos \theta)$, where β (in radians) is the peak intrinsic breadth after subtraction of the instrumental contribution, λ is the X-ray wavelength and θ the diffraction (Bragg) angle. While the strain e is determined using the Stokes and Wilson relation [27, 29]: $e = (\beta / 4) \cot \theta$, from measurements of the integral breadth β of the reflection lines.

$\alpha\text{-Fe}_2\text{O}_3$					NiO				
Milling Time (h)	2 Theta	FWHM	Avarage Particle Size (nm)	Strain (10^{-3})	Milling Time (h)	2 Theta	FWHM	Avarage Particle Size (nm)	Strain (10^{-3})
0	-	-	60	0	0	-	-	20	0
5	35.63	0.47	17.80	6.37	5	62.67	1.2606	7.38	9.03
10	35.56	0.68	12.27	9.25	10	62.80	1.3407	6.94	9.58
15	35.60	0.76	10.98	10.33	15	62.90	1.3807	6.75	9.85
20	35.65	0.78	10.70	10.58	20	62.90	1.4207	6.56	10.13
25	35.56	0.84	9.93	11.43	25	62.86	1.7009	5.47	12.14
30	35.54	0.90	9.27	12.25	30	62.89	1.7209	5.41	12.28
35	35.63	0.92	9.07	12.50	35	62.87	1.7409	5.35	12.42

Table 4.1.1. Particle size and strain of NiFe_2O_4 in the unmilled and different milled states.

It is instructive to comment on the evolution of the average strain impacted on the materials with milling time. From measurements of X-ray diffraction, the average strain associated with the different precursors is observed a gradual increase of stress at 35 hours of grinding with reference to the first 5 hours of grinding. Analogously as seen in the NiO at 35 hours with reference to the 5 hours of grinding. These behaviors are very similar to those obtained by Bid et al. [12, 13, 14, 15]. Along with the evolution of the average particle size, it is evident that the increase in tension by $\alpha\text{-Fe}_2\text{O}_3$ sample with respect to the sample of NiO, which reaches values of 12.84×10^{-3} and 4.55×10^{-3} respectively. Furthermore, the very minimum corresponding change in the particle size for milling times greater.

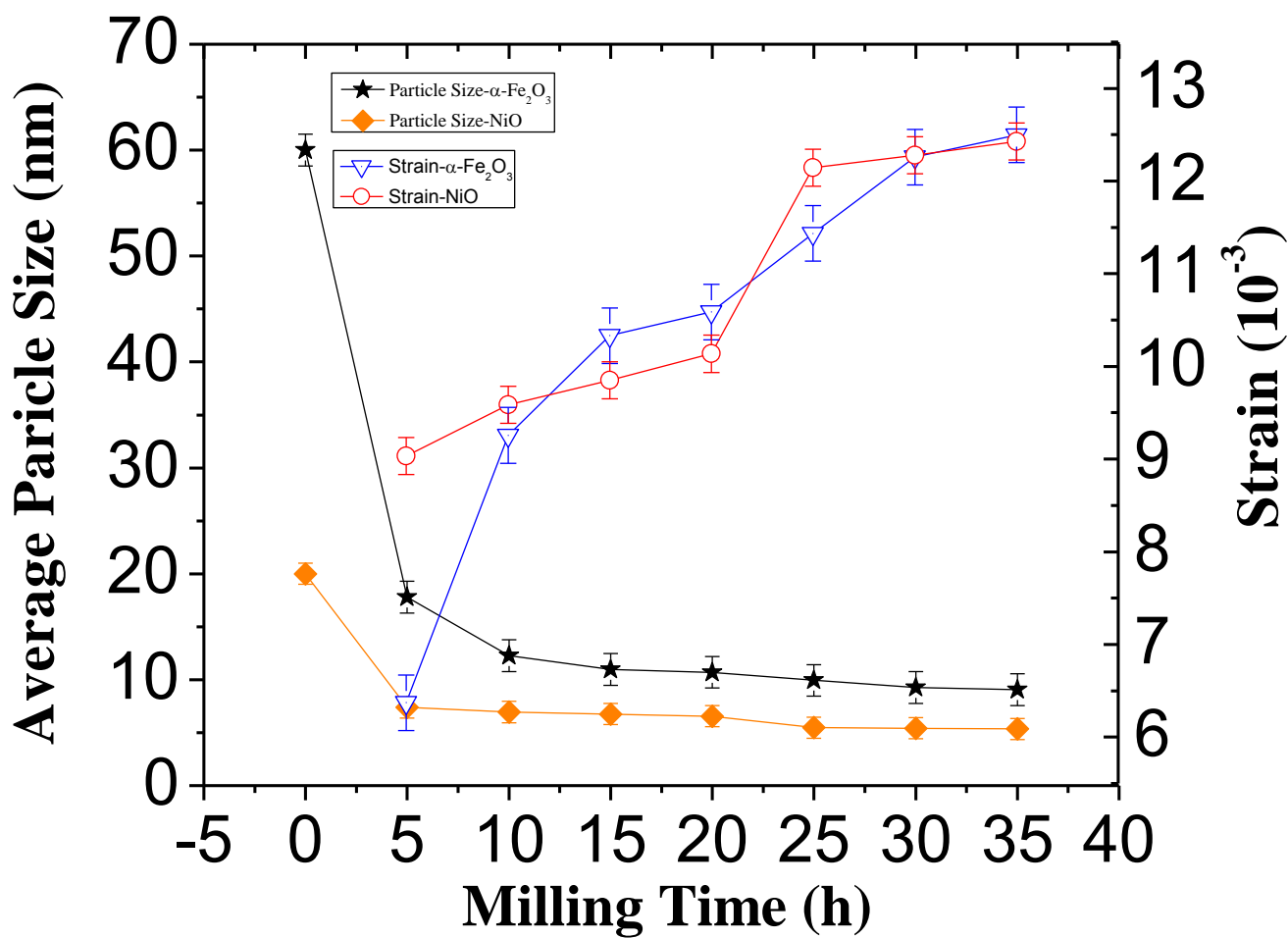


Figure 4.1 2. Evolution of particle size and strain of formed NiFe_2O_4 (BPR = 10:1) as a function of ball milling time.

4.1.2 Measurements of magnetization for BPR = 10:1

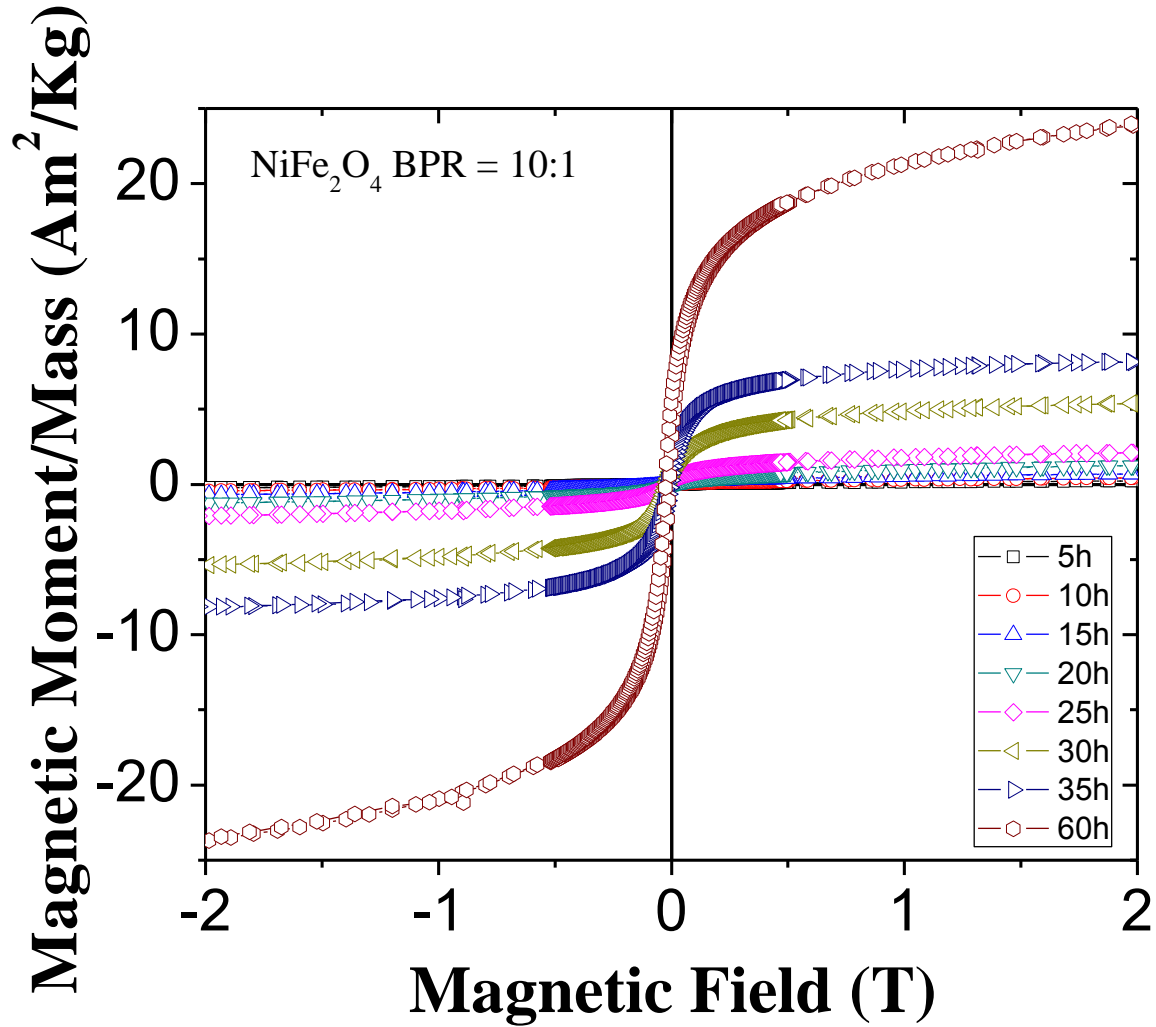


Figure 4.1.3. VSM measurements corresponding of NiFe_2O_4 for BPR 10:1

The magnetic properties of NiFe have been investigated by magnetization hysteresis curve measurements at room temperature. Figure 4.1.3 shows magnetization hysteresis curves measured at room temperature for the NiFe samples milled for various times. The specific saturation magnetization values are progressively increasing as the milling time also makes, observed a sudden, when the sample is ground to 60 hours. This behavior is in agreement with

X-ray measurements shown in the figure 4.1.1, in which there is a progressive reduction in the particle size and an increase in strain, as milling time increases. It should be noted that with some possible techniques to extract information from each of the reagents. However, VSM measurements, it is possible to separately identify each one of the precursors, because this technique gives global information of all the materials involved in the reaction. Based on this observation, we can say that the progressive increase of the saturation magnetization is due to the reaction of the precursors progressively and ends in the formation of the single phase NiFe, as indicated by X-ray measurements, which are observed peaks corresponding to said phase at 60 hours of milling. For its part, the coercivity shows a gradual decrease from its maximum value to approximately zero with respect to the milling time, due to reduced particle size (Figure 4.1.1) as reported [16].

It is known that the Ni ferrite has the structure inverse, with all the Ni^{2+} ions in B sites and the Fe^{3+} ions evenly divided between A and B sites. The moments of the Fe^{3+} ions therefore cancel, and the net moment is simply that of the Ni^{2+} ion, which is $2\mu_B$ [9,10]. Generalizing on this, we conclude that the saturation magnetization μ_H of any inverse ferrite is simply the moment on the divalent ion. However, in the formation of NiFe synthesized by HEBM technique, there is a mixture of antiferromagnetic material such as NiO and $\alpha\text{-Fe}_2\text{O}_3$, for the early stages of milling, that progressively react to form ferrite NiFe. In this process of Ni^{2+} ions will fall into place at sites B, to go gradually contributing to the sample magnetization, analogous to what happens in bulk ferrite. This arrangement of Ni^{2+} ions is what is seen as a gradual increase in the saturation magnetization. Furthermore, the coercivity is progressively reduced due to the reduction in particle size. This decrease causes a decrease in the magnetic anisotropy energy of the sample, creating magnetic resistance to decrease, which leads to a reduction in the values of coercivity.

Milling Time (h)	Saturation specific Magnetization- M_s (Am^2/Kg)	Coercivity- H_{ci} (mT)
5	0.27	32.4
10	0.54	16.1
15	0.87	13.8
20	5.23	10.6
25	8.44	6.75
30	8.05	4.60
35	10.30	4.42
60	46.39	1.97

Table 4.1.2. Saturation specific magnetization and coercivity of NiFe_2O_4 in different milling time.

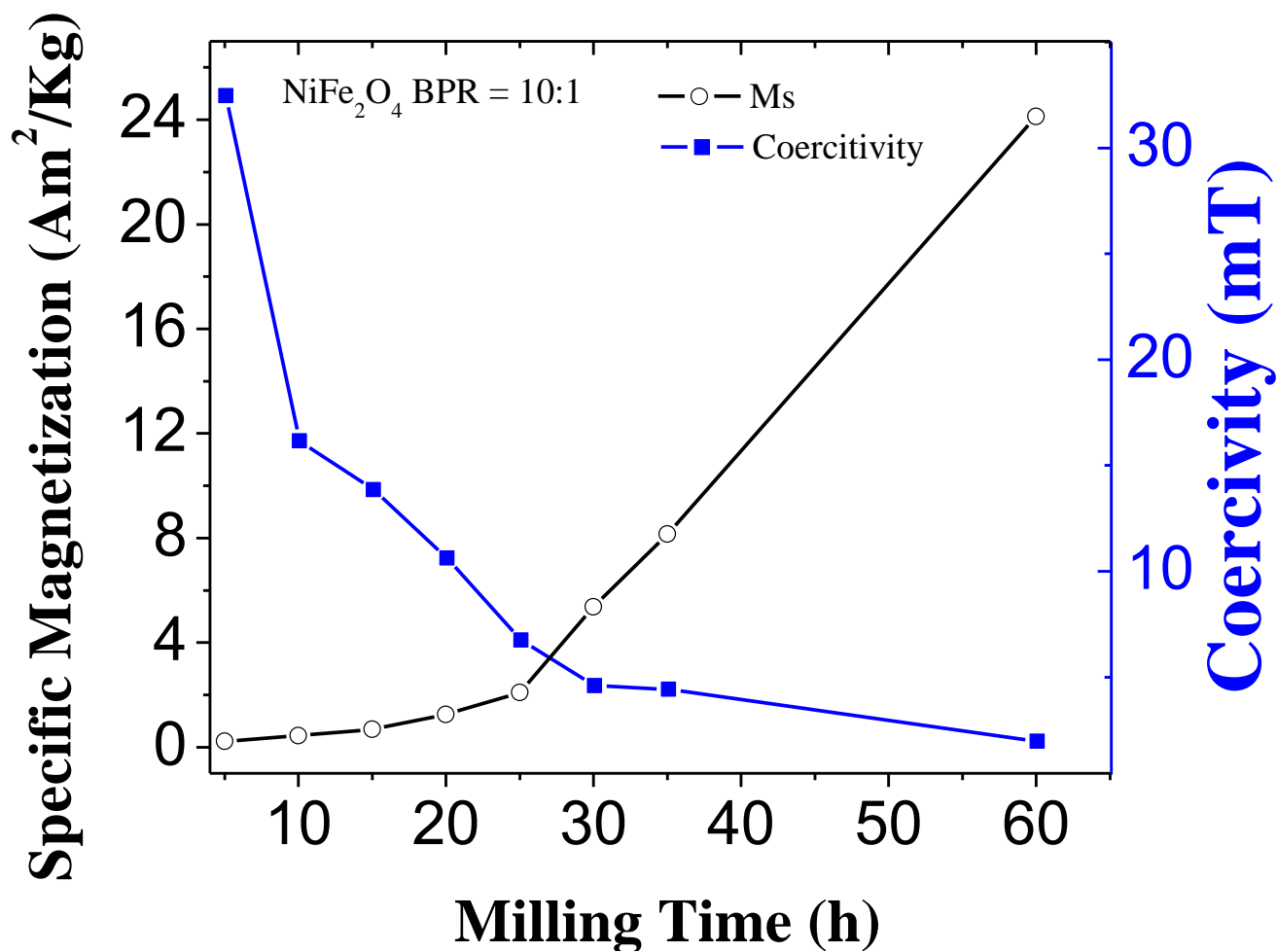


Figure 4.1.4. Evolution of coercivity and saturation magnetization as a function of ball milling of NiFe_2O_4 for BPR 10:1

4.1.3 Measurements of Mössbauer for BPR = 10:1

The room temperatures Mössbauer spectroscopic measurements carried out after 5 hours intervals of ball milled materials are shown in figure 4.1.5. The spectra helped to elucidate on the nature of the characteristics of the Fe sites in the materials, especially with respect to their magnetic order, and electronic configuration. The five hours ball milled state is comprised of prominent sextet's peaks with a central doublet. Where this double non-magnetic central has increased in intensity to higher milling times, contrary to the sextet's peaks which decrease their intensity and widen as the milling time increases to become asymmetrical. With these observations, one authority state that the mechanochemical synthesis process was achieved via the progressive consumption of the precursor materials as evidenced by the reduction in intensity of the sextet peaks and the simultaneous evolution of the central non magnetic peaks. Also, shown in Figure 4.1.5, a significant reduction of the sixth characteristic of the spectrum, this decrease is due to the decrease of the particle size and the appearance of NiFe phase in the sample, related to the increase of the saturation magnetization shown in Figure 4.1.3.

In fitting the Mössbauer spectra, the hyperfine distribution model according to Rancourt and Ping [16, 18, 19, 20] was used. This meant that as much as possible the fitting was carried out in order to obtain the best fit based on the internal field distribution novel where correlation from one spectrum to another in succession was carefully singlet. Starting from the fitting of the manual mix unmilled material while translates to the fitting of the fitting of the as-supplied α - Fe_2O_3 materials, the 5 hours and successively milled materials were carried out.

The component of the spectrum for the 35 hours milled state which account for after 9.09 % of the material was fitted with an internal magnetic field of 509.65 kOe. If showed be noted here, that the isomer shift corresponding to this site was 0.192 mm/s while the quadrupole splitting of -

0.125 mm/s and line broadening based on peaks full width at high maximum (FWHM) was 0.154 mm/s indicated that structural formation or transition occurred at this stage. Given that the reference α -Fe calibration internal magnetic field is 330 kOe, therefore, one could speculate that these sites correspond to Fe sites associated with a lot of disorder such that reduction of Fe^{3+} to Fe occurred a certain degree. The totality of this observation points to progressive evolution of the materials with ball milling, while the superparamagnetic state is not quite reached for the 60 hours milled state. It could be suggested that the milled materials reached a stage where further milling could display the mechanochemical synthesis to any direction, i.e., a sort of transition dead state.

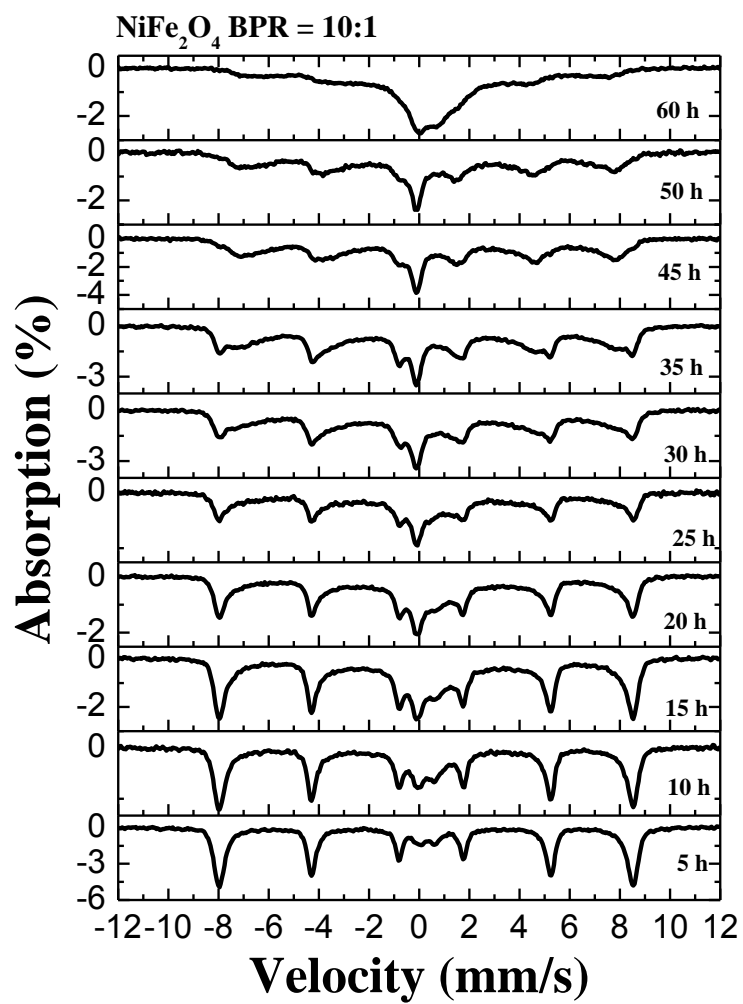


Figure 4.1 5. Mössbauer spectra of NiFe_2O_4 for BPR = 10:1

4.2. Conclusions

- Achieved ferrite phase NiFe_2O_4 at 60 hours of milling as evidenced by X-ray spectra
- For the ferrite NiFe , there is a dependence of the saturation magnetization and the coercivity with milling time, reaching a maximum at the saturation magnetization to 60 hours of milling.
- Superparamagnetic phase is evident at 60 hours milling shown by the Mössbauer spectrum.

5. $\text{Ni}_x\text{Zn}_{(1-x)}\text{Fe}_2\text{O}_4$ $x = 1$ with BPR = 20:1

5.1 X-Ray Diffraction for BPR = 20:1

The mechanochemical synthesis reaction as started under the experimental was carefully monitored by using powder XRD measurements to determine extent of reactions as a function of time starting with the manual mixture. The spectral peaks for the NiO and $\alpha\text{-Fe}_2\text{O}_3$ phases were matched with corresponding JSPDF files reference as NiO (ICCD PDF#98-000-0133) and $\alpha\text{-Fe}_2\text{O}_3$ (ICCD PDF#98-000-0240) as shown in figure 5.1.1.

Close examination of the XRD patterns show in Figure 5.1.1, shows that the reaction leading to the formation of the single phase NiFe_2O_4 commenced within 5 hours of ball milling and continued subsequently. The peaks of NiO centered around $2\theta = 35^\circ$ and $2\theta = 62\text{-}65^\circ$ range could still be seen at 15 hours of milling. It can be deduced that the single phase NiFe_2O_4 formed by the formation of disordered followed by the intercalation of Ni^{2+} in the matrix leading to the eventual formation of NiFe_2O_4 . After 15 hr of grinding the broadened peaks and $2\theta = 35\text{-}36^\circ$ and $2\theta = 42\text{-}45^\circ$ showed that a lot of structural disorder accompanied the ball milling process.

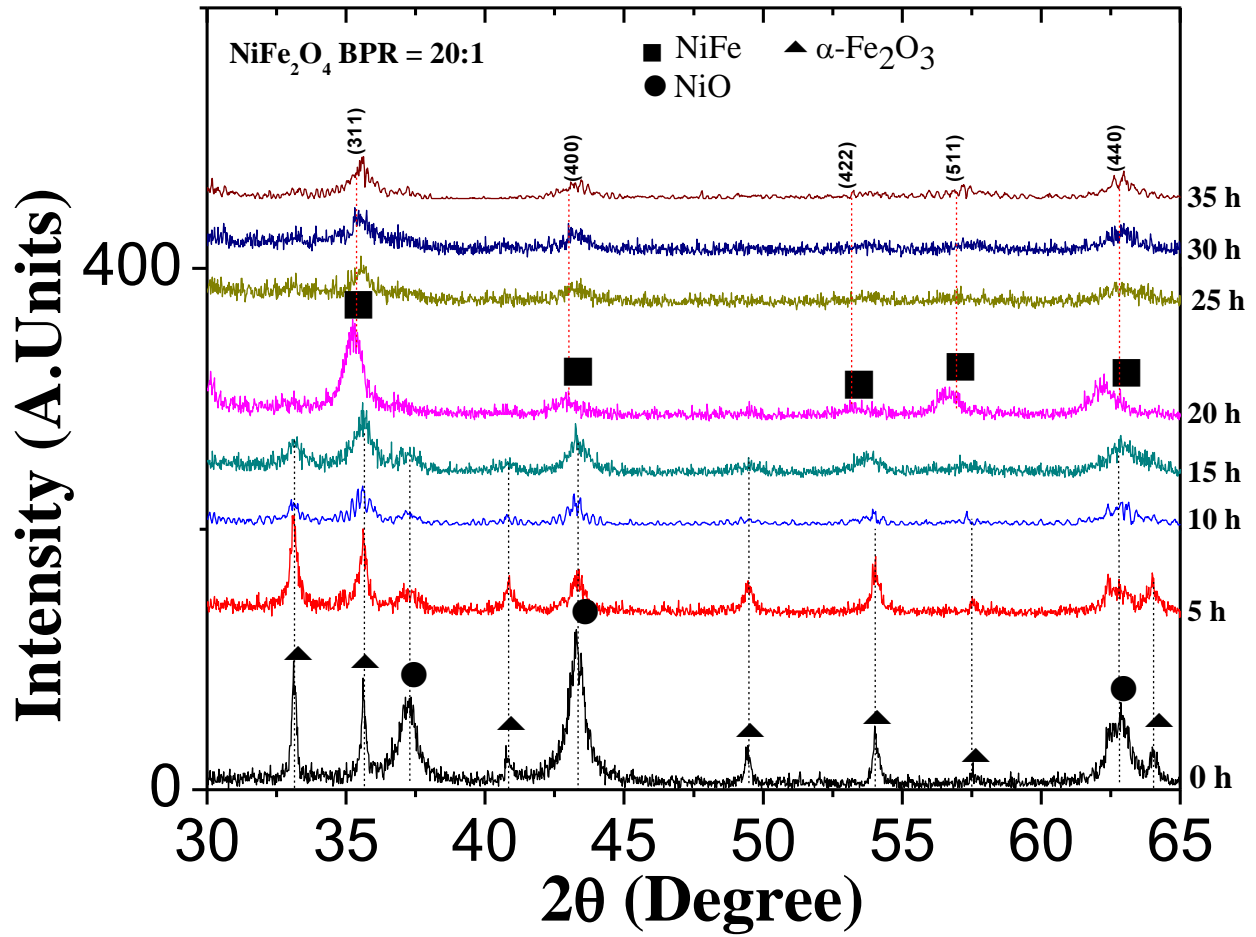


Figure 5.1 1. XRD spectra and NiFe_2O_4 for BPR 20:1

The structural disorder leading to the formation of single phase NiFe_2O_4 was accompanied by the rapid particle size reduction of the precursor solids due to the high impacts energy transferred to the particles during the milling. With the particle size reduction, the eventual inter-mixing leading to the formation of the single phase occurred. The further, broadening and loss of peaks intensities from 15 hrs to 35 hours, demonstrated that loss of crystallinity of the new phase, culminated in the formation of highly metastable material. The Metastability in the sample is

possible to identify because of the high amorphization of the sample, shown in X-ray spectra, showing a decrease in peak intensity, along with reducing its width, which is characteristic of the phase metastable as it was reported. It was not possible to extrapolate or deduce further the state of the material given that only five broad peaks could be discerned beyond 20 hours of ball milling.

From careful examination and analyses of XRD spectral peaks and relative intensities, single phase NiFe_2O_4 identified as NiFe in Figure 5.1.2, the data displayed in Table 5.1.1 were obtained. The spectral position that corresponding to the (400) reflection as a function of ball milling time showed that the peaks shifted to lower angles from $2\theta = 43.31^\circ$ to 42.88° , for the 5 hours and 20 hours state of milling. The 30 hours and 35 hrs milled states displayed XRD peaks for the (400) reflection that exhibited reversion to higher angle positions corresponding to $2\theta = 43.12^\circ$ and 43.28° respectively. While the spectral position to lower angles and reverted to higher angle shifting, the broadening of the peaks as determined from the full width at half maximum (FWHM) showed a progressive increase from 0.54 for the 5 hrs milled state, to 1.24 for the 35 hrs milled state.

Given the extensive broadening of the spectral peaks from the 5 hrs milled state and the 35 hrs milled state showed that the HEBM process employed in this study was indeed effective in engendering the mechanochemical synthesis process. The high impact energy transferred to the powder mixtures led to the destabilization of the precursor materials. The energy of impact in general causes the fracturing of the powdered materials with minimal cold welding given that the powdered precursors all belong to the ceramic material class. The ionic/covalent bonding associated with these oxides implied that extensive plastic deformation could not result since these bonds do not promote generation of dislocation as in the case of metallic bonding.

Therefore, the types of structural defects that characterize the HEBM process in this study should include formation of new surfaces (via fractures), anti-site defects, breaking of bonds especially in surfaces, grain size refinement due to local stress and heat intensities.

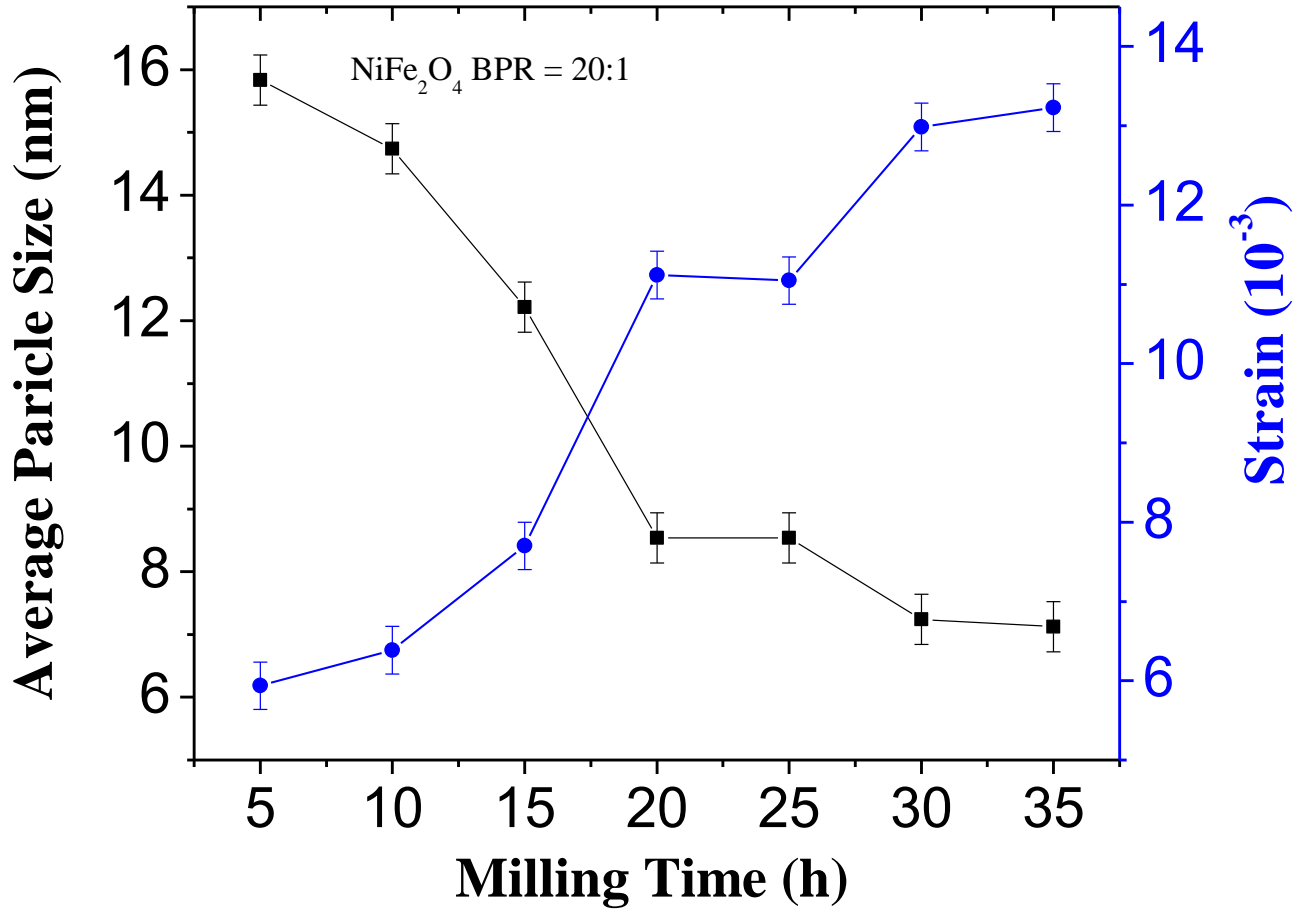


Figure 5.1 2. Average particle size and strain of NiFe_2O_4 for BPR 20: 1 as a function of time ball milling

The addition of acetone as a processing agent promoter helped to ensure intimate mixing of the powder precursor materials such that the inter-diffusion accompanying the particle size reduction

in enhanced. The use of XRD measurement as was carried out could not be used to explore the intricate sequential steps associated with the mechano-chemical synthesis process alone, hence the integration of other measuring technique as Mössbauer spectroscopy and vibrating sample magnetometer types.

Milling Time (h)	2 Theta	FWHM	Avarage Particle Size (nm)	Strain (10^{-3})
5	43.316	0.54	15.83	5.93
10	43.264	0.58	14.74	6.38
15	43.288	0.70	12.21	7.70
20	42.88	1.00	8.53	11.11
25	43.122	1.18	8.53	11.04
30	43.28	1.20	7.24	12.98
35	43.211	1.24	7.12	13.22

Table 5.1.1. Particle size and strain of NiFe_2O_4 in the unmilled and different milled states.

The general or overall evolution trend between the particle size and the average strain can be reconciled based on two competing factors, namely the need for the formation of the equilibrium solids solution single phase and the refinement of the particles of the realized phase. Given that for the material systems involved in the mechanochemical synthesis, limitation of diffusion substances for the cations causes local structural rearrangement leading to the formation of overall metastable single phase solid solution imbued with significant structural defects as evidenced by the reflections of the diffracting phase from the XRD measurements. Given the peaks broadening, and peaks disappearance, it is possible that limited amorphous phase corresponding to the same average composition of NiFe_2O_4 accompanied the highly defective crystalline state of the same solid solution phase.

5.2 Measurements of Magnetization for BPR = 20:1

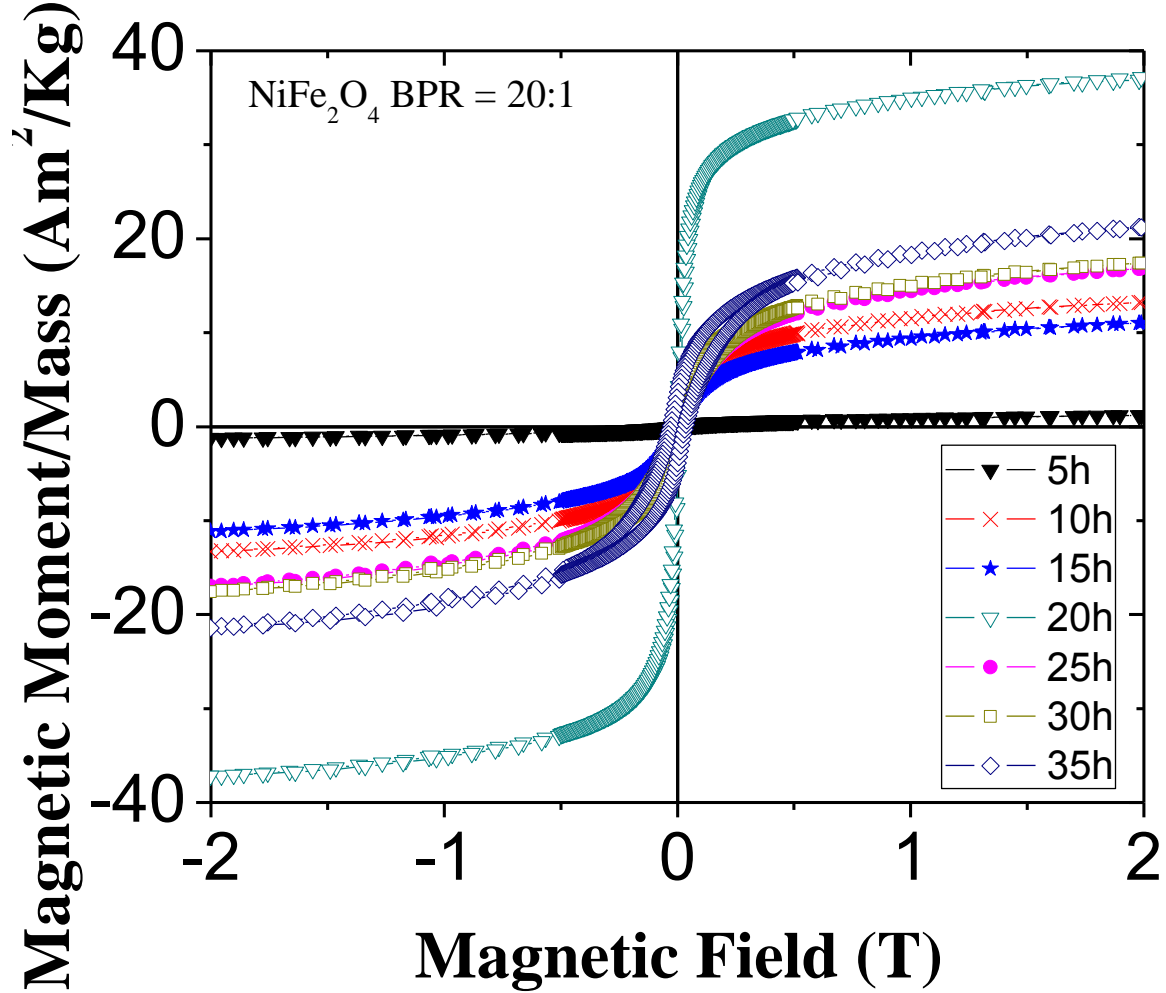


Figure 5.1 3. VSM measurements corresponding of NiFe_2O_4 for BPR 20:1

The vibrating sample magnetometer measurement showing the variation of the saturation specific magnetization (M_s) as a function of applied magnetic field show in figure 5.1.3, where the overall magnetization behavior of the milled materials are shown. Examination of the plots shows that the behaviors of the milled materials corresponding to the 5 hr, 10 hr, 15 hrs and 20

hrs milled state, displayed increasing saturation magnetization. The tendency displayed for these three values is in sharp contrast to the plots obtained for the 25 hrs, 30 hrs and 35 hrs milled states. Overall, these two groups of the milled materials are substantially consistent with the XRD measurements analysis displayed in figure 5.1.1, in which drastic change in particle size and average strain associated with the materials are observed. While it was possible to extract contributions arising from the individual precursor materials as a function of milling time, the same could not be understood for the VSM measurements. This is majority due to the fact that the entire material contribution is registered in the hysteresis loop. This said the overall pattern change in the hysteresis profile can be used to identify the progressive mechanochemical reactions leading to decreasing precursor materials with increasing single phase solid solution consisting of NiFe_2O_4 . Based on this observation, it can be stated that the decreasing saturation magnetization was caused by the progressive formation particles associated with the NiFe_2O_4 while the coercivity observed in the 5-20 hrs milled states are due to the magnetic phases whose states are due to the magnetic phases whose particle sizes were not small enough to yield superparamagnetic behavior. These could be due to trace amounts of $\alpha\text{-Fe}_2\text{O}_3$, NiO , and relatively large NiFe_2O_4 metastable phases. The overall profile of the magnetization plots as shown in figure 5.1.4 is therefore very instructive of the milled states of the materials.

The fact that HEBM causes the formation of metastable phases which are substantially reduced in size (despite the existence of particles agglomeration, and inter-particle interaction, etc) the contribution due to the overall magnetic behavior and the VSM plots shown in figure 5.1.3. Thus, preferential distribution of Ni^{2+} cations in the octahedral sites can be used to reconcile the tendencies and overall behavior observed. Firstly, terminating surfaces of the spinel phases are expected to be the low value (h, k, l) phase such as (110) and (111) hyper and as a result, the

coercivity determination for the milled materials can be explained. Had the materials been in equilibrium states, without inter-particle interactions, the contributions of the surface cationic distribution would be less, and zero-coercivity sigmoid shaped hysteresis loop associated with superparamagnetic phenomenon would holds way.

Milling Time (h)	Saturation specific Magnetization- M_s (Am^2/Kg)	Coercivity- H_{ci} (mT)
5	1.25	15.40
10	13.42	8.80
15	11.25	10.50
20	37.34	1.30
25	17.12	19.80
30	17.7	21.64
35	21.58	26.65

Table 5.1.2. Saturation specific magnetization and coercivity of NiFe_2O_4 in different milling time.

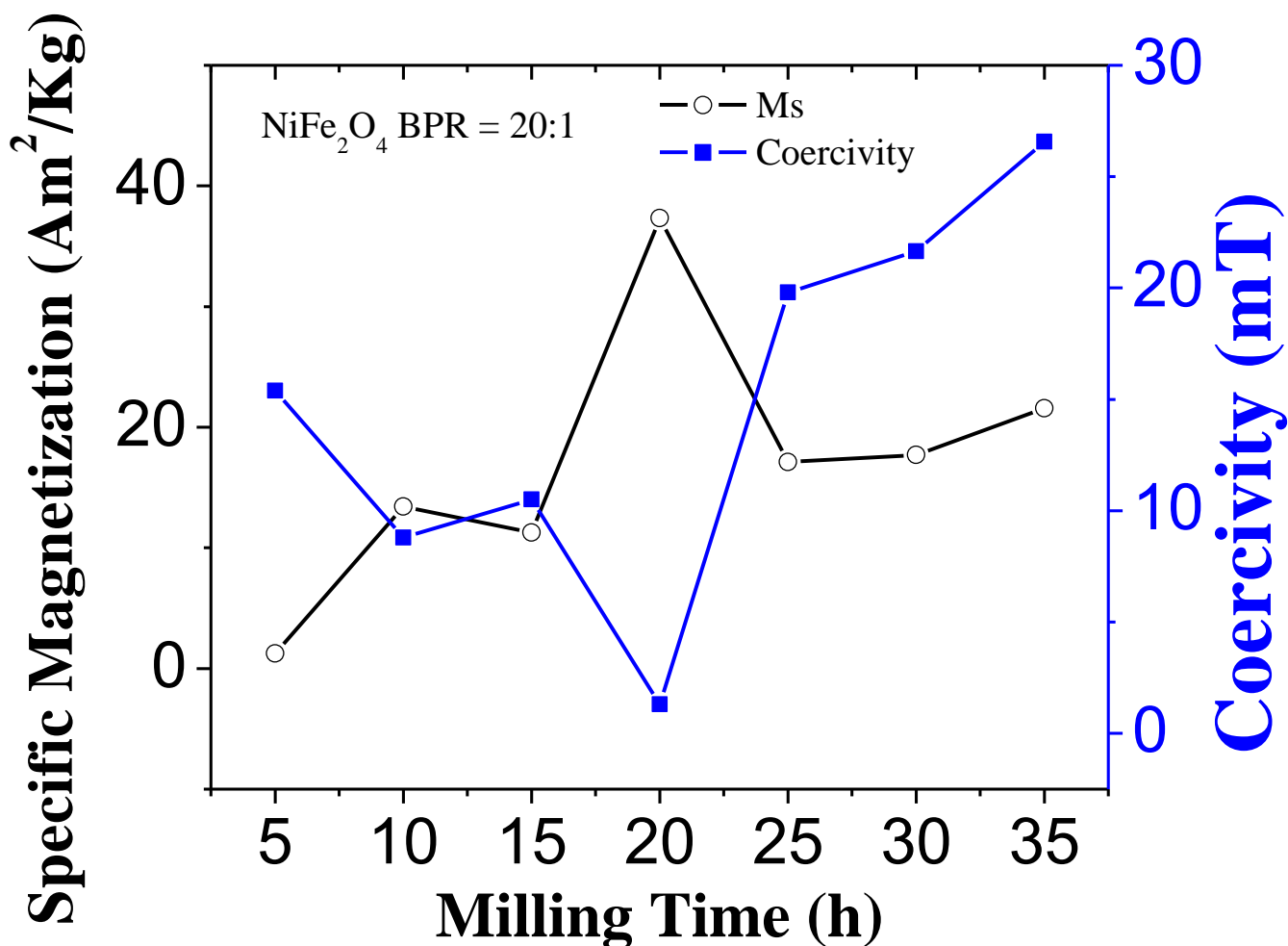


Figure 5.1.4. Evolution of coercivity and saturation magnetization as a function of ball milling of NiFe_2O_4 for BPR 20:1

5.3 Measurements of Mössbauer for BPR = 20:1

The figure 5.1.5 shows the room temperature Mössbauer spectroscopic measurements of the ball milled materials mixtures were carried out after 5 hours intervals to corroborate the XRD, and VSM corresponding measurement. The five hours ball milled state is comprised of prominent sextet's peaks with a central doublet. In comparison to the 10 hours milled, material spectrum,

the sharp sextet peaks similarly observed for the 5 hrs milled state in seen too have diminished in intensity while row very broad sextet peaks emerged. Further the central doublet peaks observed in the 5 hrs milled state can be seen to have adopted or more any metrical shape, in addition to some broadening. With these observations, one authoritarian state that the mechanochemical synthesis process was achieved via the progressive consumption of the precursor materials as evidenced by the reduction in intensity of the sextet peaks and the simultaneous evolution of the central non magnetic peaks.

The component of the spectrum for the 20 hours milled state which account for after 9.74 % of the material was fitted with an internal magnetic field of 507.89 kOe. If showed be noted here, that the isomer shift corresponding to this site was -0.27 mm/s while the quadrupole splitting of - 1.13 mm/s and line broadening based an peaks full with at high maximum (FWHM) was 0.28 mm/s indicated that structural formation or transition occurred at this stage. This stage characteristically distinguished the 10 hours and 15 hrs milled state from the 25 hr, 30 hr, and 35 hr milled state that were fitted with 3Fe sites respectively Given that the reference a-Fe calibration internal magnetic field is 330 kOe, therefore, one could speculate that these sites correspond to Fe sites assousted with a lot of disorded such that reduction of Fe^{3+} to Fe occurred a certain degree. The totality of this observation points to progressive evolution of the materials with ball milling. It could be suggested that the milled materials reached a stage where further milling could display the mechanochemical synthesis to any direction, i.e, a sort of transition dead state.

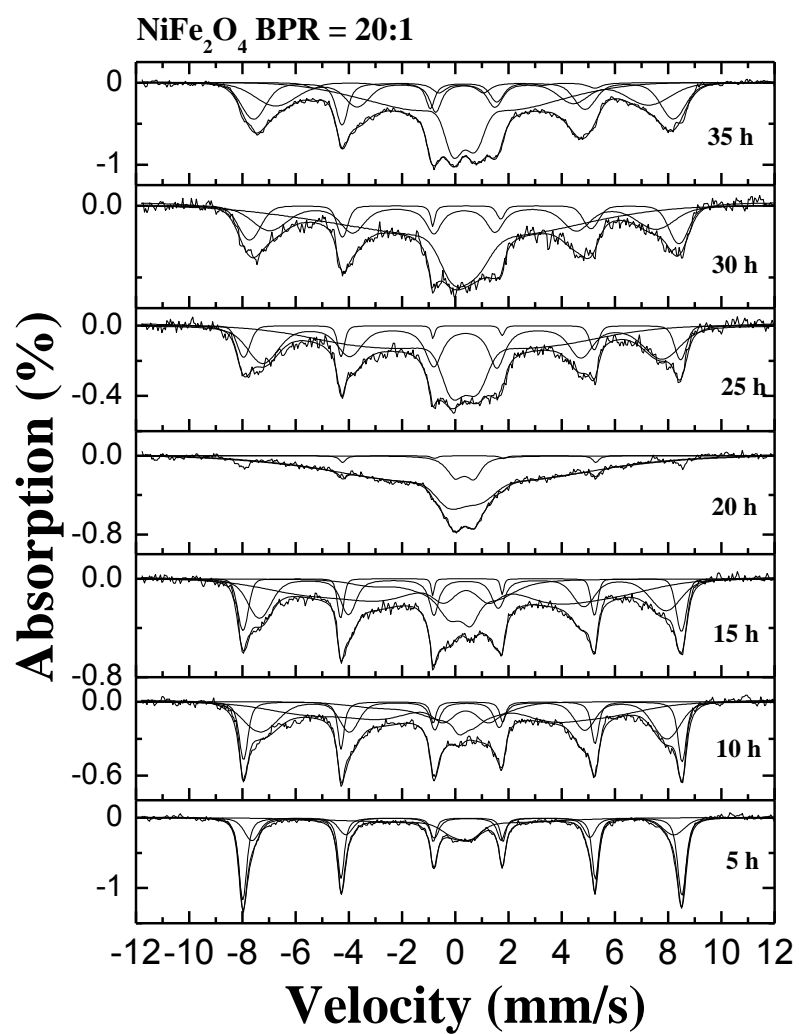


Figure 5.1 5. Mössbauer spectra of NiFe₂O₄ for BPR 20:1

6.2Ni_xZn_(1-x)Fe₂O₄ x = 1 (NiFe₂O₄) with BPR = 40:1

6.2.2. X-ray diffraction for BPR = 40:1

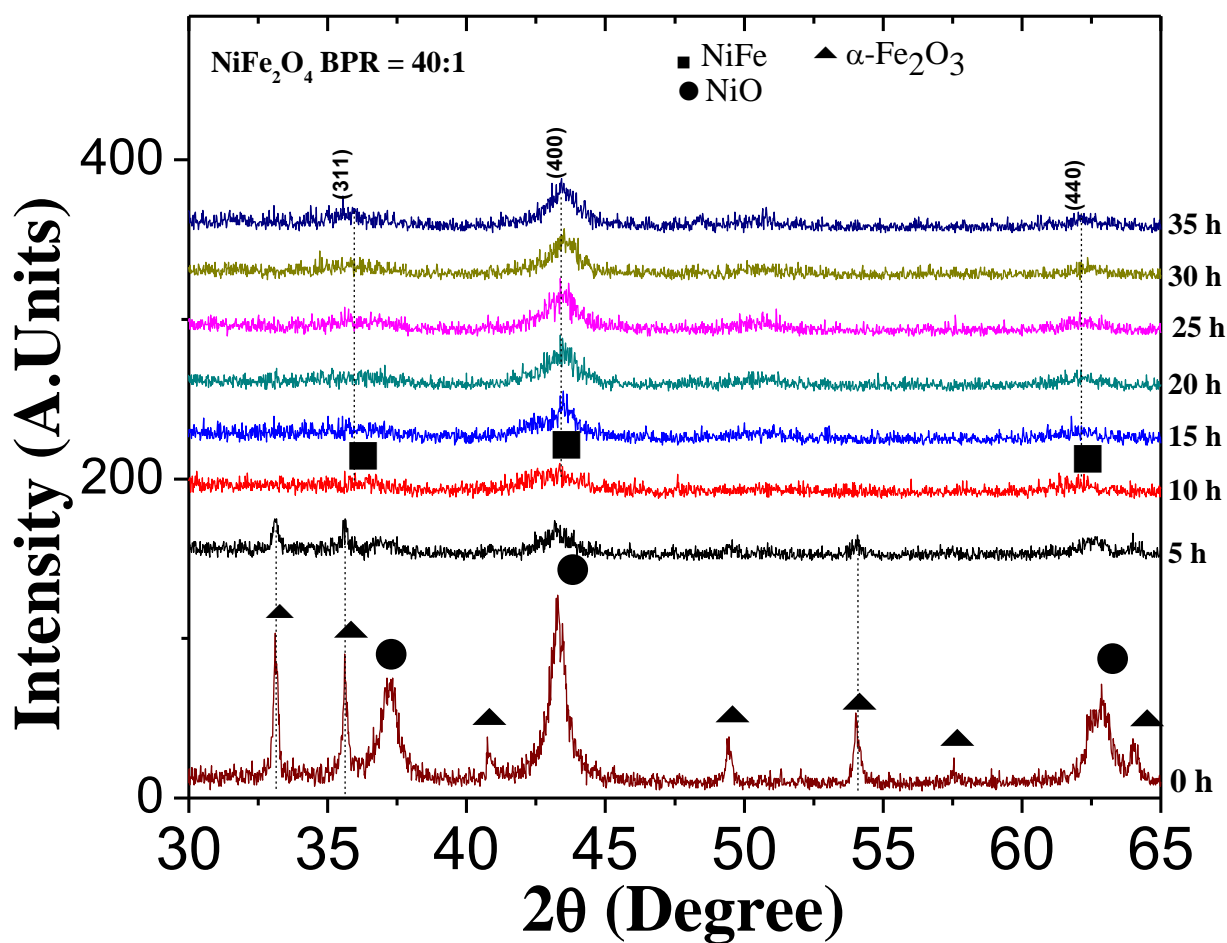


Figure 6.1 1. X-ray diffraction spectra of the formation of NiFe₂O₄ during mechanochemical synthesis for BPR = 40:1.

The X-ray diffraction pattern of the starting powder is indexed for single-phase NiFe spinel. Figure 6.1.1 shows XRD data for samples milled from 5 to 35 hours together with those for the raw sample. Unlike the two synthesis (BPR = 10:1 and 20:1) to 5 hours of milling, the formation of the single phase NiFe_2O_4 has been noticed clearly due to the appearance of the three peaks corresponding to (311), (400) and (440), reflections at $2\theta = 36.15^\circ$, 43.49° and 62.22° , respectively, as reported [21, 22, 23, 24, 25]. Compared with other synthesis (BPR = 10:1 and 20:1) phases NiO, and $\alpha\text{-Fe}_2\text{O}_3$, experience rapid disappearance dramatically. This suggests greater BPR leads to rapid formation as spinel phase. As the milling time increases, there is a progressive broadening and reduced intensity peaks characteristic of NiFe phase until 35 hours of milling. This broadening of peaks is related to a variation in particle size, structural defects, high amount of effort and possible occurrence of a superparamagnetic phase.

To check whether there is a relationship between the peak broadening the grain size reduction and strain, we made a measure of the average grain size and strain as a function of milling time. From the XRD measurements, the average strain associated the formation of single solid solution phase, NiFe_2O_4 showed progressive increase up to 35 hours of milling. Together with the evolution of the average particle size, it is evident that increase of average strain in the first regime up to 15 hrs of milling time, while the terminal stage corresponding to the 20 hours, 30 hours and 35 hours milled stage exhibited minimal change in average strain and corresponding very minimal change in particle size.

Given the extensive broadening of the spectral peaks from the 5 hrs milled state and the 35 hrs milled state showed that the HEBM process employed in this study was indeed effective in engendering the mechanochemical synthesis process. The high impact energy transferred to the powder mixtures led to the destabilization of the precursor materials. The energy of impact in

general causes the fracturing of the powdered materials with minimal cold welding given that the powdered precursors all belong to the ceramic material class. The ionic/covalent bonding associated with these oxides implied that extensive plastic deformation could not result since these bonds do not promote generation of dislocation as in the case of metallic bonding. Therefore, the types of structural defects that characterize the HEBM process in this study should include formation of new surfaces (via fractures), anti-site defects, breaking of bonds- especially in surfaces, grain size refinement due to local stress and heat intensities.

Milling Time (h)	2 Theta	FWHM	Average Particle Size (nm)	Strain (10^{-3})
5	43.22	0.50	17.09	5.51
10	43.35	0.68	12.59	7.46
15	43.47	0.86	9.94	9.41
20	43.51	0.96	8.91	10.50
25	43.48	0.98	8.73	10.72
30	43.54	1.20	7.13	13.12
35	43.47	1.38	6.20	15.11

Table 6.1.1. Particle size and strain of NiFe_2O_4 in the unmilled and different milled states.

The general or overall evolution trend between the particle size and the average strain can be reconciled based on two competing factors, namely the need for the formation of the equilibrium solids solution single phase and the refinement of the particles of the realized phase. Given that for the material systems involved in the mechanochemical synthesis, limitation of diffusion substances for the cations causes local structural rearrangement leading to the formation of overall metastable single phase solid solution imbued with significant structural defects as evidenced by the reflections of the diffracting phase from the XRD measurements.

Figure 6.1.2 shows the evolution of grain size for the mechanochemical synthesized of NiFe_2O_4 for different milling times. However, after 10 hours of milling there is a reduction in average particle size to a value of 52 nm. This value is maintained until the 20 hours of milling which again decays to a value of 46 nm for the 25 hours of milling. This value becomes increased for 30 hours of grinding to a value of 52 nm. This increase is the result of a fracture process and soldier suffering from cold samples during high energy milling, causing agglomeration of the sample, generating an increase in average particle size.

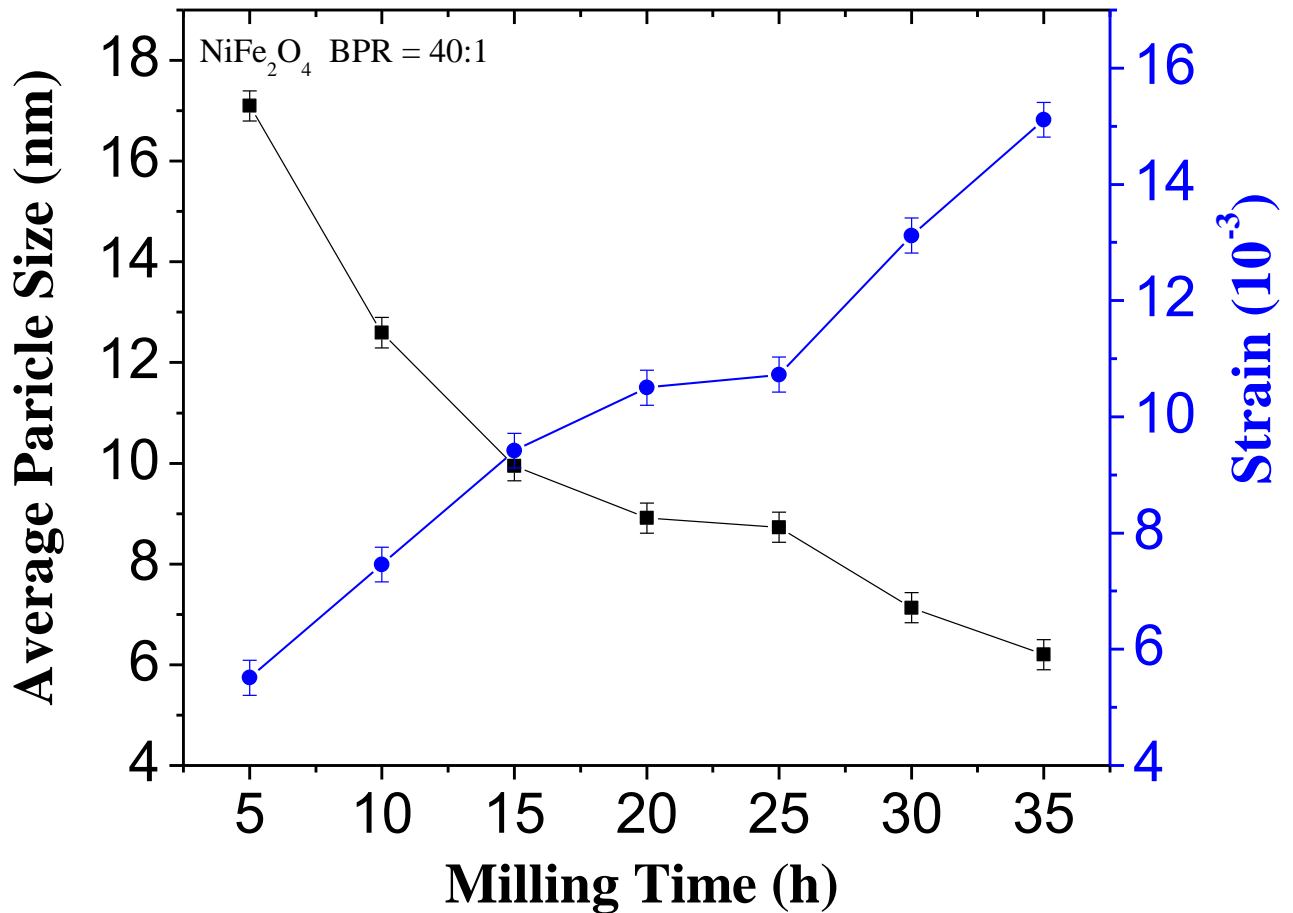


Figure 6.1 2. Evolution of paticle size and strain of formed NiFe_2O_4 (BPR = 40:1) as a funtion of ball milling time.

6.2.2. Measurements of Magnetization for BPR = 40:1

The overall magnetic properties of the entire mass comprising of the unreacted and formed materials are shown in the corresponding figure 6.1.3. In contrast to the X-ray diffraction measurements where characteristic peaks corresponding to the different material phases present are discerned, the VSM plots represent the overall contribution due to the entire material mixture. From XRD measurement analyses, the amount of NiFe_2O_4 formed after 5 hours, and as a result we attribute the change in the VSM plot between the unreacted mixture and the 5 hours ball milled state to the formation of NiFe_2O_4 , and the size reduction of the unreacted mass.

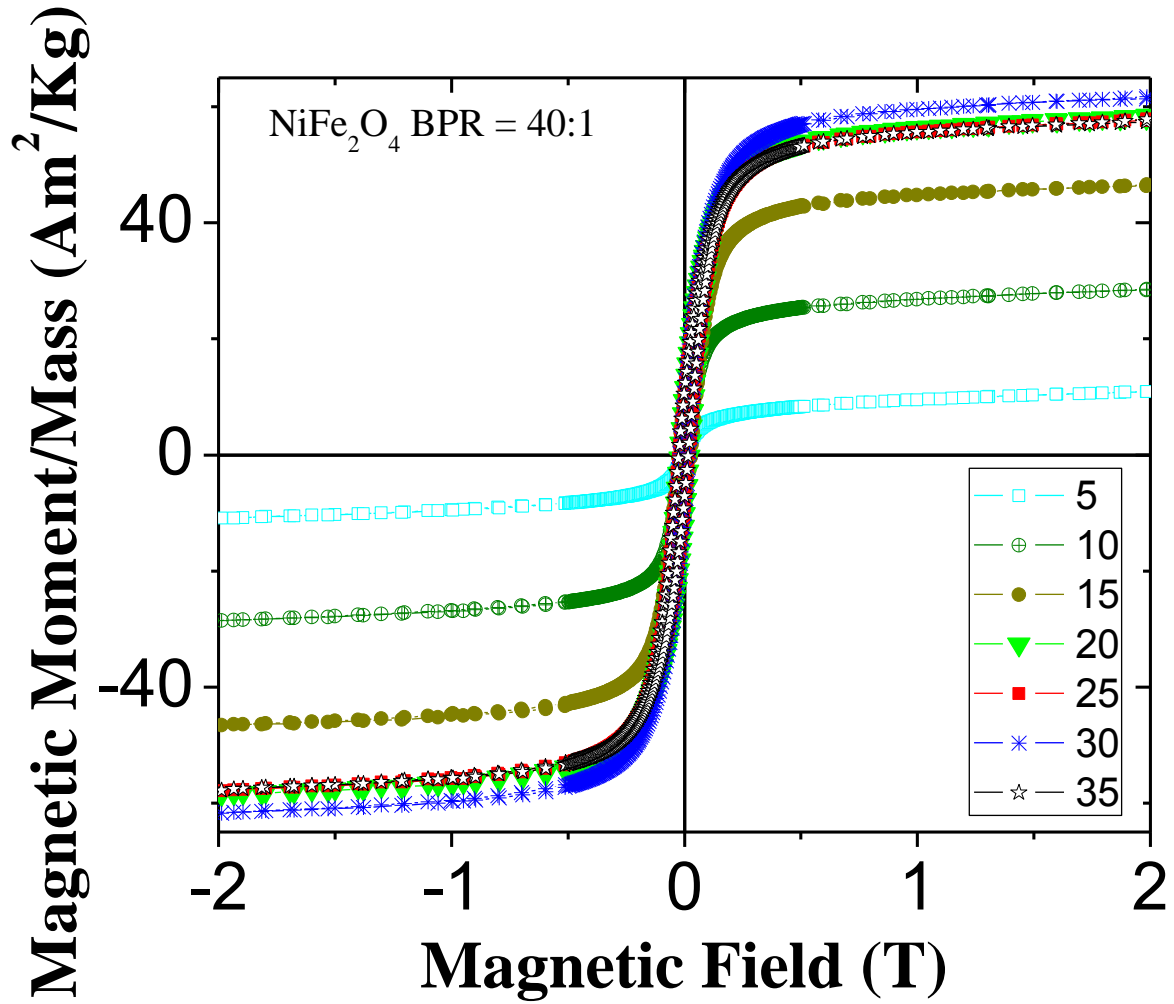


Figure 6.1 3. VSM measurements showing evolution of magnetic properties of reacting mixtures for BPR = 40:1 as a function of milling time.

In order to observe the detailed behavior of the sample material in relation to the VSM measurement, a plot of the specific magnetization and coercivity of the materials as a function of ball milling time was carried out. The relevant values are shown in Table 5.1.2, while the graphical plots are shown in Figure 6.1.4. From Figure 6.1.4, it shows a gradual increase in saturation magnetization as the milling time increases, reaching a value of 58.6 Am^2/Kg for 20

hours of milling, which then decreases to 25 hours of milling and increases again to reach its maximum value of 61.9 Am²/Kg for 30 hours of milling.

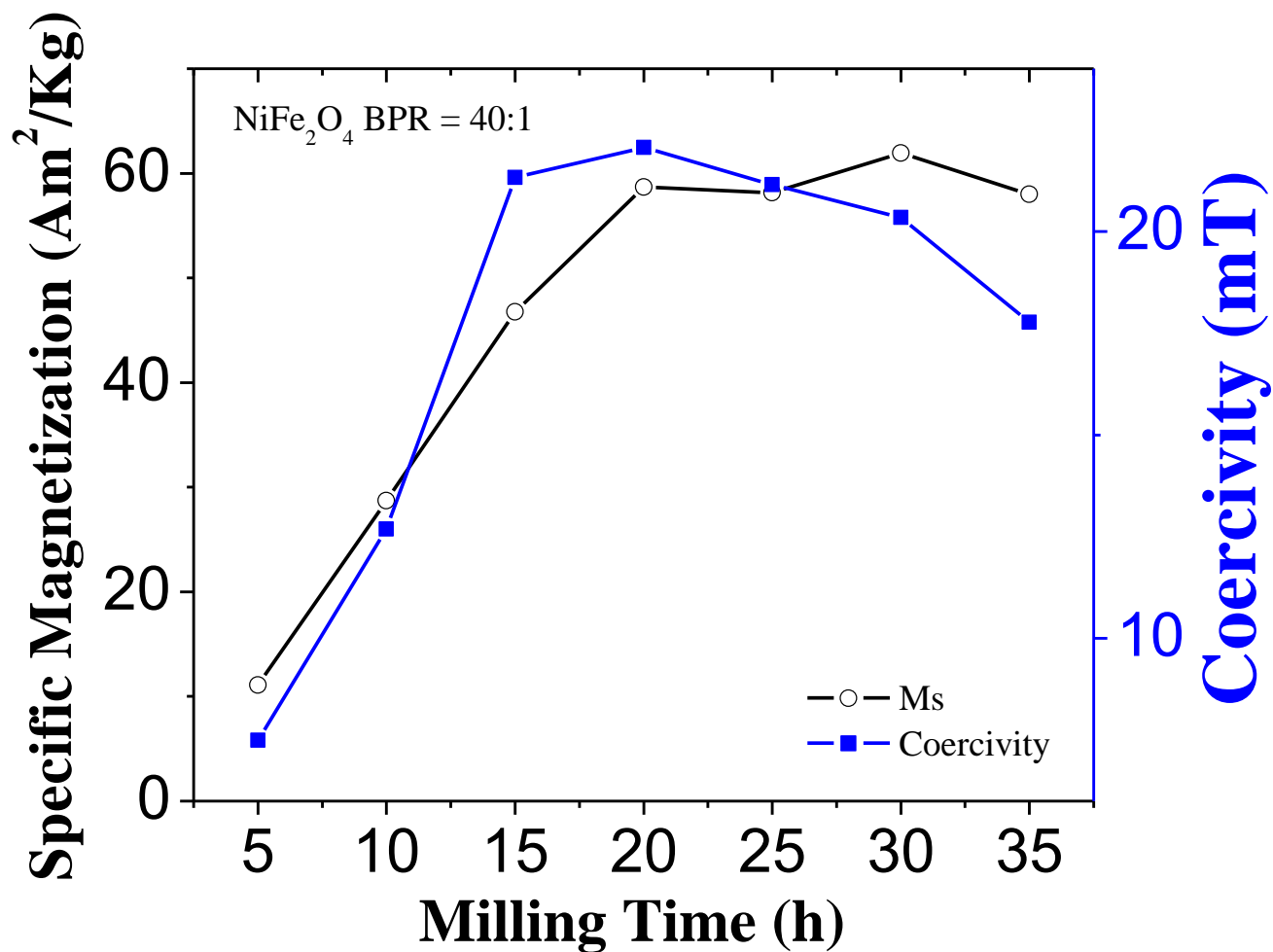


Figure 6.1 4 Evolution of coercivity and saturation magnetization as a function of ball milling of NiFe₂O₄ for BPR 40:1

Milling Time (h)	Saturation specific Magnetization- M_s (Am^2/Kg)	Coercivity- H_{ci} (mT)
5	11.088	7.50
10	28.724	12.6
15	46.744	21.3
20	58.687	22.06
25	58.148	21.15
30	61.944	20.34
35	57.994	17.77

Table 5.1.2. Saturation specific magnetization and coercivity of NiFe_2O_4 in different milling time.

6.2.2. Measurements of Mossbauer for BPR = 40:1

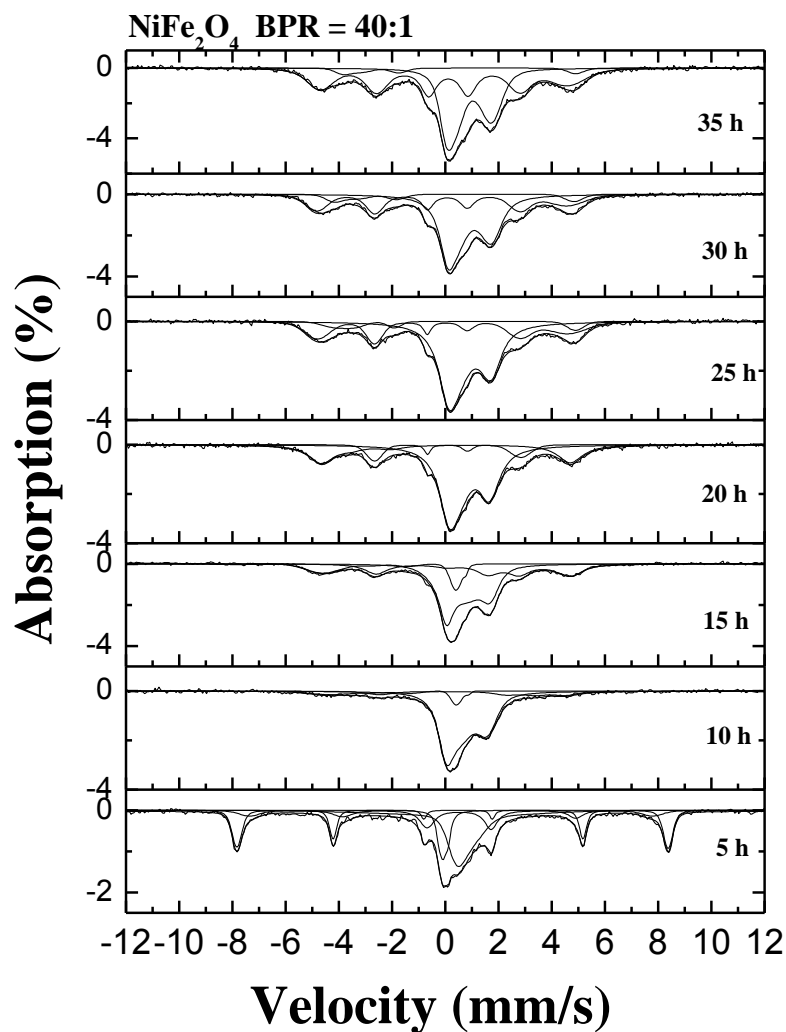


Figure 6.1.5. Mössbauer spectra of NiFe_2O_4 for BPR 40:1

As shown in Figure 6.1.5, there is a variation in the intensities of the characteristic peaks of the spectra of Mössbauer as milling time increases. Primaries in 5 hours, there is a change in the central peaks corresponding to a change in displacement isometric characteristic change in the positions of the ions in the network. This change is evidenced in X-ray spectra, showing the disappearance of peaks corresponding to peaks of the reagents and starting the formation of a

NiFe₂O₄ phase is completed at 10 hours of reaching to other grinding a superparamagnetic phase in the sample. To continue the grinding time, again arise the peaks related to the magnetic ordering in the sample. However, this behavior due to agglomeration of the particles forming the sample.

Authors	Synthesis Method	Particle size	Superparamagnetic Phase
A. Poddar [39]	Sol-gel	7 nm	OK
Jingying Wang [38]	Solvothermal	12 nm	NA
E. Manova [41]	Ball millig	8.1 nm	OK
Kamellia Nejati [42]	Hydrothermal	10-15 nm	OK
Z. Karcioğlu [43]	Hydrothermal	30 nm	NA
Bulat R. Churagulov [45]	Hydrothermal	10-14 nm 14-19 nm 13-18 nm	OK

Table 6.1.3. Comparison of crystallite sizes obtained for NiFe₂O₄ for different synthesis methods.

7. $\text{Ni}_x\text{Zn}_{(1-x)}\text{Fe}_2\text{O}_4$ $x = 0.5$ with BPR = 10:1

7.1 X-ray diffraction for BPR = 10:1

The diffractograms shown in figure 7.1.1, are a manual mixture of NiO (ICCD PDF # 98-000-0133), ZnO (ICCD PDF # 98-000-0483) and $\alpha\text{-Fe}_2\text{O}_3$ (ICCD PDF # 98-000-0240), together with the evolution with the ball mill (BPR = 10:1). Figure 7.1.1, shows the prominent peaks in the $2\theta = 31\text{-}32.5^\circ$; $46\text{-}47.5^\circ$, and $55\text{-}57.5^\circ$ experienced dramatic disappearance in contrast to the $\alpha\text{-Fe}_2\text{O}_3$ and NiO for the first 5 hours of milling. This indicates that the phase of ZnO is more prone to failure by distortion compared with the of the $\alpha\text{-Fe}_2\text{O}_3$ and NiO phases, which means that there is an increased contact area between particles of ZnO and $\alpha\text{-Fe}_2\text{O}_3$ due to reduction in particle size, allowing fresh surfaces repeatedly coming into contact, leading the formation of spinel phase ZnFe_2O_4 [27, 28, 29]. Given that ZnFe_2O_4 in a normal spinel as opposed to the inverted case for NiFe_2O_4 , it can be deduced that the single phase $\text{Ni}_{0.5}\text{Zn}_{0.5}\text{Fe}_2\text{O}_4$ formed by the formation of disordered followed by the intercalation of Ni^{2+} in the matrix leading to the eventual formation of $\text{Ni}_{0.5}\text{Zn}_{0.5}\text{Fe}_2\text{O}_4$. The peaks of NiO centered around $2\theta = 35^\circ$ and $2\theta = 62\text{-}65^\circ$ range could still be seen at 10 hours of milling, furthermore, the peaks of $\alpha\text{-Fe}_2\text{O}_3$ centered around $2\theta = 33^\circ$ and $2\theta = 49^\circ$. However, for this BPR (10:1) is not reached the Ni-Zn phase until 35 hours of milling, because the amount of reactive milling jars is high, causing the balls to not impact energy sufficient reagents powders [30, 31, 32, 33]. This does not favor the formation of the phase $\text{Ni}_{0.5}\text{Zn}_{0.5}\text{Fe}_2\text{O}_4$ for the 35 hours of milling, requiring a higher milling time on the sample to reach this stage, which is reached at 60 hours. These results are in agreement with Zimali et al [32], where the authors found a similar behavior $\text{Ni}_{0.5}\text{Zn}_{0.5}\text{Fe}_2\text{O}_4$ samples with BPR = 10:1, noting the initiation of single phase Ni-Zn to 48 hours of milling.

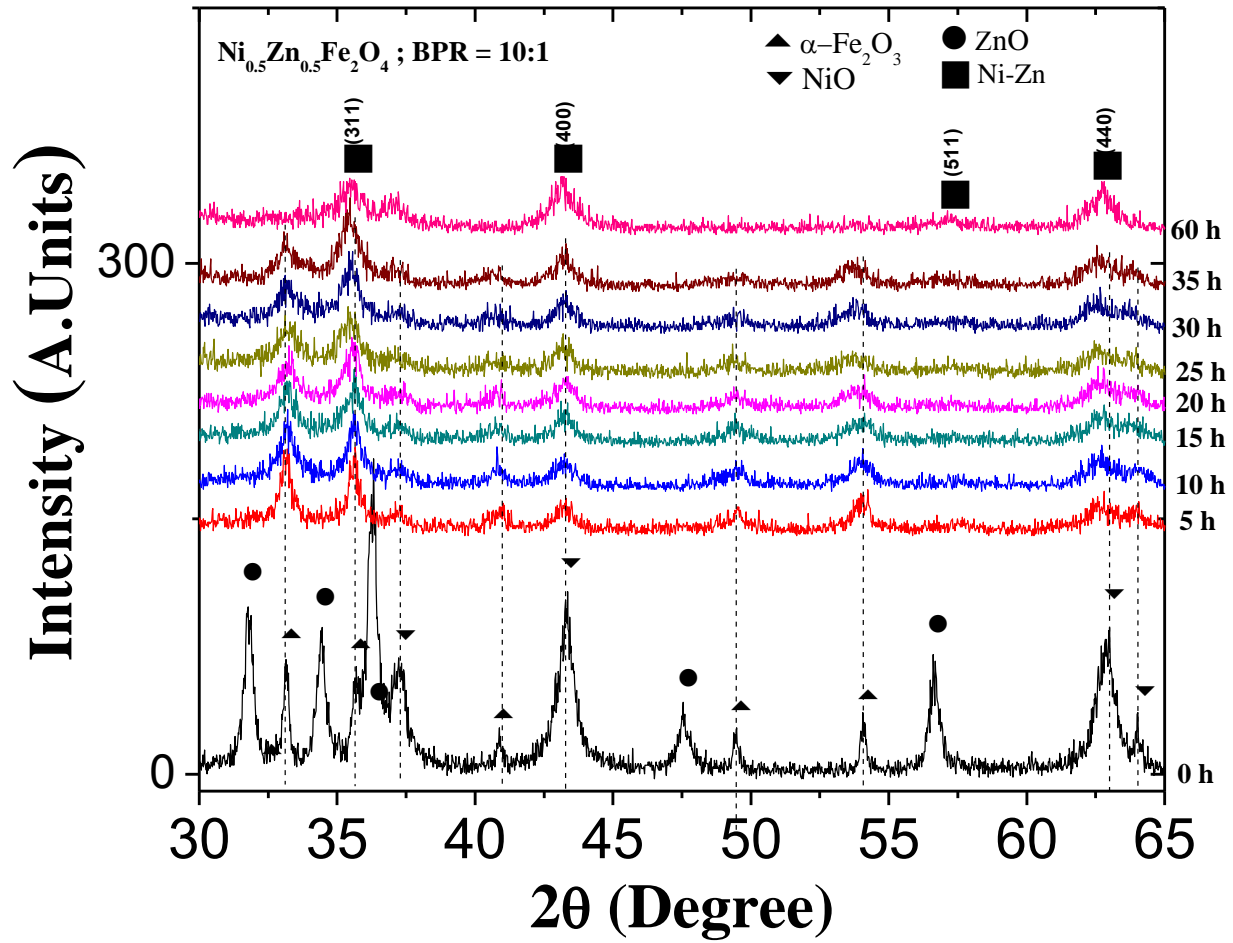


Figure 7.1 1. XRD spectra and $\text{Ni}_{0.5}\text{Zn}_{0.5}\text{Fe}_2\text{O}_4$ for BPR = 10:1

From careful study and analysis of spectral XRD peaks and relative intensities of NiO and $\alpha\text{-Fe}_2\text{O}_3$ in figure 7.1.2, the data shown in Table 7.1.1 were obtained. The spectral position that corresponding to the (110) reflection as a function of ball milling time showed that the peaks shifted to lower angles from $2\theta = 35.61^\circ$ to 35.43° , for the 5 hours and 35 hours state of milling for $\alpha\text{-Fe}_2\text{O}_3$, while for the NiO, the spectral position corresponding to the reflection (200) showed peaks shifted to lower angles $2\theta = 43.20$ to $2\theta = 43.19$, for 5 hours and 25 hours the

state of milling. The 30 hours and 35 hrs milled states displayed XRD peaks for the (200) reflection that exhibited reversion to higher angle positions corresponding to $2\Theta = 43.22^\circ$. This behavior is accompanied by a broadening of the peaks as determined from the full width at half maximum (FWHM) showed a progressive increase of 0.44 for 5 hours milled state to 0.94 for the milled state 35 hrs for $\alpha\text{-Fe}_2\text{O}_3$. Similarly, for NiO, where showed for 5 hours milling a FWHM of 0.72 and 0.98 for 35 hours of milling.

$\alpha\text{-Fe}_2\text{O}_3$					NiO				
Milling Time (h)	2 Theta	FWHM	Average Particle Size (nm)	Strain (10^{-3})	Milling Time (h)	2 Theta	FWHM	Average Particle Size (nm)	Strain (10^{-3})
0	-	-	60	0	0	-	-	20	0
5	35.61	0.44	18.97	5.98	5	43.20	0.72	11.87	5.98
10	35.62	0.54	15.45	7.33	10	43.23	0.76	11.24	7.33
15	35.62	0.58	14.39	7.88	15	43.25	0.80	10.68	7.88
20	35.59	0.70	11.92	9.51	20	43.29	0.90	9.50	9.51
25	35.46	0.78	10.69	10.64	25	43.19	0.94	9.09	10.64
30	35.48	0.94	8.87	12.82	30	43.22	0.96	8.90	12.82
35	35.43	0.94	8.87	12.84	35	43.22	0.98	8.72	12.84

Table 7.1.1. Particle size and strain of $\text{Ni}_{0.5}\text{Zn}_{0.5}\text{Fe}_2\text{O}_4$ in the unmilled and different milled states

The peaks of the phases mentioned above (NiO and $\alpha\text{-Fe}_2\text{O}_3$) disappear at 60 hours of milling, reaching single phase Ni-Zn, due the high impact energy transferred to the powder mixtures led to the destabilization of the precursor materials. The energy of impact in general causes the fracturing of the powdered materials with minimal cold welding given that the powdered precursors all belong to the ceramic material class. The ionic/covalent bonding associated with these oxides implied that extensive plastic deformation could not result since these bonds do not promote generation of dislocation as in the case of metallic bonding. Therefore, the types of structural defects that characterize the HEBM process in this study should include formation of

new surfaces (via fractures), anti-site defects, breaking of bonds- especially in surfaces, grain size refinement due to local stress and heat intensities.

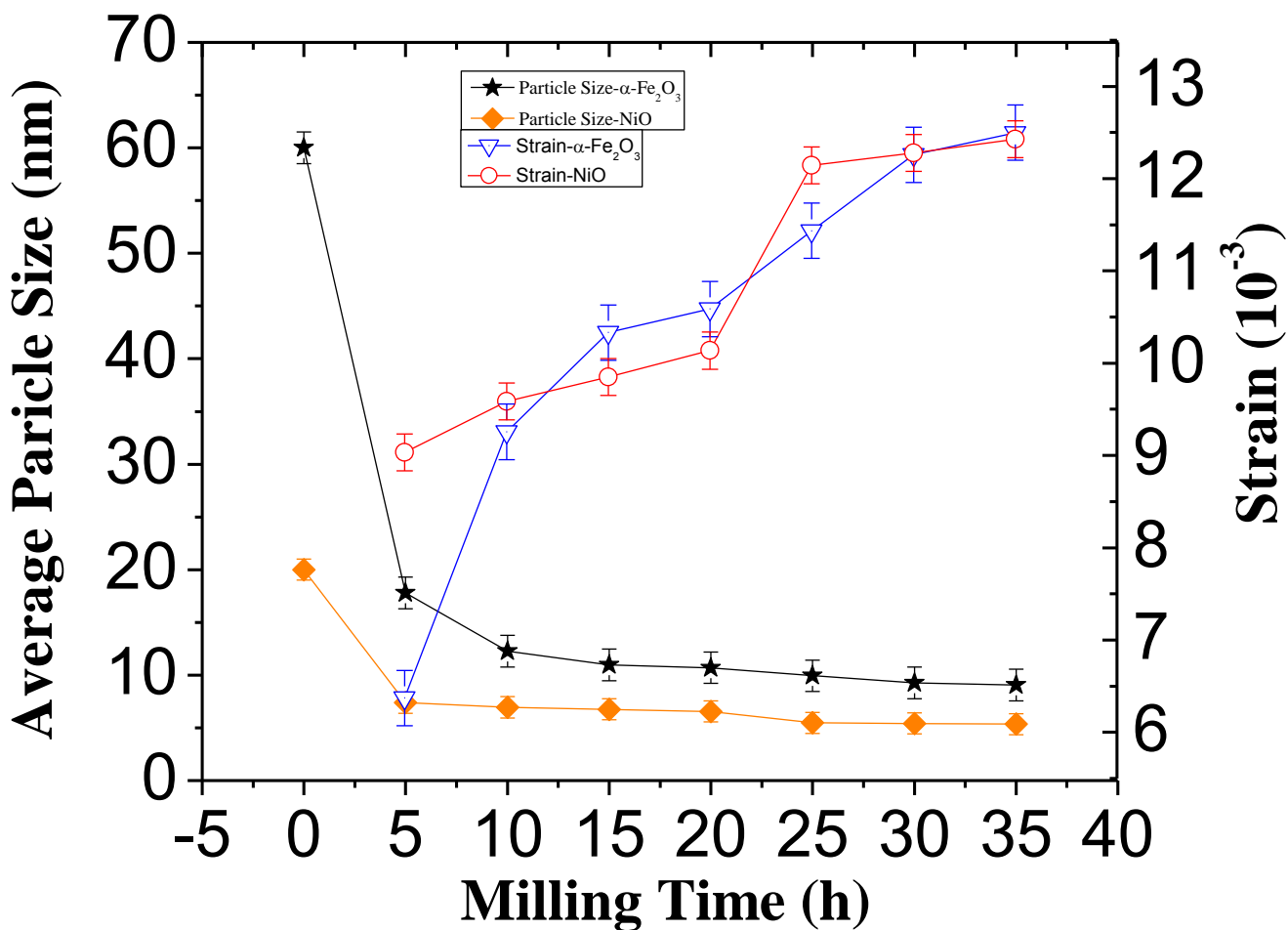


Figure 7.1 2. Evolution of particle size and strain of formed $\text{Ni}_{0.5}\text{Zn}_{0.5}\text{Fe}_2\text{O}_4$ (BPR = 10:1) as a function of ball milling time.

The particle-particle interaction leading to surface atomic diffusion there by new phase or metastable phase formation can be expected to occur during HEBM. Given that the relative thermodynamic stability of the precursor solids, ZnO, NiO and α -Fe₂O₃ vary, therefore, the order

of chemical reaction leading to the formation of the $\text{Ni}_{0.5}\text{Zn}_{0.5}\text{Fe}_2\text{O}_4$ would be determined by the decomposition of the precursor solid with the least stability. From XRD measurements, ZnO was observed to be the solid that was more affected during the early periods of ball milling. This could be as a result of high volatile nature of Zn, which implied that ZnO reacted more into the $\alpha\text{-Fe}_2\text{O}_3$ then NiO with the $\alpha\text{-Fe}_2\text{O}_3$. Given that the basic group structure of all the spinel ferrites is the same, the precise identification of the ZnFe_2O_4 , NiFe_2O_4 end member's ductile from the solid solution $\text{Ni}_{0.5}\text{Zn}_{0.5}\text{Fe}_2\text{O}_4$ was not attempted because of the resolution power of the XRD equipment and due to peaks overlaps of the ZnO and NiO phases. From the manual mixture XRD measurement, one was not in both to the peaks attribution, while, the effect of the ball milling process masked the precise monitoring of the phases with the peaks broadening, and disappearance all suggestive of the structural solution that accompanied the phases decomposition and chemical reactions with HEBM.

It is instructive to comment on the evolution of the average strain impacted on the materials with milling time. From measurements of X-ray diffraction, the average strain associated with the different precursors is observed a gradual increase of stress at 35 hours of grinding with reference to the first 5 hours of grinding. Analogously as seen in the NiO, at 35 hours with reference to the 5 hours of grinding. These behaviors are very similar to those obtained by Bid et al. [33, 34]. Along with the evolution of the average particle size, it is evident that the increase in tension by $\alpha\text{-Fe}_2\text{O}_3$ sample with respect to the sample of NiO, which reaches values of 12.84×10^{-3} and 4.55×10^{-3} respectively. Furthermore, the very minimum corresponding change in the particle size for milling times greater.

7.2 Measurements of Magnetization for BPR = 10:1

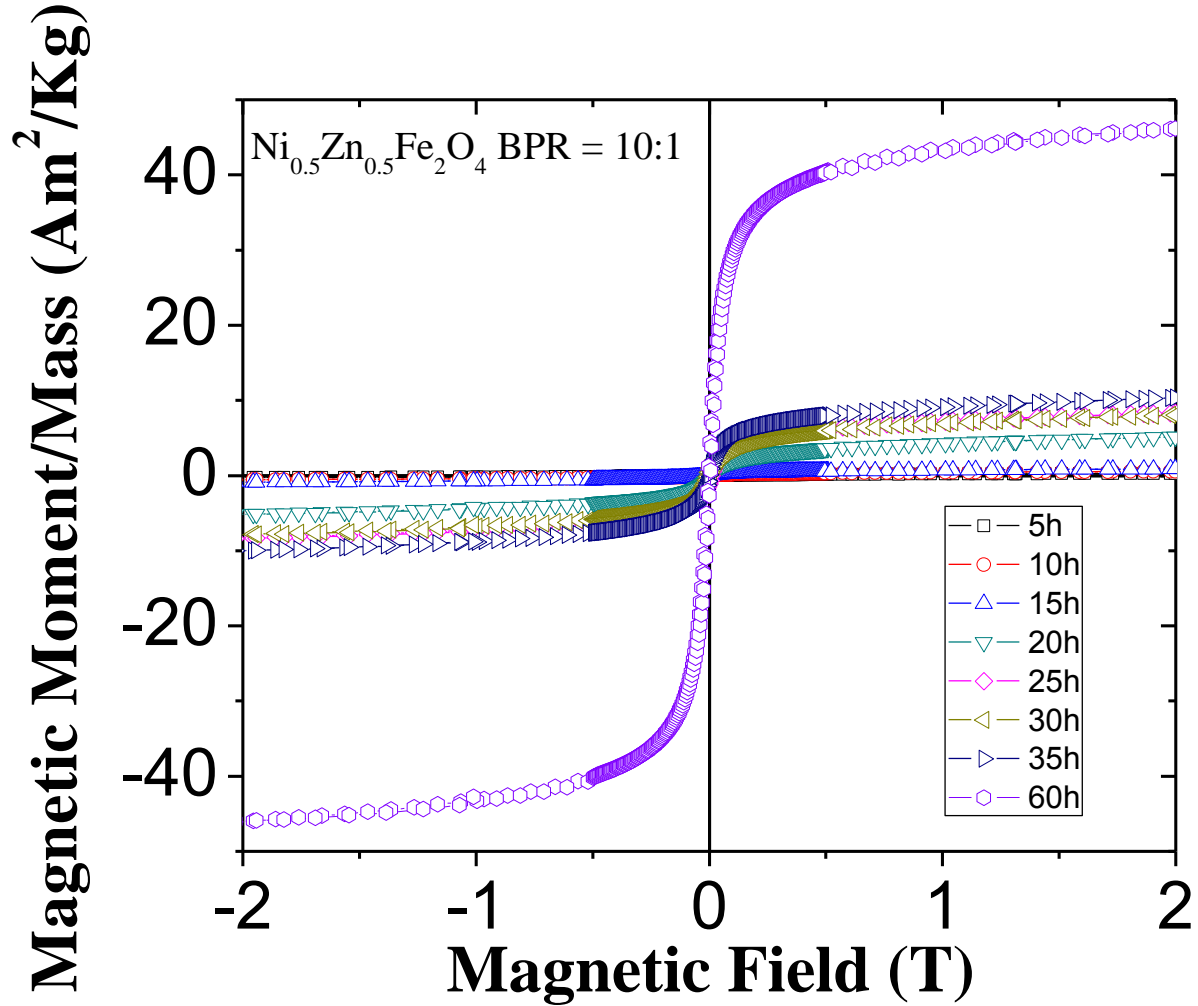


Figure 7.1 3.. VSM measurements corresponding of $\text{Ni}_{0.5}\text{Zn}_{0.5}\text{Fe}_2\text{O}_4$ for BPR = 10:1

The magnetic properties of Ni-Zn have been investigated by magnetization hysteresis curve measurements at room temperature. Figure 7.1.3 shows magnetization hysteresis curves measured at room temperature for the Ni-Zn samples milled for various times. The specific saturation magnetization values are progressively increasing as the milling time also makes,

observed a sudden, when the sample is ground to 60 hours. This behavior is in agreement with X-ray measurements shown in the figure 7.1.1, in which there is a progressive reduction in the particle size and an increase in strain, as milling time increases. It should be noted that with some possible techniques to extract information from each of the reagents. However, VSM measurements, it is possible to separately identify each one of the precursors, because this technique gives global information of all the materials involved in the reaction. Based on this observation, we can say that the progressive increase of the saturation magnetization is due to the reaction of the precursors progressively and ends in the formation of the single phase NiZn, as indicated by X-ray measurements, which are observed peaks corresponding to said phase at 60 hours of milling. For its part, the coercivity shows a gradual decrease from its maximum value to approximately zero with respect to the milling time, due to reduced particle size.

Milling Time (h)	Saturation specific Magnetization- M_s (Am ² /Kg)	Coercivity- H_{ci} (mT)
5	0.27	19.82
10	0.54	7.02
15	0.87	3.81
20	5.23	3.04
25	8.44	2.52
30	8.05	2.60
35	10.30	2.41
60	46.39	3.47

Table 7.1. 2. Saturation specific magnetization and coercivity of $Ni_{0.5}Zn_{0.5}Fe_2O_4$ in different milling time.

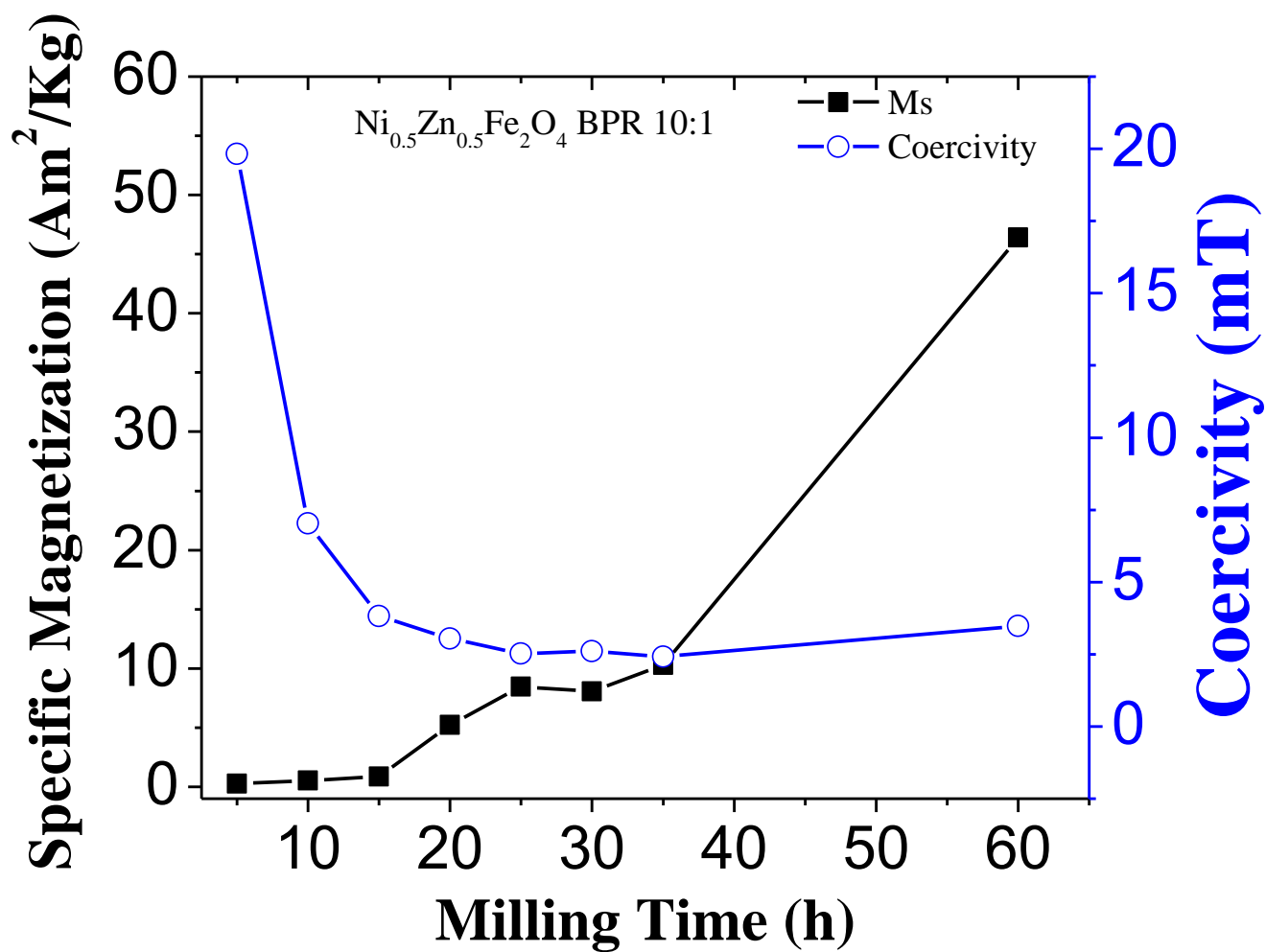


Figure 7.1 4. Evolution of coercivity and saturation magnetization as a function of ball milling of $\text{Ni}_{0.5}\text{Zn}_{0.5}\text{Fe}_2\text{O}_4$ for BPR 10:1.

7.3 Measurements of Mossbauer for BPR = 10:1

The room temperatures Mössbauer spectroscopic measurements carried out after 5 hours intervals of ball milled materials are shown in Fig. 7.1.3. The spectra helped to elucidate on the nature of the characteristics of the Fe sites in the materials, especially with respect to their magnetic order, and electronic configuration. The five hours ball milled state is comprised of prominent sextet's peaks with a central doublet. Where this double non-magnetic central has increased in intensity to higher milling times, contrary to the sextet's peaks which decrease their intensity and widen as the milling time increases to become asymmetrical. With these observations, one authority state that the mechanochemical synthesis process was achieved via the progressive consumption of the precursor materials as evidenced by the reduction in intensity of the sextet peaks and the simultaneous evolution of the central non magnetic peaks.

In fitting the Mössbauer spectra, the hyperfine distribution model according to Rancourt and Ping [37] was used. This meant that as much as possible the fitting was carried out in order to obtain the best fit based on the internal field distribution novel where correlation from one spectrum to another in succession was carefully singlet. Starting from the fitting of the manual mix unmilled material while translates to the fitting of the fitting of the as-supplied $\alpha\text{-Fe}_2\text{O}_3$ materials, the 5 hours and successively milled materials were carried out.

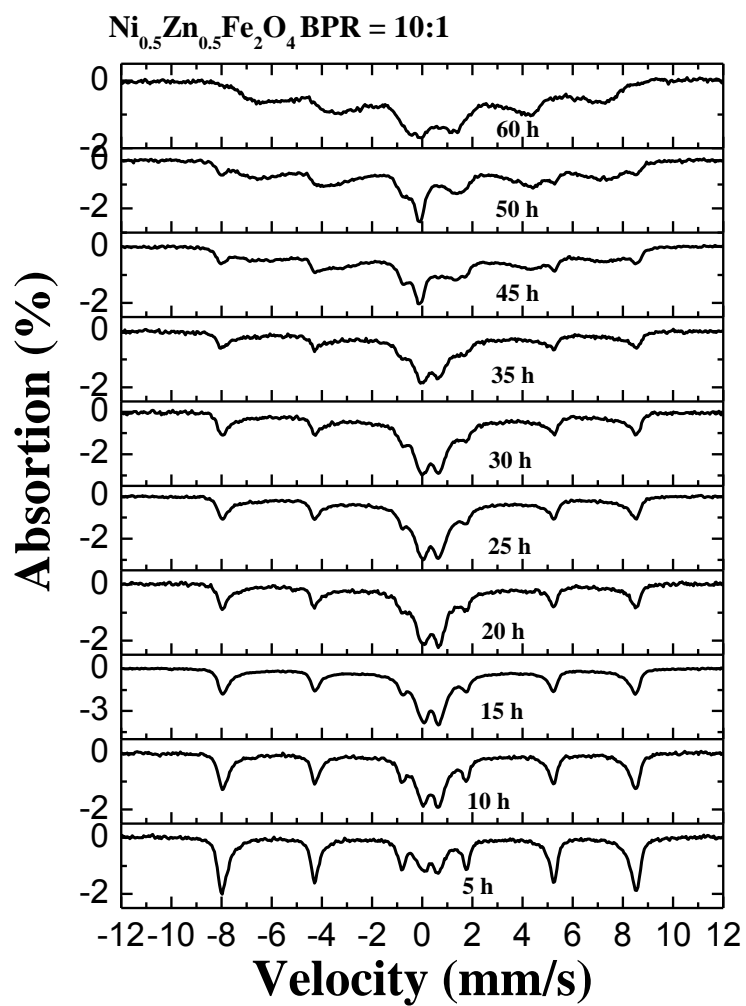
Starting from the fitting of the manual mix unmilled material while translates to the fitting of the fitting of the as-supplied $\alpha\text{-Fe}_2\text{O}_3$ materials, the 5 hours and successively milled materials were carried out. The 5 hrs milled materials was fitted by surrendering that the consumption of the reactants precursor was gradual and progressive. The 5 hrs milled state was reasonably fitted with 3-sites, corresponding to $\alpha\text{-Fe}_2\text{O}_3$ and or non-magnetic component at the central portion of the spectrum.

According to J Z Jiang et al [38, 39], the ball milling of CuFe_2O_4 using Fritch pulveriser planetary, mill, under set of condition different from ours, but with ball to powder ratio of 20:1, with a time interval systematic, resulted in the particle size from 41 nm to as low as 10 nm based on the Schereer analysis. While the majority of the material remained magnetic at room temperature, based on room temperature Mossbauer measurement, a relative area which account for about maximum of 21.9 % for a 4 hours grinding was reported to have isomer shift of 0.39 mm/s with quadrupole splitting of -0.14 mm/s. The internal magnetic field for the material was 50.4 T and decreased slightly to 46.7 T for 29 hrs grinding. The low hyperfine field and large linewidth of the magnetic subspectra due to the grinding which the authors attributed to achieved from large particle size distribution and also, significant degree of magnetic relaxation and/or magnetic disorder in milled samples. The observation of decrease of internal magnetic field is consistent with the study reported by Bid et al [40, 41, 42] during the ball milling of $\alpha\text{-Fe}_2\text{O}_3$ in which they used a BPR of 30:1 and 35:1, where the internal magnetic field was reduced from 51.82 T (518.2 kOe) to as value of 48.89 T (488.9 kOe).

The most prominent sextet peaks fitted with an internal magnetic field of 510.53 kOe. The isomer shift value of -0.725 mm/s with reference to $\alpha\text{-Fe}$, and relative ratios of the outer-must and inert must peaks (h_1/h_3) ratio of the 3.64 and the inner-must peaks ratio (h_2/h_3) of the 2.2 was indication of existence of some structural charges that occurred with the grinding of the material mixture. The internal magnetic field value is well with the range of reported value for $\alpha\text{-Fe}_2\text{O}_3$ in bulk for in the literature [43, 44, 45] in which for nanoparticles measuring 16 nm, two components of sextet peaks of 52.5 T and 48 T were reported. In our case, the values determined as shown in Table 1 are 51.0 T and 48.6 T, respectively. In direct comparison to the above reference [46, 47, 48], then 48 T components accounted for about 10 % of their spectrum, and

has more broadened peaks than the main prominent peak with 52.5 T field. Given that the smaller field of 485.98 kOe component accounted for about 35.03 % of the 5 hours milled state, we can suggest that the difference arose from the HEBM action, where by structural change caused the overall change in the abundance ratios of these components. Unlike their suggestion that this component could be due to a ferrite of state or amorphous phase [49, 50], we are not able to comment further on this component because, our α -Fe₂O₃ precursor material was not prepared in house in contrast to the case of these workers.

In this work, the component of the spectrum for the 35 hours milled state which account for after 9.09 % of the material was fitted with an internal magnetic field of 509.65 kOe. If showed be noted here, that the isomer shift corresponding to this site was 0.192 mm/s while the quadrupole splitting of -0.125 mm/s and line broadening based on peaks full width at high maximum (FWHM) was 0.154 mm/s indicated that structural formation or transition occurred at this stage. Given that the reference α -Fe calibration internal magnetic field is 330 kOe, therefore, one could speculate that these sites correspond to Fe sites associated with a lot of disorder such that reduction of Fe³⁺ to Fe occurred a certain degree. The totality of this observation points to progressive evolution of the materials with ball milling, while the superparamagnetic state is not quite reached for the 60 hours milled state. It could be suggested that the milled materials reached a stage where further milling could display the mechanochemical synthesis to any direction, i.e, a sort of transition dead state.



Figures 7.1 5. Mössbauer spectra of $\text{Ni}_{0.5}\text{Zn}_{0.5}\text{Fe}_2\text{O}_4$ for BPR = 10:1

8 $\text{Ni}_x\text{Zn}_{(1-x)}\text{Fe}_2\text{O}_4$ $x = 0.5$ with BPR = 20:1

8.1 X-ray diffraction for BPR = 20:1

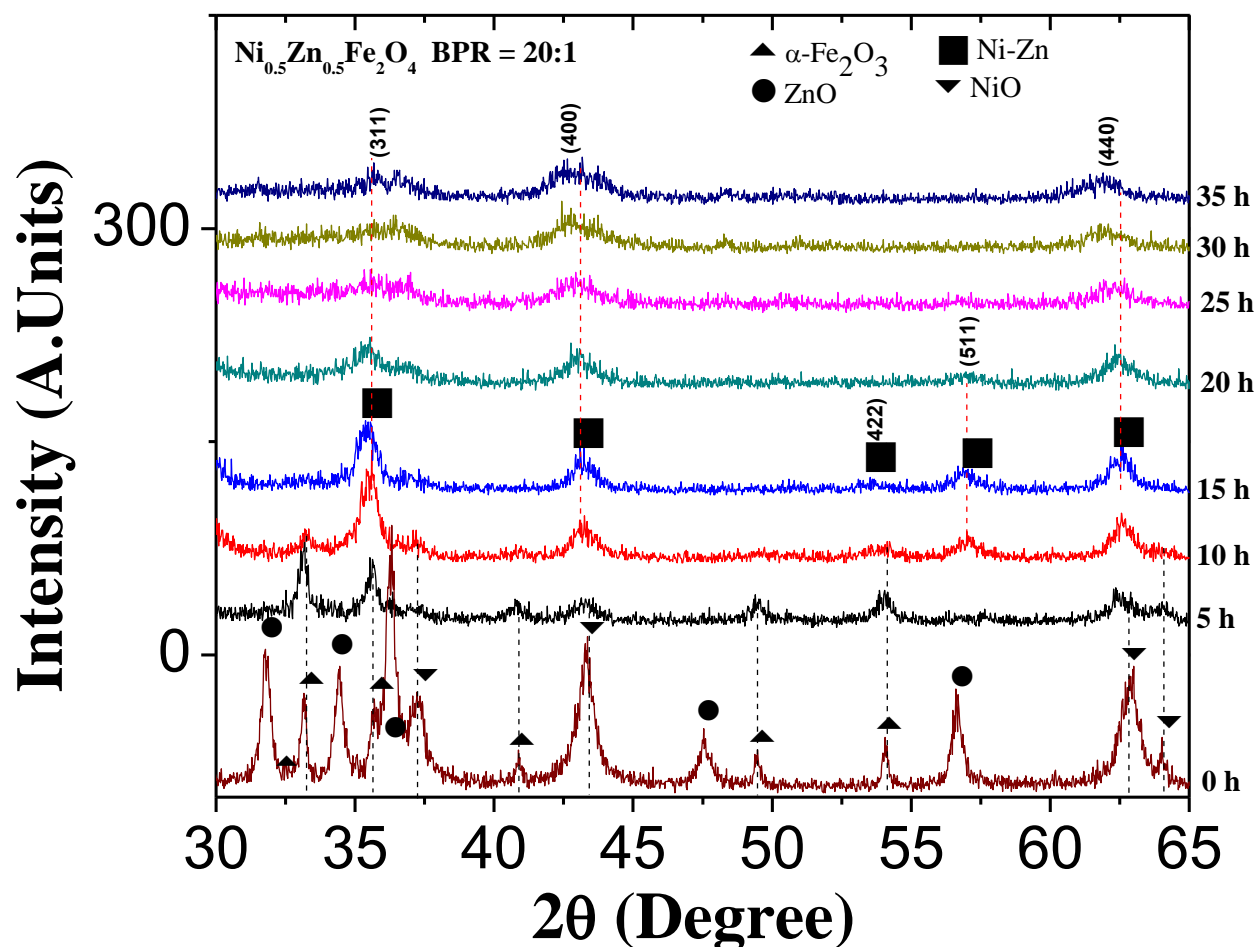


Figure 8.1 1. XRD spectra and $\text{Ni}_{0.5}\text{Zn}_{0.5}\text{Fe}_2\text{O}_4$ for BPR = 20:1

The mechanochemical synthesis reaction as started under the experimental was carefully monitored by using powder XRD measurements to determine extent of reactions as a function of time starting with the manual mixture. The spectral peaks for the NiO, ZnO, and $\alpha\text{-Fe}_2\text{O}_3$ phases

were matched with corresponding JSPDF files reference as NiO (ICCD PDF#98-000-0133), for ZnO (ICCD PDF#98-000-0483) and α -Fe₂O₃ (ICCD PDF#98-000-0240).

Close examination of the XRD patterns show in Figure 8.1.1, shows that the reaction leading to the formation of the single phase Ni_{0.5}Zn_{0.5}Fe₂O₄ commenced within 5 hours of ball milling and continued progressively subsequently. In comparison of the ZnO phase, the prominent peaks in the $2\theta = 31-32.5^\circ$; $46-47.5^\circ$, and $55-57.5^\circ$ experienced dramatic disappearance in contrast to the α -Fe₂O₃ and NiO phases peaks. This is suggestive of higher rate of decomposition of ZnO leading the formation of spinel phase. The peaks of NiO centered around $2\theta = 35^\circ$ and $2\theta = 62-65^\circ$ range could still be seen at 10 hours of milling unlike the case of ZnO peaks. Given that ZnFe₂O₄ in a normal spinel as opposed to the inverted case for NiFe₂O₄, it can be deduced that the single phase Ni_{0.5}Zn_{0.5}Fe₂O₄ formed by the formation of disordered followed by the intercalation of Ni²⁺ in the matrix leading to the eventual formation of Ni_{0.5}Zn_{0.5}Fe₂O₄. After 15 hr of grinding the broadened peaks and $2\theta = 35-36^\circ$ and $2\theta = 42-45^\circ$ showed that a lot of structural disorder accompanied the ball milling process.

The structural disorder leading to the formation of single phase Ni_{0.5}Zn_{0.5}Fe₂O₄ was accompanied by the rapid particle size reduction of the precursor solids due to the high impacts energy transferred to the particles during the grinding. With the particle size reduction, the eventual inter-mixing leading to the formation of the single phase occurred. The further, broadening and loss of peaks intensities from 15 hrs to 35 hours, demonstrated that loss of crystallinity of the new phase, culminated in the formation of highly metastable material. It was not possible to extrapolate or deduce further the state of the material given that only three broad peaks could be discerned beyond 20 hours of ball milling.

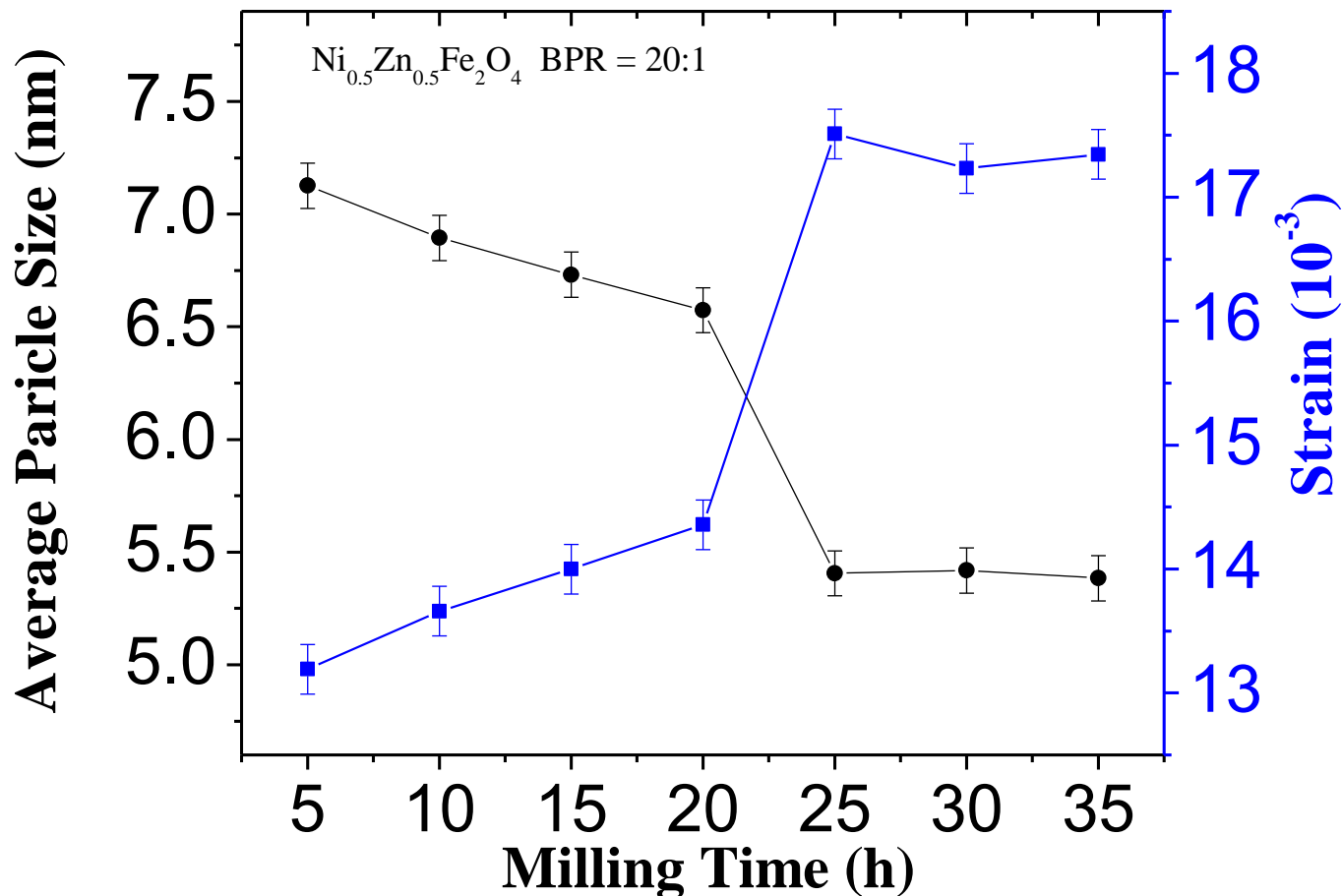


Figure 8.1 2. Particle size reduction and strain of $\text{Ni}_{0.5}\text{Zn}_{0.5}\text{Fe}_2\text{O}_4$ for BPR = 20: 1 as a function of time ball milling

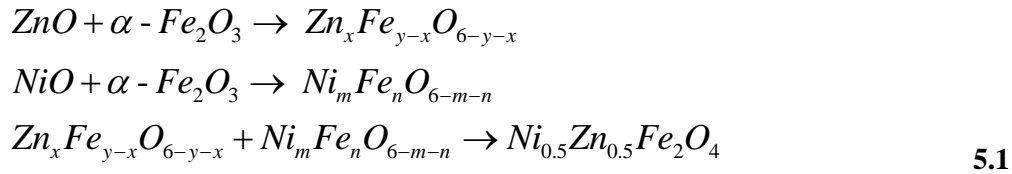
From careful examination and analyses of XRD spectral peaks and relative intensities, single phase $\text{Ni}_{0.5}\text{Zn}_{0.5}\text{Fe}_2\text{O}_4$ identified as NiZn in Figure 8.1.2, the data displayed in Table 8.1.1 were obtained. The spectral position that corresponding to the (400) reflection as a function of ball milling time showed that the peaks shifted to lower angles from $2\theta = 43.31^\circ$ to 43.00° , for the 5 hours and 25 hours state of milling. The 30 hours and 35 hrs milled states displayed XRD peaks for the (400) reflection that exhibited reversion to higher angle positions corresponding to $2\theta =$

43.62° and 43.61 respectively. While the spectral position to lower angles and reverted to higher angle shifting, the broadening of the peaks as determined from the full width at half maximum (FWHM) showed a progressive increase from 1.026 for the 5 hrs milled state, to 1.5907 for the 35 hrs milled state.

Given the extensive broadening of the spectral peaks from the 5 hrs milled state and the 35 hrs milled state showed that the HEBM process employed in this study was indeed effective in engendering the mechanochemical synthesis process. The high impact energy transferred to the powder mixtures led to the destabilization of the precursor materials. The energy of impact in general causes the fracturing of the powdered materials with minimal cold welding given that the powdered precursors all belong to the ceramic material class. The ionic/covalent bonding associated with these oxides implied that extensive plastic deformation could not result since these bonds do not promote generation of dislocation as in the case of metallic bonding. Therefore, the types of structural defects that characterize the HEBM process in this study should include formation of new surfaces (via fractures), anti-site defects, breaking of bonds- especially in surfaces, grain size refinement due to local stress and heat intensities.

The particle-particle interaction leading to surface atomic diffusion thereby new phase or metastable phase formation can be expected to occur during HEBM. Given that the relative thermodynamic stability of the precursor solids, ZnO, NiO and α -Fe₂O₃ vary, therefore, the order of chemical reaction leading to the formation of the Ni_{0.5}Zn_{0.5}Fe₂O₄ would be determined by the decomposition of the precursor solid with the least stability. From XRD measurements, ZnO was observed to be the solid that was more affected during the early periods of ball milling. This could be as a result of high volatile nature of Zn, which implied that ZnO reacted more into the α -Fe₂O₃. Given that the basic group structure of all the spinel ferrites is the same, the precise

identification of the ZnFe_2O_4 , NiFe_2O_4 end member's ductile from the solid solution $\text{Ni}_{0.5}\text{Zn}_{0.5}\text{Fe}_2\text{O}_4$ was not attempted because of the resolution power of the XRD equipment and due to peaks overlaps of the ZnO and NiO phases. From the manual mixture XRD measurement, one was not in the peaks attribution, while, the effect of the ball milling process masked the precise monitoring of the phases with the peaks broadening, and disappearance all suggestive of the structural solution that accompanied the phases decomposition and chemical reactions with HEBM. It is possible that the sequence of reaction leading to the formation of the single phase solid solution could be summarized thus:



Where the phases are related via the spinel structure. The structural re-adjustment required to from the spinel structure from ZnO and NiO should be favored by the incorporation (i.e. diffusion) of Ni^{2+} and Zn^{2+} ions in the $\alpha\text{-Fe}_2\text{O}_3$ matrix then the contrary case of Fe^{3+} from $\alpha\text{-Fe}_2\text{O}_3$ into the NiO and ZnO matrices.

The addition of acetone as a processing agent promoter helped to ensure intimate mixing of the powder precursor materials such that the inter-diffusion accompanying the particle size reduction in enhanced. The use of XRD measurement as was carried out could not be used to explore the intricate sequential steps associated with the mechano-chemical synthesis process alone, hence the integration of other measuring technique as Mössbauer spectroscopy and vibrating sample magnetometer types.

It is instructive to comment on the evolution of the average strain impacted on the materials with the progressives of the mechanochemical synthesis. From the XRD measurements, the average strain associated the formation of single solid solution phase, $\text{Ni}_{0.5}\text{Zn}_{0.5}\text{Fe}_2\text{O}_4$ showed progressive increase up to 20 hours of milling followed by a dramatic increase at 25 hours of grinding with reference to the 5 hours milled state, on jump in comparison to the 20 hours milled state. Together with the evolution of the average particle size, it is evident that decrease of average strain in the first regime up to 20 hrs of milling time, while the terminal stage corresponding to the 25 hours, 30 hours and 35 hours milled stage exhibited change in average strain and corresponding very minimal change in particle size.

Milling Time (h)	2 Theta	FWHM	Avarage Particle Size (nm)	Strain (10^{-3})
5	43.31	1.2006	7.126111	13.19
10	43.23	1.2406	6.894462	13.65
15	43.20	1.2706	6.731026	13.99
20	43.13	1.3007	6.573626	14.35
25	43.00	1.5808	5.406302	17.51
30	43.62	1.5807	5.418404	17.23
35	43.61	1.5907	5.38419	17.345

Table 8.1.1. Particle size and strain of $\text{Ni}_{0.5}\text{Zn}_{0.5}\text{Fe}_2\text{O}_4$ in the unmilled and different milled states

The general or overall evolution trend between the particle size and the average strain can be reconciled based on two competing factors, namely the need for the formation of the equilibrium solids solution single phase and the refinement of the particles of the realized phase. Given that for the material systems involved in the mechanochemical synthesis, limitation of diffusion substances for the cations causes local structural rearrangement leading to the formation of overall metastable single phase solid solution imbued with significant structural defects as evidenced by the reflections of the diffracting phase from the XRD measurements. Given the

peaks broadening, and peaks disappearance, it is possible that limited amorphous phase corresponding to the same average composition of $\text{Ni}_{0.5}\text{Zn}_{0.5}\text{Fe}_2\text{O}_4$ accompanied the highly defective crystalline state of the same solid solution phase.

8.2 Measurements of Magnetization for BPR = 20:1

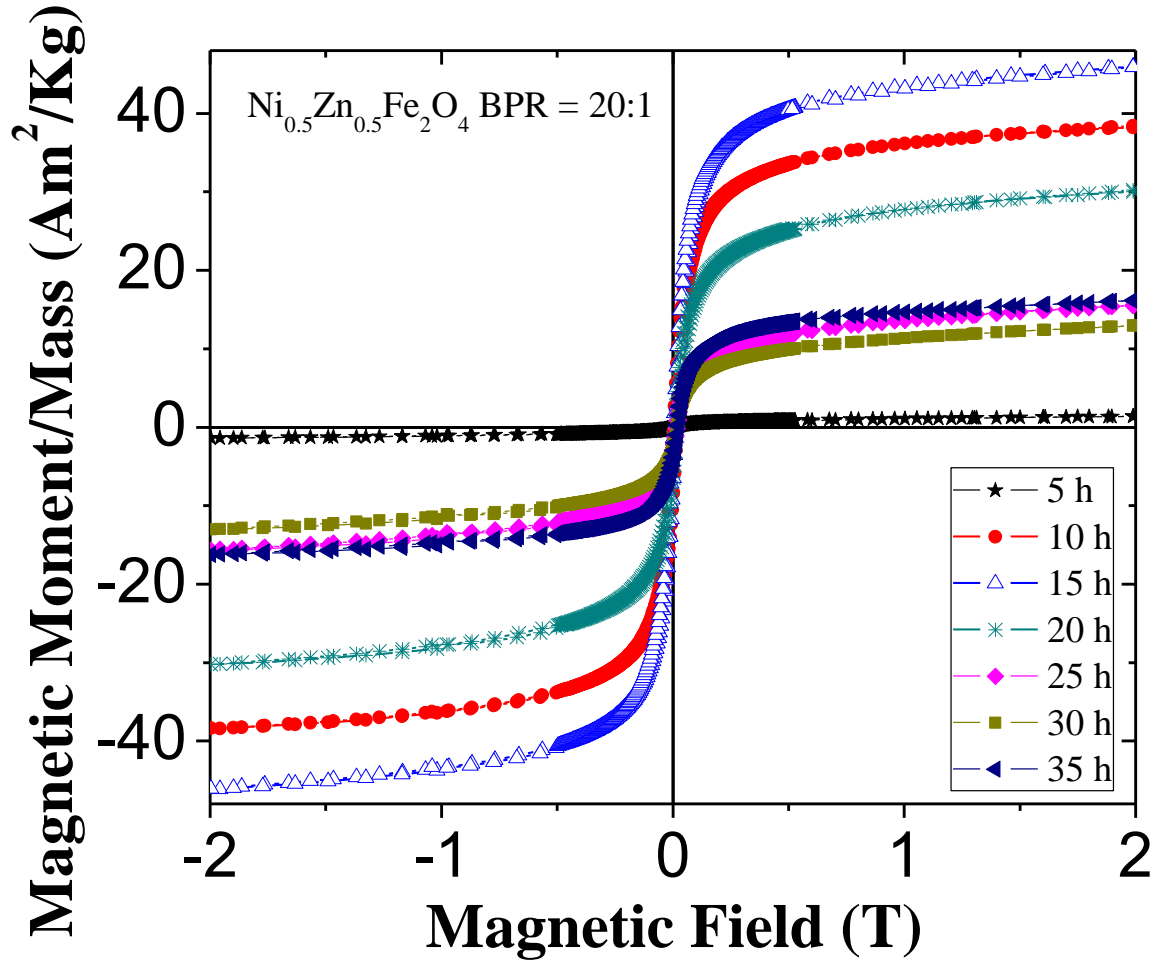


Figure 8.13. VSM measurements corresponding of $\text{Ni}_{0.5}\text{Zn}_{0.5}\text{Fe}_2\text{O}_4$ for BPR 40:1

The vibrating sample magnetometer measurement showing the variation of the saturation specific magnetization (M_s) as a function of applied magnetic field show in figure 8.1.3, where the overall magnetization behavior of the milled materials are shown. Examination of the plots shows that the behaviors of the milled materials corresponding to the 5 hr, 10 hr, and 15 hrs milled state, displayed decreasing saturation magnetization. The tendency displayed for these three plots is in sharp contrast to the plots obtained for the 20 hrs, 25 hrs and 30 hrs milled states. Overall, these two groups of the milled materials are substantially consistent with the XRD measurements analysis displayed in figure 8.1.1, in which drastic change in particle size and average strain associated with the materials are observed. While it was possible to extract contributions arising from the individual precursor materials as a function of milling time, the same could not be understood for the VSM measurements. This is majority due to the fact that the entire material contribution is registered in the hysteresis loop. This said the overall pattern change in the hysteresis profile can be used to reduce or reconcile the progressive mechanochemical reactions leading to decreasing precursor materials with increasing single phase solid solution consisting of $\text{Ni}_{0.5}\text{Zn}_{0.5}\text{Fe}_2\text{O}_4$. Further, the third drastic change in the hysteresis loop profile corresponded to the 35 hours milled state which showed an almost flat profile, i.e., within magnetization. This is clear indication that the 35 hrs milled state consisted of no-magnetic particles which can be attributed to the phenomenon of superparamagnetic entirely. Based on this observation, it can be stated that the decreasing saturation magnetization was caused by the progressive formation particles associated with the $\text{Ni}_{0.5}\text{Zn}_{0.5}\text{Fe}_2\text{O}_4$ while the coercivity observed in the 5-15 hrs milled states are due to the magnetic phases whose states are due to the magnetic phases whose particle sizes were not small enough to yield superparamagnetic behavior. These could be due to trace amounts of $\alpha\text{-Fe}_2\text{O}_3$, NiO, and

relativity large $\text{Ni}_{0.5}\text{Zn}_{0.5}\text{Fe}_2\text{O}_4$ metastable phases. The overall profile of the magnetization plots as show in figure 3 is therefore very instructive of the milled states of the materials.

The fact that HEBM causes them formation of metastable phases which are substantially reduced in size (despite the existence of particles agglomeration, and inter-particle interaction, etc) the contribution due to the overall magnetic behavior and the VSM plots show in figure 8.1.3. Thus, preferential distribution of Ni^{2+} cations in the octahedral sites with Zn^{2+} in the tetrahedral sites can be used to reconcile the tendencies and overall behavior observed. Firstly, terminating surfaces of the spinel phases are expected to be the low value (h, k, l) phase such as (110) and (111) hyper and as a result, the coercivity determination for the milled materials can be explained. Had the materials been in equilibrium states, without inter-particle interactions, the contributions of the surface cationic distribution would be less, and zero-coercivity sigmoid shaped hysteresis loop associated with superparamagnetic phenomenon would holds way.

Milling Time (h)	Saturation specific Magnetization- M_s (Am^2/Kg)	Coercivity- H_{ci} (mT)
5	1.43	6.88
10	38.58	2.88
15	46.36	3.75
20	30.40	4.77
25	15.80	4.00
30	13.15	4.14
35	16.34	5.59

Table 8.1.2. Saturation specific magnetization and coercivity of $\text{Ni}_{0.5}\text{Zn}_{0.5}\text{Fe}_2\text{O}_4$ in different milling time.

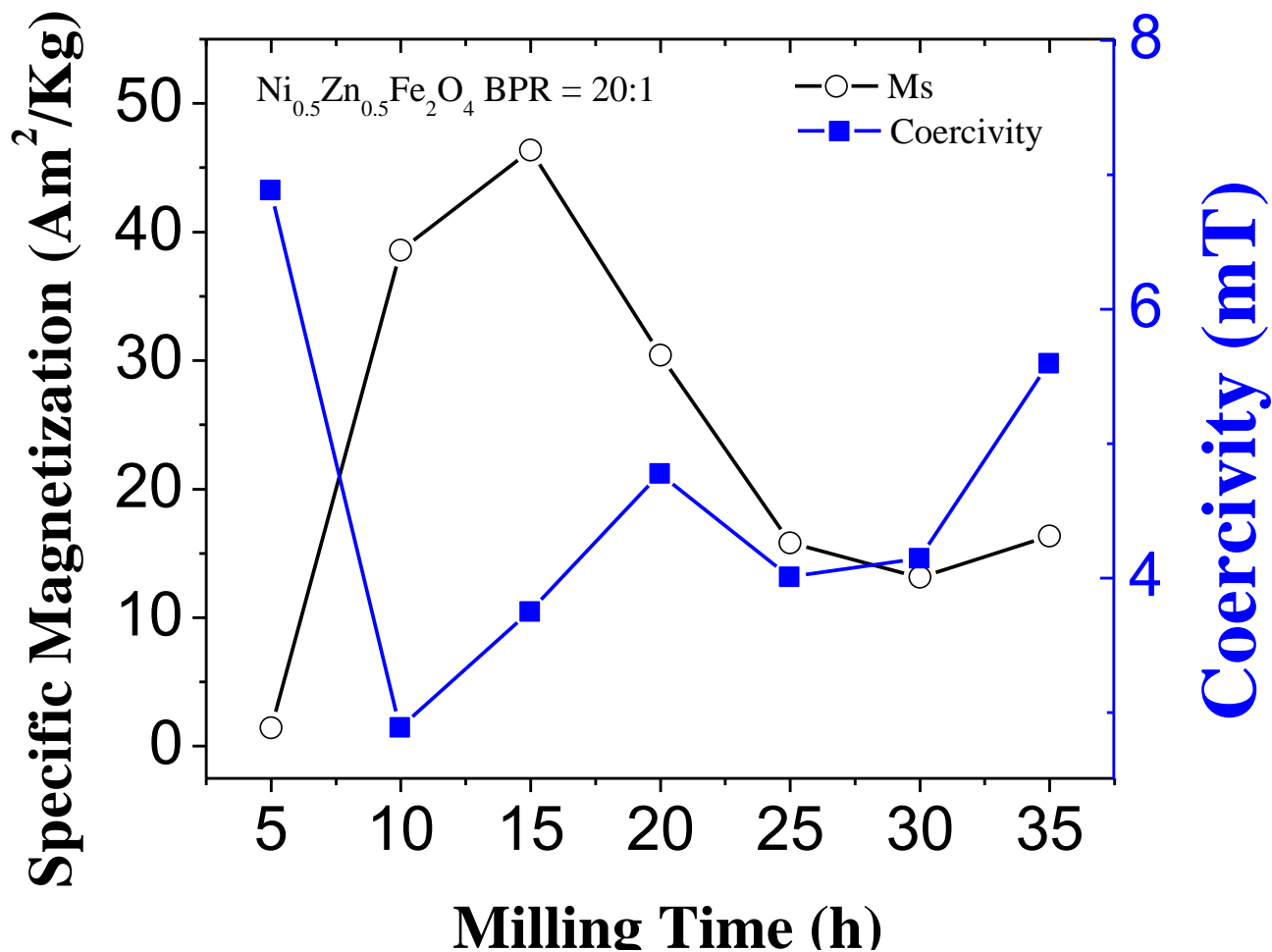


Figure 8.1.4. Evolution of coercivity and saturation magnetization as a function of ball milling of $\text{Ni}_{0.5}\text{Zn}_{0.5}\text{Fe}_2\text{O}_4$ for BPR 20:1

8.3 Measurements of Mossbauer for BPR = 20:1

Room temperature measurements of the ball milled materials mixtures were carried out after 5 hours intervals to corroborate the XRD, and VSM corresponding measurement. These are displayed in figure 8.1.5, with their respective subspectra following the fitting exercises. The five hours ball milled state is comprised of prominent sextet's peaks with a central doublet. In comparison to the 10 hours milled, material spectrum, the sharp sextet peaks similarly observed

for the 5 hrs milled state in seen too have diminished in intensity while row very broad sextet peaks emerged. Further the central doublet peaks observed in the 5 hrs milled state can be seen to have adopted or more any metrical shape, in addition to some broadening. With continued milling the sharp sextet peaks were evolution of the central non-material peaks develop into free non-material peaks with a feat background observed for the 35 hrs milled state. With these observations. One authority state that the mechanochemical synthesis process was achieved via the progressive consumption of the precursor materials as evidenced by the reduction in intensity of the sextet peaks and the simultaneous evolution of the central non magnetic peaks.

In fitting the spectra, care was taken to use as much non-restrictions, of the parameters as possible. This meant that as much as possible the fitting was carried out in order to obtain the best fit based on the internal field distribution nobel where correlation from one spectrum to another in succession was carefully singlet. Starting from the fitting of the manual mix unmilled material (whiles translates to the fitting of the fitting of the as-supplied $\alpha\text{-Fe}_2\text{O}_3$ materials, the 5 hours and successively milled materials were carried out. The 5 hrs milled materials was fitted by surridering that the censureption of the reactants precursor was gradual and progressive. The 5 hrs milled state was reasonably fitted with 3- sites, corresponding to $\alpha\text{-Fe}_2\text{O}_3$ and or non-magnetic component at the central portion of the spectrum.

The most prominent sextet peaks fitted with an internal magnetic field of 511.12 kOe and accounted for 11.50 % of the total spectrum. The isomer shift value of 0.094 mm/s with reference to a-Fe, and relative rations of the outer-must and inert must peaks (h_1/h_3) ratio of the 4.6 and the inner-must peaks ratio (h_2/h_3) of the 2.7 was indication of existence of some structural charges that occurred with the grinding of the material mixture. The internal magnetic field value is well with the range of reported value for $\alpha\text{-Fe}_2\text{O}_3$ in bulk for in the literature [49,

50, 51] in which for nanoparticles measuring 16 nm, two components of sextet peaks of 52.5 T and 48 T were reported. In our case, the values determined as shown in Table 1 are 51.1 T and 48.5 T, respectively. In direct comparison to the above reference [49, 50], then 48 T component accounted for about 10 % of their spectrum, and has more broadened peaks than the main prominent peak with 52.5 T field. Given that the smaller field of 484.51 kOe component accounted for about 35.03 % of the 5 hours milled state, we can suggest that the difference arose from the HEBM action, where by structural change caused the overall change in the abundance ratios of these components. Unlike their suggestion that this component could be due to a ferrihydrite or amorphous phase [51, 52, 53, 54], we are not able to comment further on this component because, our α -Fe₂O₃ precursor material was not prepared in house in contrast to the case of these workers.

Hematite has a rhombohedral crystal structure and is isostructural with Al₂O₃ (corundum). For well crystallized and chemically pure α -Fe₂O₃, the Morin transition temperature, T_M occurs near 264 K, while the Neel temperature occurs at about 956 K, and in a weakly Ferromagnetic (WFM) which arises from the a slight misalignment of the antiferromagnetic lattices in the basal phase of the structure. The material can equally display antiferromagnetic state (AFM) below T_M temperature. It has been reported that with the internal magnetic field and T_M can be affected by a variety of often inter dependent factors such as particle-size, morphology, presence of impurities, state of crystallinity, etc. [38, 39]. The Mossbauer parameters for nanostructured α -Fe₂O₃ obtained from sol-gel technique followed by heat treatment revealed that the particle size increased with increased annealing temperature according to Kim et al [48, 49].

In addition to the increase of the particle size with heat treatment, the interval field value was observed to be dependent of on particle size with the 350 °C treated samples exhibiting an

internal field of 511.299 kOe, with isomer shift equal to 0.381 mm/s and quadrupole splitting of -0.101 mm/s, and had no paramagnetic doublet in contrast to samples heat treated at lower temperature (100 °C, 140 °C, 180 °C, and 220 °C) where particles sizes from XRD measurement were 4.02 nm, 8.58 nm, 12.48 nm, 13.02 nm, respectively with the size for the 350 °C treatment reported as 17.37 nm. The range of internal magnetic field value was 447.848 to 508.241 kOe between the 4.02 nm and the 13.02 nm sized samples.

Further, according to Bid et al [25, 37, 38], the ball milling of pre-cast α -Fe₂O₃ using Fritch pulveriser planetary, mill, under set of condition different from ours, but with ball – to powder ratio of 30:1 and 35:1 resulted in the particle size from 57.05 nm to as low as 10.39 nm (BPR=35:1) after 15 hours of grinding or to (BPR =30:1) an average size of 9.41nm after 20 hrs of grinding, based on the Debye Scherrer analysis. While the majority of the material remained magnetic at room temperature, based on room temperature Mossbauer measurement, a doublet which account for about maximum of 25.78 % for a 20 hours grinding was reported to have isomer shift in the range of 0.38 -0.64 mm/s with quadrupole splitting ranging for 1.69-2.33 mm/s. The internal magnetic field for the unground material was 518.2 kOe and decreased slightly to 498.67 kOe for 20 hrs grinding. The sextet peaks became unsymmetrical and very broadened due to the grinding which the authors attributed to arising from large particle size distribution and also, to the fluctuation of the magnetization vector in a direction close to the easy direction resulting to the so-called collective magnetic excitations. From the displayed, the spectra showed that α -Fe₂O₃ persisted until 15 hours of ball milling field since the corresponding site having internal magnetic field of 511.12 kOe at 5 hours HEBM decreased slightly to 510.83 kOe after 15 hours of ball milling. The observation of decrease of internal magnetic field is consistent with the reported by Bid et al [26, 33, 34] during the ball milling of α -Fe₂O₃ in which

they used a BPR of 30:1 and 35:1, where the internal magnetic field was reduced from 51.82 T (518.2 kOe) to as value of 48.89 T (488.9 kOe).

The component of the spectrum for the 20 hours milled state which account for after 7.3 % of the material was fitted with an internal magnetic field of 536.11 kOe. It should be noted here, that the isomer shift corresponding to this site was 1.206 mm/s while the quadrupole splitting of -0.236 mm/s and line broadening based on peaks full width at half maximum (FWHM) was 0.230 mm/s indicated that structural formation or transition occurred at this stage. This stage characteristically distinguished the 10 hours and 15 hrs milled state from the 25 hr, 30 hr, and 35 hr milled state that were fitted with 3Fe sites respectively. While the Mossbauer parameters for the 25 hours and 30 hours milled materials as shown in the Table are comparable, however, the terminal 35 hours milled materials is distinctively or substantively different from them. The internal magnetic field values of the magnetically 2-Fe sites fitted in the 35 hours milled material were 296.79 kOe and 300.80 kOe respectively while their quadrupole splitting values -1.016 mm/s and -1.018 mm/s indicating that the close similarity of the local distribution associated with them. Their isomer shift values were markedly different being 1.158 mm/s and 0.0495 mm/s with their respective abundances of 21.91 % and 9.28 % respectively. Given that the reference α -Fe calibration internal magnetic field is 330 kOe, therefore, one could speculate that these sites correspond to Fe sites associated with a lot of disorder such that reduction of Fe^{3+} to Fe occurred to a certain degree. The totality of this observation points to progressive evolution of the materials with ball milling, while the superparamagnetic site which accounted for 45.38 % in the 30 hours milled state. It could be suggested that the milled materials reached a stage where further milling could display the mechanochemical synthesis to any direction, i.e., a sort of transition state.

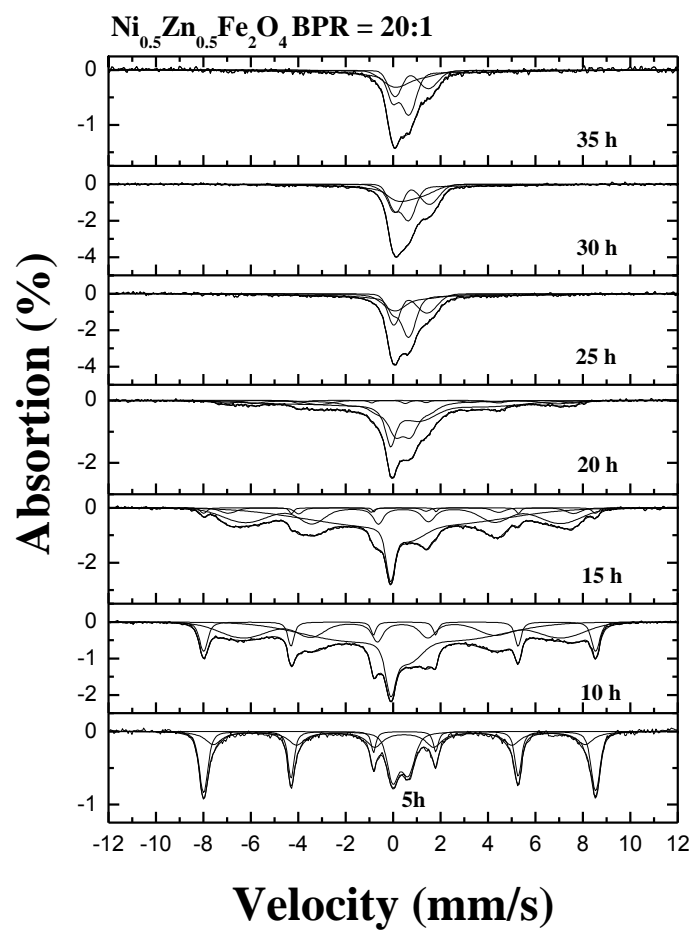


Figure 8.1 5: Mössbauer spectra of $\text{Ni}_{0.5}\text{Zn}_{0.5}\text{Fe}_2\text{O}_4$ for BPR 20:1 and different milling time

9 $\text{Ni}_x\text{Zn}_{(1-x)}\text{Fe}_2\text{O}_4$ $x = 0.5$ with BPR = 40:1

9.1 X-ray diffraction for BPR = 40:1

The X-ray diffraction pattern of the starting powder is indexed for single-phase NiZn spinel. Figure 9.1.1 shows XRD data for samples milled from 5 to 35 hours together with those for the raw sample. Unlike the two previous synthesis (BPR = 10:1 and 20:1) to 5 hours of milling, the formation of the single phase $\text{Ni}_{0.5}\text{Zn}_{0.5}\text{Fe}_2\text{O}_4$ has been noticed clearly due to the appearance of the four peaks corresponding to (220), (311), (400) and (422), reflections at $2\theta = 30.51^\circ$, 35.75° , 43.11° and 48.29° respectively, as reported [28, 30]. Compared with other synthesis (BPR = 10:1 and 20:1) phases NiO, ZnO and $\alpha\text{-Fe}_2\text{O}_3$, experience rapid disappearance dramatically. This suggests greater BPR leads to rapid formation as spinel phase. As the milling time increases, there is a progressive broadening and reduced intensity peaks characteristic of Ni-Zn phase until 35 hours of milling. This broadening of peaks is related to a variation in particle size, structural defects, high amount of effort and possible occurrence of a superparamagnetic phase.

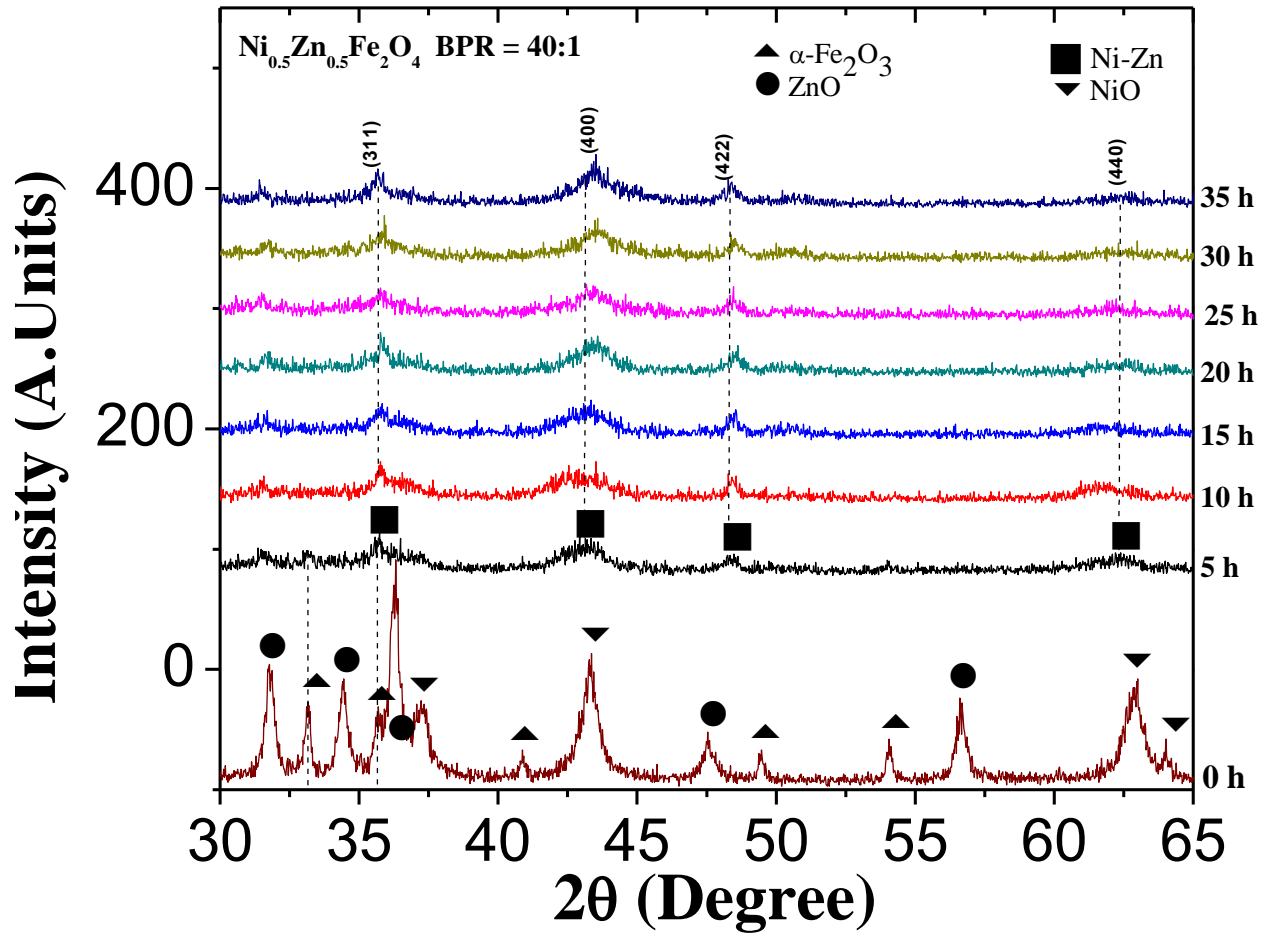


Figure 9.1 1. XRD spectra of $\text{Ni}_{0.5}\text{Zn}_{0.5}\text{Fe}_2\text{O}_4$ for BPR = 40:1.

To check whether there is a relationship between the peak broadening the grain size reduction and strain, we made a measure of the average grain size and strain as a function of milling time. From the XRD measurements, the average strain associated the formation of single solid solution phase, $\text{Ni}_{0.5}\text{Zn}_{0.5}\text{Fe}_2\text{O}_4$ showed progressive increase up to 35 hours of milling. Together with the evolution of the average particle size, it is evident that increase of average strain in the first regime up to 15 hrs of milling time, while the terminal stage corresponding to the 20 hours, 30

hours and 35 hours milled stage exhibited minimal change in average strain and corresponding very minimal change in particle size.

Milling Time (h)	2 Theta	FWHM	Avarage Particle Size (nm)	Strain (10^{-3})
5	43.25	1.26	6.78	13.87
10	43.366	1.38	6.20	15.15
15	43.291	1.58	5.42	17.38
20	43.502	1.48	5.78	16.19
25	43.345	1.50	5.70	16.48
30	43.554	1.52	5.64	16.61
35	43.46	1.56	5.48	17.08

Table 9.1.1. Particle size and strain of $\text{Ni}_{0.5}\text{Zn}_{0.5}\text{Fe}_2\text{O}_4$ in the unmilled and different milled states.

Given the extensive broadening of the spectral peaks from the 5 hrs milled state and the 35 hrs milled state showed that the HEBM process employed in this study was indeed effective in engendering the mechanochemical synthesis process. The high impact energy transferred to the powder mixtures led to the destabilization of the precursor materials. The energy of impact in general causes the fracturing of the powdered materials with minimal cold welding given that the powdered precursors all belong to the ceramic material class. The ionic/covalent bonding associated with these oxides implied that extensive plastic deformation could not result since these bonds do not promote generation of dislocation as in the case of metallic bonding. Therefore, the types of structural defects that characterize the HEBM process in this study should include formation of new surfaces (via fractures), anti-site defects, breaking of bonds- especially in surfaces, grain size refinement due to local stress and heat intensities.

The general or overall evolution trend between the particle size and the average strain can be reconciled based on two competing factors, namely the need for the formation of the equilibrium

solids solution single phase and the refinement of the particles of the realized phase. Given that for the material systems involved in the mechanochemical synthesis, limitation of diffusion substances for the cations causes local structural rearrangement leading to the formation of overall metastable single phase solid solution imbued with significant structural defects as evidenced by the reflections of the diffracting phase from the XRD measurements

To verify if there is a relationship between the peak broadening and the grain size reduction was carried out a measure of the average grain size as a function of milling time. As shown, the figure 5.2, with increasing milling time there is a reduction in grain size from the first 10 hours of grinding, where the grain size is reduced from about 70 nm to 60 nm. This reduction in grain size due to repeated collision between balls and powders with very high impact velocity deform and work-hardens the powder. In this repetitive cold welding fracturing mechanism, cold welding of overlapping particles occurs between the surfaces formed by previous fractures. The competing process of deformation, fracture and welding during milling produces a microstructural refinement [50, 51]. It is hoped that this behavior affects the magnetic properties of the sample. For this reason measurements were performed magnetic properties.

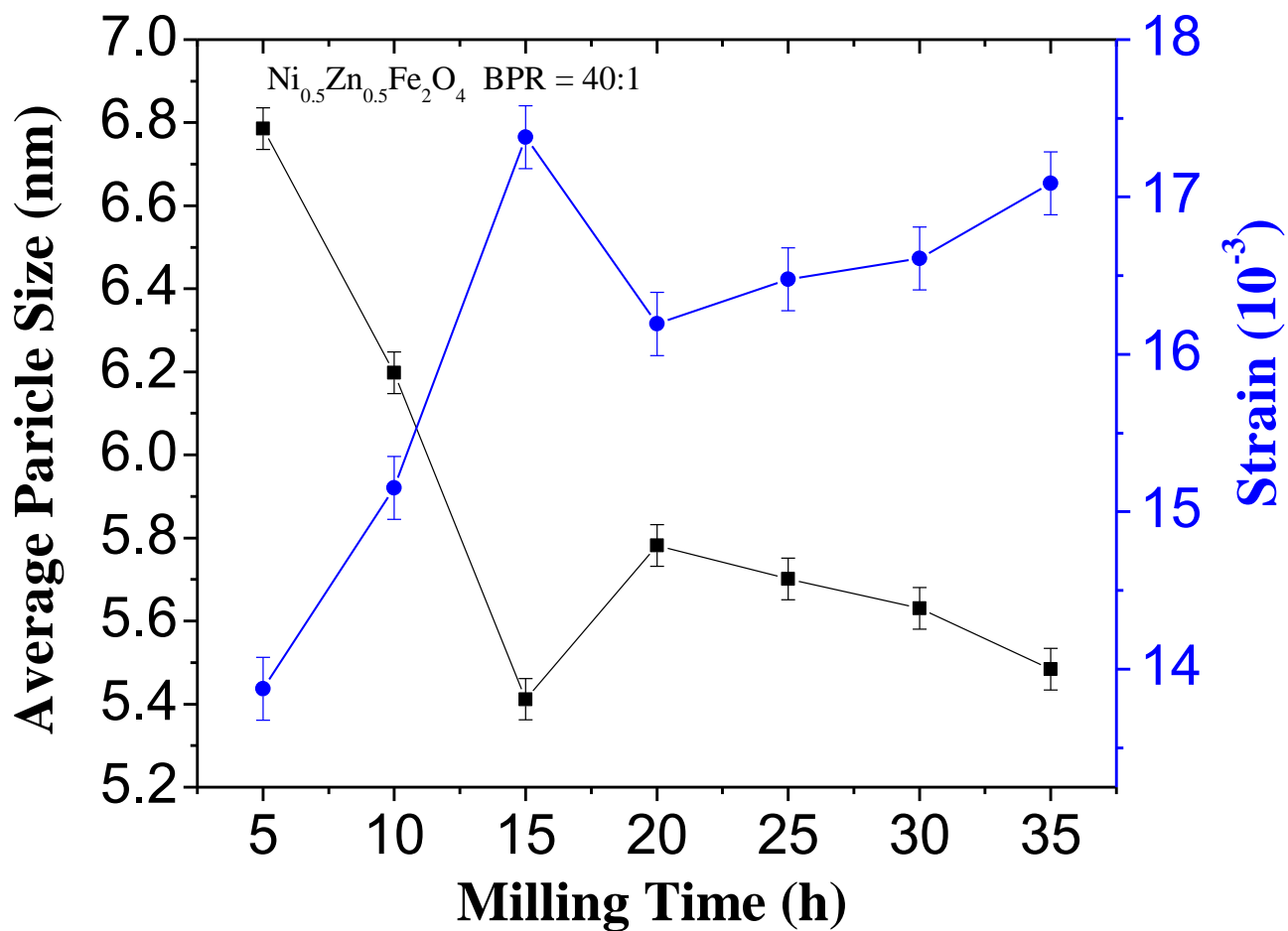


Figure 9.1 2. Average particle size reduction and strain of $\text{Ni}_{0.5}\text{Zn}_{0.5}\text{Fe}_2\text{O}_4$ for BPR 40:1 as a function of milling time

9.2 Magnetization measurement for BPR = 40:1

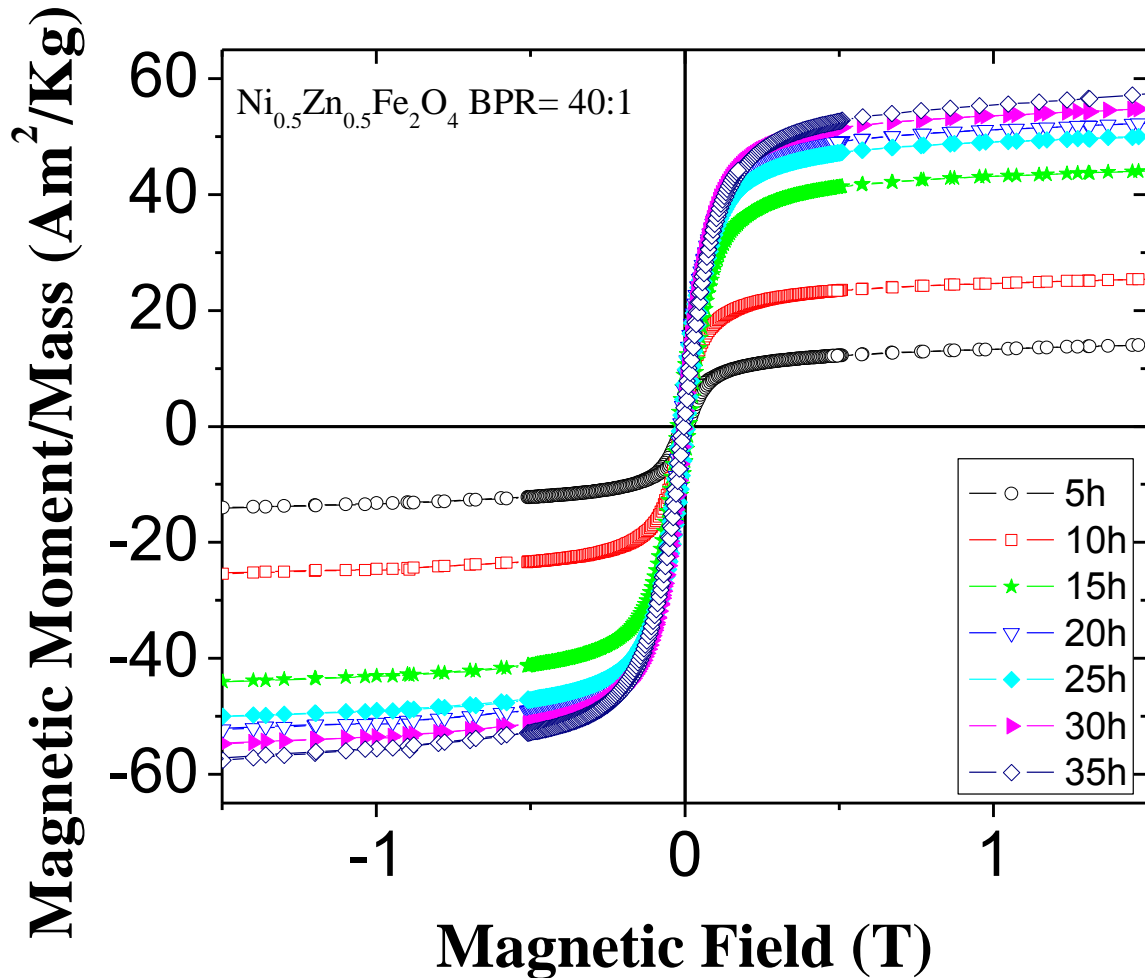


Figure 9.1.3. Vibrating sample magnetometer (VSM) corresponding to the different ball milled of $\text{Ni}_{0.5}\text{Zn}_{0.5}\text{Fe}_2\text{O}_4$ for BPR 40:1 as a function of time.

The graph 9.1.3, shows the magnetic moment per unit mass (specific magnetization) versus applied magnetic field for different milling times. We observed a gradual increase of magnetization as the milling time is increasing from 5 hours to 35 hours grinding. Overall, these

the milled materials are substantially consistent with the XRD measurements analysis displayed in figure 9.1.1, in which change in particle size and average strain associated with the materials are observed. As with the particle size, the specific magnetization of each sample, depending on the particle size, which in turn is related to the increase in the milling time. This increased specific magnetization with decreasing particle size can be attributed to a variation in the distribution site in nanoparticles. However, it is unclear observe this behavior in the graph of M_s vs. H , therefore, it was necessary to make a specified plot of magnetization and coercivity versus time of milling.

Milling Time (h)	Saturation specific Magnetization- M_s (Am^2/Kg)	Coercivity- H_{ci} (mT)
5	1.43	6.88
10	38.58	2.88
15	46.36	3.75
20	30.40	4.77
25	15.80	4.00
30	13.15	4.14
35	16.34	5.59

Table 9.1.2. Saturation specific magnetization and coercivity of $\text{Ni}_{0.5}\text{Zn}_{0.5}\text{Fe}_2\text{O}_4$ in different milling time.

In the figure 9.1.4, we observe that there is a progressive increase of the magnetization specified as milling time increases as expected from the graph of M_s vs. H , contrary to the coercivity that shows a significant increase of 19.5 mT at 15 hours of milling and then goes decreasing smoothly to a value of 11.5 mT at 35 hours of milling. This sudden change in coercivity is related to the change in grain size values that change just the same grinding time (15 h). The behavior of the coercivity in the range of 5 to 15 hours of milling is consistent with the results

found in XRD measurements and average particle size, which shows the existence of the $\text{Ni}_{0.5}\text{Zn}_{0.5}\text{Fe}_2\text{O}_4$ to the 5 hours of milling. In the second interval of 15 to 30 hours of milling, there is a progressive decrease reaching a minimum of 5.59 mT. This behavior appears to be a cyclic, which is due to the formation of crystalline and amorphous phases of the sample of Ni-Zn, when there is an increase in the milling time, as has been reported [23, 27, 53]. These amorphous phases are justified by the broadening of the XRD peaks, which again is connected with the reduction of average grain size, has been reported where the dependence of the saturation magnetization is sensitive to specify the structure [27]. The behavior of the specified saturation magnetization as milling time increases is very similar to the behavior of the saturation magnetization when NiFe_2O_4 ferrite is doped with different concentrations of Zn from 0 to 100% or when formulated ferrites MFe_2O_4 are doped different transition metals ($\text{M} = \text{Mn, Fe, Co, Ni, Cu, Zn}$) [4, 14]. For this case we can explain magnetism from the viewpoint of the distribution of cations among crystallographic interstitial octahedral sites 64 and 32 tetrahedral that exist in unit cell [13]. This means that the octahedral sites are dominant in the surface layers. In the crystal structure of ferrite Ni-Zn, the Zn^{2+} ions occupy tetrahedral sites preferably, the Fe^{3+} ions occupy both tetrahedral and octahedral sites, meanwhile, ions Ni^{2+} occupy octahedral sites most preferably ions Fe^{3+} [15, 28]. As the ball mill causes disorder in the crystallinity of the lattice, we expect that the behaviors of magnetization change in the course of ball milling, also the fresh surfaces generated by the ball mill contact several sometimes causing effects on the surface to be larger Ni ions. Therefore, the contribution of Ni ions to the total magnetic moment is greater due to the milling process.

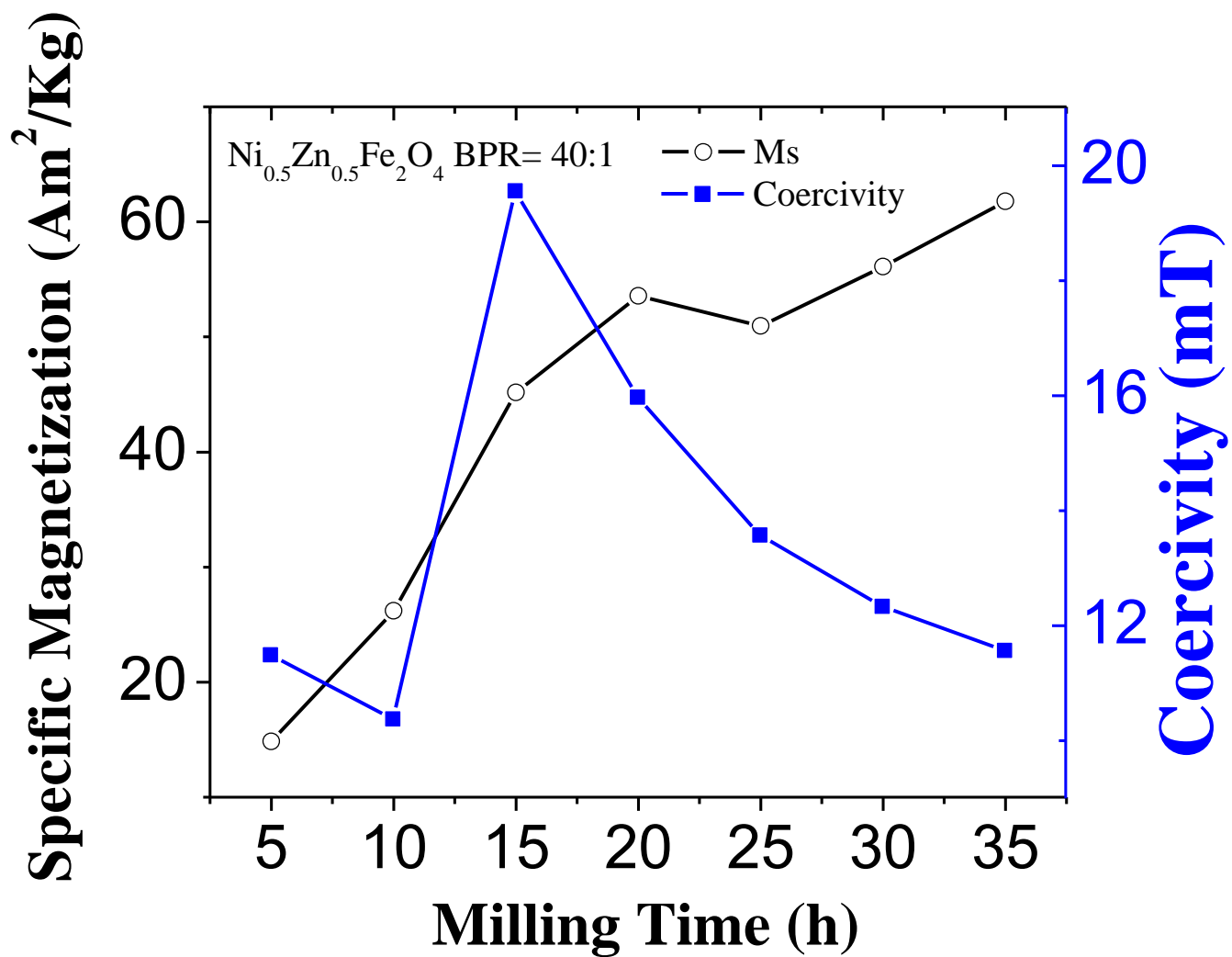
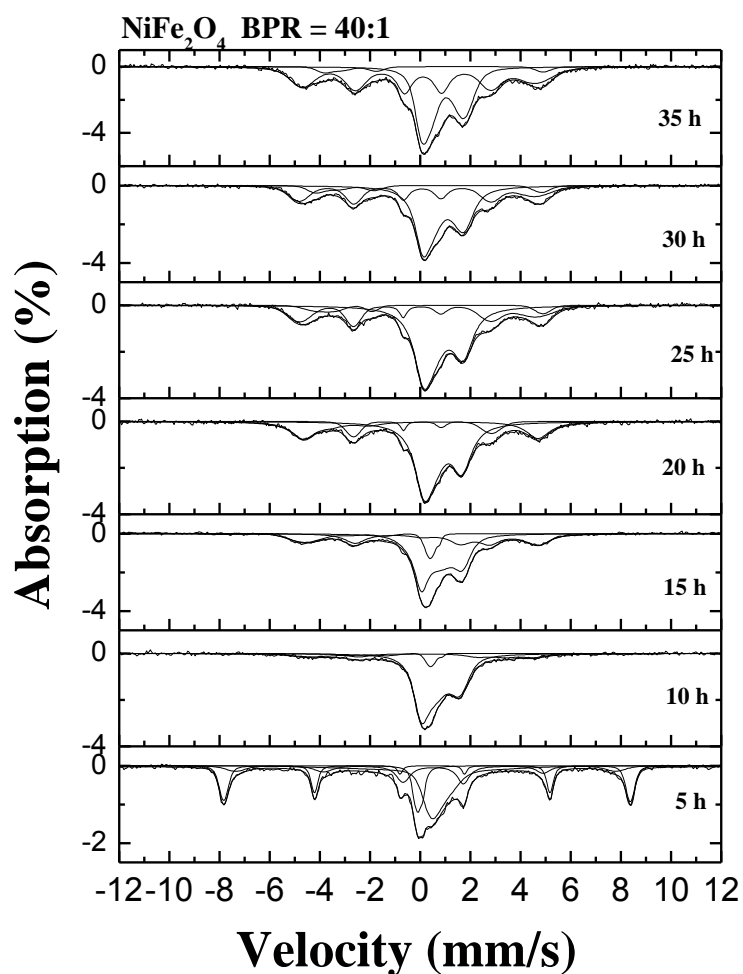


Figure 9.1 4. Evolution of coercivity and saturation magnetization as a function of ball milling of $\text{Ni}_{0.5}\text{Zn}_{0.5}\text{Fe}_2\text{O}_4$ for BPR 40:1

9.3 Measurements of Mössbauer for BPR 40:1

In order to study the possibility of structural changes and chemical of Fe ions in the nanocrystalline Ni-Zn particles, room temperature ^{57}Fe Mossbauer spectra for the samples are shown in Figure 9.1.5. For the first 5 hours of milling, it is interesting that the acceptable fit of the spectra was obtained only when the data were fitted with three sextets. In the first 5 hours of milling there is a significant reduction sextet intensity characteristic, which means that the sample reaches a state where the process of mechanochemical synthesis was achieved faster compared to the previous synthesis (10:1 and 20:1), by the progressive consumption of the precursor materials, achieving superparamagnetic phase at 10 hours of milling that is consistent with X-ray measurements, VMS and particle size reduction. With these observations, one authoritarian state that the mechanochemical synthesis process was achieved via the consumption of the precursor materials as evidenced by the reduction in intensity of the sextet peaks and the simultaneous evolution of the central non magnetic peaks. The component of the spectrum for the 10 hours milled state which account for after 5.6 % of the material was fitted with an internal magnetic field of 487.01 kOe. If showed be noted here, that the isomer shift corresponding to this site was 6.35×10^{-4} mm/s while the quadrupole splitting of -0.37 mm/s and line broadening based an peaks full with at high maximum (FWHM) was 0.24 mm/s indicated that structural formation or transition occurred at this stage. The totality of this observation points to progressive evolution of the materials with ball milling, while the superparamagnetic site which accounted for 44.34 % in the 10 hours milled state. It could be suggested that the milled materials reached a stage where further milling could display the mechanochemical synthesis



Figures 9.1 5. Mössbauer spectra of $\text{Ni}_{0.5}\text{Zn}_{0.5}\text{Fe}_2\text{O}_4$ for BPR = 40:1

Authors	Synthesis Method	Particle size	Superparamagnetic Phase
Bulat R. Churagulov [48]	Hydrothermal	12-16 nm	OK
D.G. Chen [49]	Co-precipitation	20.8 -53.3 nm	OK
Woo Hyun Kwon [51]	Sol-gel	15 nm	OK
Qiaoling Li [52]	Coprecipitation	40 nm	OK

Table 9.1.3. Comparison of particles sizes obtained for $\text{Ni}_{0.5}\text{Zn}_{0.5}\text{Fe}_2\text{O}_4$ for different synthesis methods.

10. Conclusions

- The $\text{Ni}_{0.5}\text{Zn}_{0.5}\text{Fe}_2\text{O}_4$ phase formation is related to the decrease in particle size as a function of milling time.
- $\text{Ni}_{0.5}\text{Zn}_{0.5}\text{Fe}_2\text{O}_4$ phase with BPR 20:1 and 40:1, was achieved for milling times of 15 and 5 hours, respectively. For the sample with BPR of 10:1, was not reached the stage of $\text{Ni}_{0.5}\text{Zn}_{0.5}\text{Fe}_2\text{O}_4$.
- $\text{Ni}_{0.5}\text{Zn}_{0.5}\text{Fe}_2\text{O}_4$ solid solution with BPR 40:1 has the highest specific magnetization, compared to solid solutions with different BPR, with a value of $60 \text{ Am}^2/\text{Kg}$.
- The solid solutions of $\text{Ni}_{0.5}\text{Zn}_{0.5}\text{Fe}_2\text{O}_4$ with BPR 40:1 and 20:1, show superparamagnetic phase for a milling time of 10 and 25 hours respectively, as shown by the results of spectroscopy Mössbauer.

REFERENCE

- [1] A. C. F. M. Costa, E. Tortella, M. R. Morelli, and R. H. G. A. Kiminami, "Synthesis , microstructure and magnetic properties of Ni – Zn ferrites," *Magnetis and Magnetic Materials*, vol. 256, pp. 174–182, 2003.
- [2] Y. Guo, S. Feng, N. Wang, B. Wang, and M. Gu, "Bi₄Ti₃O₁₂–(Ni_{0.5}Zn_{0.5})Fe₂O₄ dielectric–ferromagnetic ceramic composites synthesized with nanopowders," *Materials Chemistry and Physics*, vol. 124, no. 1, pp. 184–187, Nov. 2010.
- [3] T. Verdier, V. Nachbaur, and M. Jean, "Mechanosynthesis of zinc ferrite in hardened steel vials: Influence of ZnO on the appearance of Fe(II)," *Journal of Solid State Chemistry*, vol. 178, no. 11, pp. 3243–3250, Nov. 2005.
- [4] E. Manova, D. Paneva, B. Kunev, E. Rivière, C. Estournès, and I. Mitov, "Characterization of nanodimensional Ni-Zn ferrite prepared by mechanochemical and thermal methods," *Journal of Physics: Conference Series*, vol. 217, p. 012102, Mar. 2010.
- [5] P. C. Fannin, S. W. Charles, and J. L. Dormann, "Field dependence of the dynamic properties of colloidal suspensions of Mn_{0.6}Zn_{0.34}Fe₂O₄ and Ni_{0.5}Zn_{0.5} Fe₂O₄ particles," *Journal of Magnetism and Magnetic Materials*, vol. 201, pp. 99–102, 1999.
- [6] C. Upadhyay, D. Mishra, H. C. Verma, S. Anand, and R. P. Das, "Effect of preparation conditions on formation of nanophase Ni–Zn ferrites through hydrothermal technique," *Journal of Magnetism and Magnetic Materials*, vol. 260, no. 1–2, pp. 188–194, Mar. 2003.
- [7] H.-T. Jiang, X.-F. Wang, C.-L. Yu, and L. Wang, "Molten Salt Synthesis of Ni 0.5 Zn 0.5 Fe 2 O 4 Powders," *Materials and Manufacturing Processes*, vol. 25, no. 12, pp. 1489–1493, Dec. 2010.
- [8] H. E. Zhang, B. F. Zhang, G. F. Wang, X. H. Dong, and Y. Gao, "The structure and magnetic properties of Zn_{1–x}Ni_xFe₂O₄ ferrite nanoparticles prepared by sol–gel auto-combustion," *Journal of Magnetism and Magnetic Materials*, vol. 312, no. 1, pp. 126–130, May 2007.
- [9] M. Jean and V. Nachbaur, "Determination of milling parameters to obtain mechanothesized ZnFe₂O₄," *Journal of Alloys and Compounds*, vol. 454, no. 1–2, pp. 432–436, Apr. 2008.
- [10] I. Ismail, M. Hashim, K. Amin Matori, R. Alias, and J. Hassan, "Milling time and BPR dependence on permeability and losses of Ni_{0.5}Zn_{0.5}Fe₂O₄ synthesized via mechanical alloying process," *Journal of Magnetism and Magnetic Materials*, vol. 323, no. 11, pp. 1470–1476, Jun. 2011.

- [11] O. Uwakweh, "Mössbauer spectroscopy study of the high energy ball milling (HEBM) synthesis & kinetics of CoFe_2O_4 from $\text{Co}(\text{OH})_2$ and," *Journal of Physics: Conference*, vol. 217, no. 012086, pp. 11–15, 2010.
- [12] S. Verma, P. a. Joy, and S. Kurian, "Structural, magnetic and Mössbauer spectral studies of nanocrystalline $\text{Ni}_{0.5}\text{Zn}_{0.5}\text{Fe}_2\text{O}_4$ ferrite powders," *Journal of Alloys and Compounds*, vol. 509, no. 37, pp. 8999–9004, Sep. 2011.
- [13] Q. Li, C. Chang, H. Jing, and Y. Wang, "Synthesis and characterization of shape-controlled $\text{Ni}_{0.5}\text{Zn}_{0.5}\text{Fe}_2\text{O}_4$ via the coprecipitation method," *Journal of Alloys and Compounds*, vol. 495, no. 1, pp. 63–66, Apr. 2010.
- [14] F. . Li, L. Wang, J. . Wang, Q. . Zhou, X. . Zhou, H. . Kunkel, and G. Williams, "Site preference of Fe in nanoparticles of ZnFe_2O_4 ," *Journal of Magnetism and Magnetic Materials*, vol. 268, no. 3, pp. 332–339, Jan. 2004.
- [15] D. C. Kulkarni, U. B. Lonkar, and V. Puri, "High-frequency permeability and permittivity of $\text{Ni}_x\text{Zn}_{(1-x)}\text{Fe}_2\text{O}_4$ thick film," *Journal of Magnetism and Magnetic Materials*, vol. 320, no. 12, pp. 1844–1848, Jun. 2008.
- [16] P. G. McCormick, "Application of Mechanical Alloying to Chemical Refining (overview)." pp. 161–169, 1995.
- [17] D. C. Kulkarni, S. P. Patil, and V. Puri, "Properties of $\text{Ni}_x\text{Zn}_{(1-x)}\text{Fe}_2\text{O}_4$ thick films at microwave frequencies," *Microelectronics Journal*, vol. 39, no. 2, pp. 248–252, Feb. 2008.
- [18] B. . Zhang, L. Lu, and M. . Lai, "Evolution of vacancy densities in powder particles during mechanical milling," *Physica B: Condensed Matter*, vol. 325, pp. 120–129, Jan. 2003.
- [19] N. D. Chaudhari, R. C. Kambale, D. N. Bhosale, S. S. Suryavanshi, and S. R. Sawant, "Thermal hysteresis and domain states in Ni–Zn ferrites synthesized by oxalate precursor method," *Journal of Magnetism and Magnetic Materials*, vol. 322, no. 14, pp. 1999–2005, Jul. 2010.
- [20] Goya, G F, "Ionic disorder and Neel Temperature in ZnFe_2O_4 nanoparticles," vol. 197, pp. 191–192, 1999.
- [21] D. G. Chen, X. G. Tang, J. B. Wu, W. Zhang, Q. X. Liu, and Y. P. Jiang, "Effect of grain size on the magnetic properties of superparamagnetic $\text{Ni}_{0.5}\text{Zn}_{0.5}\text{Fe}_2\text{O}_4$ nanoparticles by co-precipitation process," *Journal of Magnetism and Magnetic Materials*, vol. 323, no. 12, pp. 1717–1721, Jun. 2011.
- [22] N. Randrianantoandro, A. M. Mercier, M. Hervieu, and J. M. Greneche, "Direct phase transformation from hematite to maghemite during high energy ball milling," *Materials Letters*, vol. 47, no. January, pp. 150–158, 2001.
- [23] J. Chappert and R. B. Frankel, "Moossbauer study of Ferrimagnetic ordering in nickel ferrite and chromiun-substituted nickel ferrite," *Physical review letters*, vol. 19, no. 10, pp. 19–21, 1967.

- [24] H. Mio, J. Kano, and F. Saito, "Scale-up method of planetary ball mill," *Chemical Engineering Science*, vol. 59, no. 24, pp. 5909–5916, Dec. 2004.
- [25] S. Ghatak, "Electrical Conductivity, Magnetoconductivity and Dielectric Behaviour of (Mg,Ni)-Ferrite below Room Temperature," *Materials Sciences and Applications*, vol. 01, no. 04, pp. 177–186, 2010.
- [26] C. Suryanarayana, "Mechanical alloying and milling," *Progress in Materials Science*, vol. 46, pp. 1–184, 2001.
- [27] B. P. Rao, O. Caltun, I. Dumitru, and L. Spinu, "Ferromagnetic resonance parameters of ball-milled Ni–Zn ferrite nanoparticles," *Journal of Magnetism and Magnetic Materials*, vol. 304, no. 2, pp. e752–e754, Sep. 2006.
- [28] C. N. Chinnasamy, A. Narayanasamy, N. Ponpandian, and K. Chattopadhyay, "The influence of Fe³⁺ ions at tetrahedral sites on the magnetic properties of nanocrystalline ZnFe₂O₄," *Materials Science and Engineering A*, vol. 306, pp. 983–987, 2001.
- [29] a. E. Virden and K. O'Grady, "Structure and magnetic properties of NiZn ferrite nanoparticles," *Journal of Magnetism and Magnetic Materials*, vol. 290–291, pp. 868–870, Apr. 2005.
- [30] S. J. Stewart, S. J. a. Figueroa, M. B. Sturla, R. B. Scorzelli, F. García, and F. G. Requejo, "Magnetic ZnFe₂O₄ nanoferrites studied by X-ray magnetic circular dichroism and Mössbauer spectroscopy," *Physica B: Condensed Matter*, vol. 389, no. 1, pp. 155–158, Feb. 2007.
- [31] a. K. M. A. Hossain, S. T. Mahmud, M. Seki, T. Kawai, and H. Tabata, "Structural, electrical transport, and magnetic properties of Ni_{1-x}Zn_xFe₂O₄," *Journal of Magnetism and Magnetic Materials*, vol. 312, no. 1, pp. 210–219, May 2007.
- [32] S. Vladimir, D.- Hannover, A. Feldhoff, P. Heitjans, F. Krumeich, C.- Zurich, D. Menzel, F. J. Litterst, D.- Braunschweig, I. Bergmann, and K. D. Becker, "Nonequilibrium Cation Distribution , Canted Spin Arrangement , and Enhanced Magnetization in Nanosized MgFe₂O₄ Prepared by a One-Step Mechanochemical Route," *Chem. Mater.*, vol. 3, no. 1, pp. 3057–3067, 2006.
- [33] W. H. Kwon, J. Y. Kang, J. Lee, S. W. Lee, and K. P. Chae, "Synthesis and Magnetic Properties of Zn, Co and Ni Substituted Manganese Ferrite Powders by Sol-gel Method," *Journal of Magnetism*, vol. 15, no. 4, pp. 159–164, Dec. 2010.
- [34] S. K. Date, P. a. Joy, P. S. A. Kumar, B. Sahoo, and W. Keune, "Structural, magnetic and Mössbauer studies on nickel-zinc ferrites synthesized via a precipitation route," *Physica Status Solidi (C)*, vol. 1, no. 12, pp. 3495–3498, Dec. 2004.
- [35] F. Li, H. Wang, L. Wang, and J. Wang, "Magnetic properties of ZnFe₂O₄ nanoparticles produced by a low-temperature solid-state reaction method," *Journal of Magnetism and Magnetic Materials*, vol. 309, no. 2, pp. 295–299, Feb. 2007.
- [36] G. Srinivasan, V. M. Laletsin, R. Hayes, N. Puddubnaya, E. T. Rasmussen, and D. J. Fekel, "Giant magnetoelectric effects in layered composites of nickel zinc ferrite and lead zirconate titanate," *Solid State Communications*, vol. 124, no. 10–11, pp. 373–378, Dec. 2002.

- [37] G. F. Goya and H. R. Rechenberg, "Magnetic properties of ZnFe₂O₄ synthesized by ball milling," vol. 203, pp. 141–142, 1999.
- [38] T. S. Ward, W. Chen, M. Schoenitz, R. N. Dave, and E. L. Dreizin, "A study of mechanical alloying processes using reactive milling and discrete element modeling," *Acta Materialia*, vol. 53, no. 10, pp. 2909–2918, Jun. 2005.
- [39] G. Pozo López, a. M. Condó, S. E. Urreta, S. P. Silvetti, and M. D. C. Aguirre, "Ni_{0.5}Zn_{0.5}Fe₂O₄ nanoparticles dispersed in a SiO₂ matrix synthesized by sol–gel processing," *Materials Characterization*, vol. 74, pp. 17–27, Dec. 2012.
- [40] S. Bid and S. . Pradhan, "Characterization of crystalline structure of ball-milled nano-Ni–Zn-ferrite by Rietveld method," *Materials Chemistry and Physics*, vol. 84, no. 2–3, pp. 291–301, Apr. 2004.
- [41] R. K. Singh, C. Upadhyay, S. Layek, and A. Yadav, "Cation distribution of Ni_{0.5}Zn_{0.5}Fe₂O₄ nanoparticles," *International Journal of Engineering, Science and Technology*, vol. 2, no. 8, pp. 104–109, 2010.
- [42] S. a. Saafan, T. M. Meaz, E. H. El-Ghazzawy, M. K. El Nimr, M. M. Ayad, and M. Bakr, "A.C. and D.C. conductivity of NiZn ferrite nanoparticles in wet and dry conditions," *Journal of Magnetism and Magnetic Materials*, vol. 322, no. 16, pp. 2369–2374, Aug. 2010.
- [43] G. Pozo López, S. P. Silvetti, S. E. Urreta, and a. C. Carreras, "Structure and magnetic properties of NiZn ferrite/SiO₂ nanocomposites synthesized by ball milling," *Journal of Alloys and Compounds*, vol. 505, no. 2, pp. 808–813, Sep. 2010.
- [44] U. Ghazanfar, "Preparation and Characterization of Ferrite Materials for Practical Applications." 2005.
- [45] T. Iwasaki, T. Yabuuchi, H. Nakagawa, and S. Watano, "Scale-up methodology for tumbling ball mill based on impact energy of grinding balls using discrete element analysis," *Advanced Powder Technology*, vol. 21, no. 6, pp. 623–629, Nov. 2010.
- [46] L. K. Leung, B. J. Evans, and A. H. Morrish, "Low-Temperature Mossbauer Study of a Nickel-Zinc Ferrite: Zn_xNi_[1-x]Fe₂O₄," *Physical review B*, vol. 8, 1973.
- [47] B. P. Rao and O. F. Caltun, "Microstructure and magnetic behaviour of Ni-Zn-Co ferrites," *Optoelectronics and Advantage Materials*, vol. 8, no. 3, pp. 995–997, 2006.
- [48] O. N. C. Uwakweh, R. P. Moyet, R. Mas, C. Morales, P. Vargas, J. Silva, Á. Rossa, and N. López, "Mössbauer spectroscopy study of the synthesis of SnFe₂O₄ by high energy ball milling (HEBM) of SnO and α-Fe₂O₃," *IOPscience*, vol. 217, no. 012087, pp. 4–8, 2010.
- [49] S. . B. and N. Zeman, "Mossbauer study Ni_{0.25}Zn_{0.75}Fe₂O₄." 1980.
- [50] A. Sato, J. Kano, and F. Saito, "Analysis of abrasion mechanism of grinding media in a planetary mill with DEM simulation," *Advanced Powder Technology*, vol. 21, no. 2, pp. 212–216, Mar. 2010.

- [51] I. Ismail and M. Hashim, "Synthesized via Mechanical Alloying," *Aust. J. Basic & Appl. Sci.*, vol. 5, no. 11, pp. 1865–1877, 2011.
- [52] I. H. Gul, W. Ahmed, and a. Maqsood, "Electrical and magnetic characterization of nanocrystalline Ni–Zn ferrite synthesis by co-precipitation route," *Journal of Magnetism and Magnetic Materials*, vol. 320, no. 3–4, pp. 270–275, Feb. 2008.
- [53] N. Sivakumar, a Narayanasamy, N. Ponpandian, J.-M. Greneche, K. Shinoda, B. Jeyadevan, and K. Tohji, "Effect of mechanical milling on the electrical and magnetic properties of nanostructured Ni_{0.5} Zn_{0.5} Fe₂ O₄," *Journal of Physics D: Applied Physics*, vol. 39, no. 21, pp. 4688–4694, Nov. 2006.
- [54] H. Ehrhardt, S. J. Campbell, and M. Hofmann, "Structural evolution of ball-milled ZnFe₂O₄," vol. 339, pp. 255–260, 2002.